Increase of Spin Polarization for Energy Calibration at LEP

von

Florian Sonnemann

Diplomarbeit in Physik

vorgelegt der

Mathematisch-Naturwissenschaftlichen Fakultät der
Rheinisch-Westfälischen Technischen Hochschule Aachen

im

Juni 1998

angefertigt im

III. Physikalischen Institut A

bei

Priv. Dozent Dr. M. Tonutti

Abstract

Die präziseste Strahlenergiebestimmung bei LEP basiert auf einer $g - 2$ Messung der Elektronen mittels resonanter Depolarisation des Strahls. Bei Strahlenergien höher als 45 GeV ist diese Methode durch depolarisierende Effekte limitiert. Die Kompensation von depolarisierenden Resonanzen wurde verbessert durch Verringerung der störenden Strahlablenkung in den optischen Elementen des Speicherringes. Dazu wurde die Fehlausrichtung der Strahlpositionsmonitore mittels einer Strahlmessung bestimmt und die mechanische Fehlaufstellung der Quadrupolmagnete analysiert. Außerdem wurden die Maschineinstellungen verbessert, um die Anregung depolarisierender Effekte zu verkleinern. Während des LEP Jahres 1997 konnte erstmalig eine Strahlenergiekalibration bei 55,3 GeV mittels resonanter Depolarisation durchgeführt werden. Des weiteren wurde Strahlpolarisation bei 60,6 GeV gemessen.

The most accurate beam energy determination at LEP is based on a $g - 2$ measurement of electrons via resonant depolarization of the beam. At beam energies beyond 45 GeV this method is limited due to depolarizing effects. The compensation of depolarizing resonances was improved by reducing the beam deflection in the optical elements of the storage ring. Therefore the misalignment of the beam position monitors was detected with a dynamic beam based measurement and the mechanical misplacement of the quadrupole magnets was analysed. In addition, the machine parameters were optimised in order to minimise the excitation of depolarizing effects. During the 1997 LEP run it was possible for the first time to calibrate the beam energy at 55.3 GeV with resonant depolarization and to observe polarization at 60.6 GeV.

Contents

Chapter 1

Introduction

Large accelerators have been built for high energy physics in order to investigate the properties of particles and their interactions. Various types of linear and circular accelerators were constructed to reach higher energies. The highest centre of mass energy E_{cm} is achieved in accelerators in which two beams of particles are accelerated to the same energy and collided head-on.

In storage rings two beams (protons, anti-protons, electrons and positrons) are brought into collision for many hours inside large detectors. Positron-electron (e^+e^-) collisions are very valuable as these are point-like particles. LEP, the *L*arge *E*lectron *P*ositron collider was build at CERN (Conseil Européen pour la Recherche Nucléaire) near Geneva, Switzerland, to study in detail the bosons of the electro-weak interactions, the Z and the W. The Z was discovered in 1983 at CERN

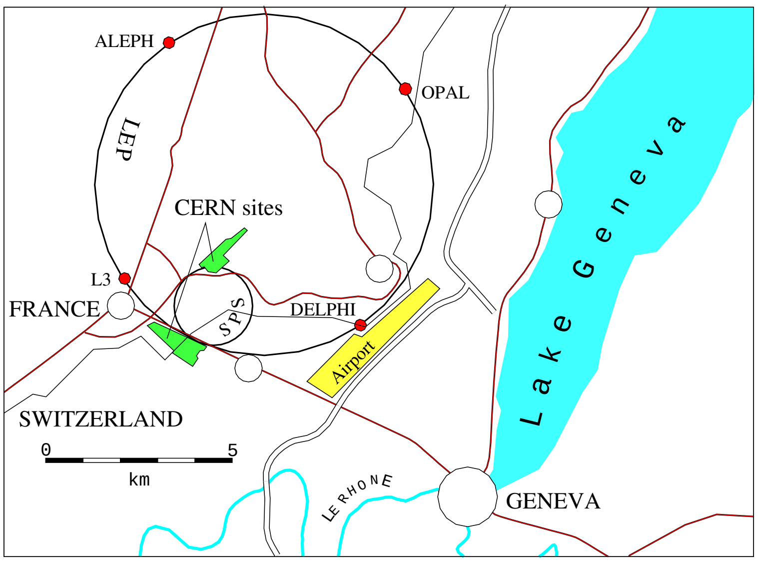

Figure 1.1: LEP ring, taken from the 'LEP Design Report'

in the SPS (a proton accelerator). The storage ring with its circumference of 26.7 km is shown in Fig. 1.1. It is the largest electron positron collider in the world and is described comprehensively in the 'LEP Design Report' [1]. Four experiments are installed around the ring to record the events from the e^+e^- collisions.

Between 1989 and 1995 LEP was used to investigate the properties of the Z boson in the beam energy range of 40–48 GeV (LEP I). The hadronic cross-section increases significantly at a centre of mass energy corresponding to the mass of the Z. This phenomenon is known as the Z resonance (see Fig. 1.2). The dominating reaction is

$$e^+ \, e^- \to Z^0 \to f \, \overline{f}$$

where $f\overline{f}$ indicates a fermion anti-fermion pair.

In general, a resonance is characterised by its peak value and its width. The location of the peak value gives the mass whereas the width corresponds to the lifetime. The error of the statistical determination of the cross-section together with the beam energy uncertainty leads to the total error of the Z resonance parameters. The beam energy was calibrated using the transverse spin polarization in e^+e^- storage rings. The measurement is based on resonant depolarization. The precise determination of the number of spin oscillations per particle revolution reduced the beam energy error to $\Delta E_{beam} = \pm 1.5$ MeV. Due to the hadronic cross-section at the Z energy (see Fig. 1.2) the data acquisition during the LEP running period of one year was enough to reduce the statistical error of the Z mass and width to a value comparable to the beam energy uncertainty. The Z mass could be determined to $m_Z = 91186.3 \pm 1.9$ MeV whereas the width was given by $\Gamma_Z = 2494.7 \pm 2.6$ MeV. The given errors include the contribution of both systematic and statistical errors.

Further results of this LEP period are the exclusion of a fourth neutrino with a mass below 45 GeV and a prediction of the mass of the top quark (see ‘Physics at LEP I’ [2]).

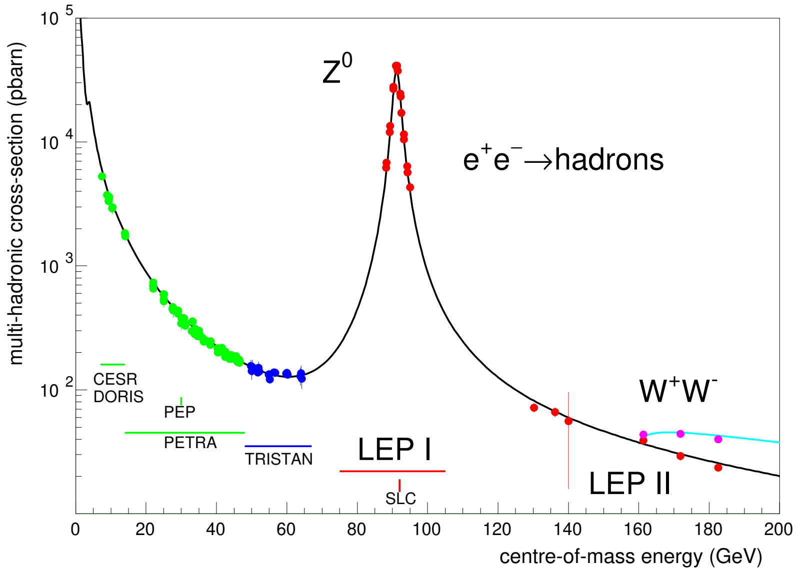

Figure 1.2: Total hadronic cross-section without initial state radiation for different lepton colliders as a function of the centre of mass energy.

The W bosons, the partner of the Z, have been studied since 1996 (LEP II). As the W bosons are charged particles, only W^+W^- pairs can be produced and require a minimum centre of mass energy of $2m_W c^2 = 160.6$ GeV. The energy loss per revolution due to synchrotron radiation in e^+e^- storage rings which scales with energy ($\propto E^4/\rho$, ρ being the average radius) and limits the achievable beam energy. In order to compensate the energy losses and to reach the beam energy which is required for W pair production, super-conducting RF (radio-frequency) cavities have been developed and installed in the ring to supply a higher accelerating voltage. Since 1995 new super-conducting cavities have been installed every year. In 1997 the maximum beam energy was 94 GeV, but stable operation could only be made at 91.5 GeV. The ultimate goal of LEP is to approach a beam energy of 100 GeV in the year 1999 or 2000. The stepwise increase of the centre of mass energy allows testing of the standard model up to 200 GeV, to look for the Higgs Boson H and to search for super-symmetric particles.

In contrast with the Z resonance energy, the hadronic cross-section is much lower at higher energies (see Fig. 1.2). The largest contribution that is given by

$$e^+ \, e^- \to \gamma \to f \, \overline{f}$$

decreases proportionally to the energy squared. Just above the threshold energy of the W pair production the cross-section σ_{tot} is slightly increased due to the reaction

$$e^+ \, e^- \to W^+ \, W^- \to f \, \overline{f} \, f'\overline{f'}$$

and is used to determine the W mass. Beyond $E_{cm} = 160$–165 GeV the W mass is reconstructed from the invariant mass of decay products. The Higgs boson can be produced according to the reaction

$$e^+ \, e^- \to Z^* \to Z^0 \, H \to f \, \overline{f} \, f'\overline{f'}.$$

From the measurements taken up to the end of 1997, a Higgs boson mass below 90 GeV has been excluded. To reduce the statistical uncertainty of the W mass to 30 MeV, about 8000 W^+W^- events are required per experiment. The target for energy calibration is to reduce the uncertainty on the beam energy below 15 MeV.

The transverse spin polarization essentially disappears at beam energies beyond 60 GeV so that only magnetic devices can be used to determine the beam energy. The magnetic instruments are calibrated at lower energies with resonant depolarization. The beam energy is given by the extrapolation of the calibration points to the operating energy. Its uncertainty depends on the linearity of the extrapolation and on the highest energy which is calibrated with resonant depolarization.

This Diploma Thesis describes the improvements which were made to increase the transverse polarization to calibrate the beam energy beyond 50 GeV. After a short general introduction of some accelerator physics concepts, the theory of transverse spin polarization in storage rings is summarised. The LEP accelerator is presented and the energy calibration method is explained. Methods to increase the polarization level are shown and their impacts are simulated. The measurements made in order to improve the compensation of depolarizing effects are analysed. The results of polarization measurements are presented and compared with the simulation results. The improvement for the LEP energy calibration is described.

Chapter 2

Fundamental Concepts

Electro-magnetic fields are used to guide particles in accelerators. A more detailed description can be found for example in [3, 4, 5]. The Lorentz force $\vec{F_l}$ which acts on a particle with momentum $\vec{p}$ and charge e is given by

$$\vec{F_l} = \frac{d\vec{p}}{dt} = \frac{dm\gamma\vec{v}}{dt} = \dot{\vec{p}} = e\vec{v} \times \vec{B} + e\vec{E} \tag{2.1}$$

where $\vec{B}$ is the magnetic field and $\vec{v}$ is the velocity of the particle. In the relativistic case the momentum is given by $\vec{p} = m\gamma\vec{v}$, m being the rest mass and $\gamma = E/E_0$ being the ratio of the energy and rest energy of the particle.

The particle motion in a circular accelerator is described in a coordinate system which moves along the design trajectory of the ring instead of Cartesian coordinates. The longitudinal motion is characterised by the longitudinal coordinate s (see Fig. 2.1). Deviations in the transverse planes are expressed with x, y, respectively.

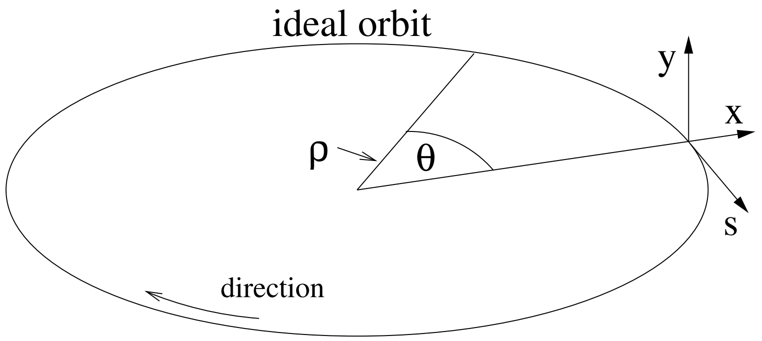

Figure 2.1: Coordinate system in circular accelerators which follows a perfect particle's trajectory in the horizontal plane.

The revolution frequency is given by

$$f_{rev} = \frac{\mid \vec{v} \mid}{C} \tag{2.2}$$

where C is the circumference of the accelerator and $\vec{v}$ the velocity of the particle. For ultra-relativistic particles $f_{rev} = c/C$ where c is the velocity of light (at LEP $f_{rev} = 11246\,\mathrm{Hz}$).

The particles are accelerated with the help of electric fields inside radio-frequency cavities. At LEP most of the cavities are super-conducting.

Dipole magnets are used to bend the particles. The bending radius ρ for a particle with momentum p and charge e travelling in the horizontal plane in the presence of a constant vertical dipole field B_y follows from the equality of the centrifugal F_c and Lorentz F_l force

$$\rho = \frac{p}{eB_y}. \tag{2.3}$$

The product $B_y\rho = p/e$ is called the magnetic rigidity. The bending angle of a single dipole magnet with length l is $\theta_i = (B_y l)/(B_y\rho) = (eB_y l)/p$.

A large number of particles form the beam which is accelerated. When the particles are injected into the accelerator each particle has its own position and angle. Without any focusing force they would continue to separate more and more until they are lost. In accelerators like LEP the beam is focused with the help of quadrupole magnets separated from the dipole magnets (see Fig. 2.2). The magnetic field of a quadrupole is given by

$$B_x = \frac{\partial B_x}{\partial y} y_Q \qquad\qquad B_y = \frac{\partial B_y}{\partial x} x_Q \tag{2.4}$$

where x_Q and y_Q are the offsets of the particle position with respect to the centre of the quadrupole. As the deflection of a particle by a quadrupole depends linearly on the distance to the centre,

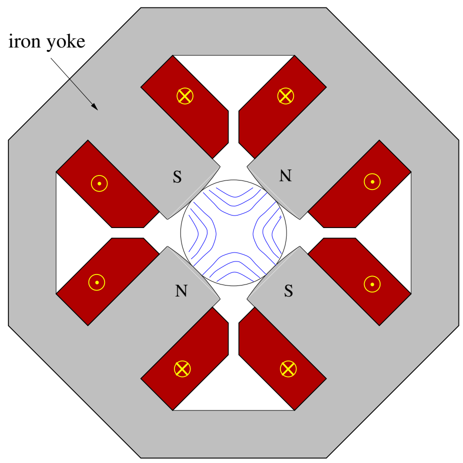

Figure 2.2: Quadrupole with magnetic field lines.

quadrupoles can be used to focus the beams. From Maxwells' laws it follows that $\partial B_x/\partial y = \partial B_y/\partial x$ and, consequently, quadrupoles focus in one plane and defocus in the other plane. To obtain a magnet lattice that is focusing in both planes, quadrupoles with gradients of opposite sign are combined in a so-called *FODO* lattice (see Fig. 2.3). It consists of a horizontally *F*ocusing quadrupole, a drift space (or a dipole) *O*, a horizontally *D*efocusing quadrupole and another drift space (or dipole) *O*. In other words, quadrupoles are used to correct the dipoles which alone are insufficient to keep the particles in the accelerator. The *ideal* or design orbit is formed by the trajectory passing through the centre of the perfectly aligned quadrupole magnets.

Electric fields $\vec{E}$ are often not sufficient to guide the particles since the force of a $1T$ magnetic field corresponds to a force of an $3 \cdot 10^8 \frac{V}{m}$ electric field.

2.1 Linear Beam Dynamics

If quadrupole magnets are used to focus the beam, the two transverse motions x, y can be treated independent of one another. The restoring focusing force is linear and can be expressed as $F_x = k \cdot x$, $F_y = -k \cdot y$, where k is the quadrupole field strength. The differential equations for the transverse motions become [3]

$$\frac{d^2x(s)}{ds^2} + \left(\frac{1}{\rho^2(s)} - k(s)\right) x(s) = \frac{1}{\rho(s)}\frac{\Delta p}{p} \tag{2.5}$$

$$\frac{d^2y(s)}{ds^2} + k(s)y(s) = 0. \tag{2.6}$$

In Eq. 2.5 an additional focusing term coming from the bending magnets ($\propto 1/\rho(s)^2$) appears. It has just a small effect in large accelerators like LEP compared to the strong focusing of the quadrupoles. The horizontal motion also depends on the relative momentum spread $\Delta p/p$ of the particles. Such a term only appears for the vertical plane when magnets are misaligned or when the accelerator is not in a plane.

For on-momentum particles ($\Delta p = 0$), both equations are of the form

$$\frac{d^2x(s)}{ds^2} + k(s)x(s) = 0. \tag{2.7}$$

It is similar to the equation of motion of a harmonic oscillator, differing only by the fact that the restoring force depends on the longitudinal position. This type of differential equation is called Hill's equation. The solution can either be stable or unstable. The beam is focused or defocused at a position s according to the sign of $k(s)$

$$k(s) = \begin{cases} \text{defocusing} & \text{if } k(s) < 0 \\ \text{focusing} & \text{if } k(s) > 0 \end{cases} \tag{2.8}$$

k is a period function which means $k(s) = k(s + C)$, where C is the circumference. The stable solution of Hill's equation has a closed form

$$x(s) = A\sqrt{\beta(s)}cos[\Psi(s) + \phi]. \tag{2.9}$$

The motion $x(s)$ depends on the phase advance $\Psi(s)$, the beta function $\beta(s)$ and the initial conditions which determine the amplitude A and the phase ϕ. $\beta(s)$ and $\Psi(s)$ are related

$$\frac{d\Psi(s)}{ds} = \frac{1}{\beta(s)}. \tag{2.10}$$

The phase advance from position s_0 to $s_0 + \Delta s$ is given by

$$\Psi(s_0 \to s_0 + \Delta s) \equiv \Delta\Psi_{\Delta s} = \int_{s_0}^{s_0+\Delta s} \frac{ds}{\beta(s)}. \tag{2.11}$$

The solution of Eq. 2.9 is an oscillation whose amplitude depends on the local value of the beta function. The number of these betatron oscillations per revolution are called the betatron tunes

$$Q_{x,y} = \frac{1}{2\pi}\oint \frac{ds}{\beta(s)} = \frac{1}{2\pi}\left[\Psi_{x,y}(s + C) - \Psi_{x,y}(s)\right]. \tag{2.12}$$

The initial conditions, the beam position x_0 and its angle x'_0 define the phase space volume occupied by a particle. For a particle with constant energy this volume is conserved. The emittance or Courant-Snyder invariant $\epsilon = \sqrt{A}$ expresses this volume

$$\frac{\epsilon}{\pi} = \gamma(s)x^2(s) + 2\alpha(s)x(s)x'(s) + \beta(s)x'^2(s) \tag{2.13}$$

where the Twiss parameters α and γ are derived from the beta function

$$\alpha(s) \equiv -\frac{1}{2}\frac{d\beta(s)}{ds} \tag{2.14}$$

$$\gamma(s) \equiv \frac{1+\alpha^2(s)}{\beta(s)}. \tag{2.15}$$

For a beam with a Gaussian distribution of particles without a momentum spread, the conserved beam emittance ϵ defines the beam sizes at any point by

$$\sigma(s) = \sqrt{\epsilon\beta(s)}. \tag{2.16}$$

From the knowledge of the beam position and angle $x(s_1), x(s_1)'$ at any position s_1 in the ring, it is possible to construct the coordinates at a position s_2 using a matrix formalism.

For example, the changes after one revolution in the ring, $x(s+C), x'(s+C)$ are given by multiplying the initial conditions $x(s_1), x'(s_1)$ with the transport matrix $M_{s_1 \to s_1+C}$, which contains the Twiss functions 2.14

$$\begin{pmatrix} x \\ x' \end{pmatrix}_{s_1+C} = \begin{pmatrix} \cos(\Delta\Psi_C) + \alpha\sin(\Delta\Psi_C) & \beta\sin(\Delta\Psi_C) \\ -\gamma\sin(\Delta\Psi_C) & \cos(\Delta\Psi_C) - \alpha\sin(\Delta\Psi_C) \end{pmatrix} \begin{pmatrix} x \\ x' \end{pmatrix}_{s_1}. \tag{2.17}$$

Another way to compute the beam position is possible by solving Eq. 2.7 for each accelerator element individually and integrating numerically or, if possible , analytically. A single quadrupole with strength k and length l can be represented by a thin lens with focal length f which becomes

$$\frac{1}{f} = kl = \frac{1}{B\rho}\frac{dB_y}{dx} = \frac{e}{p}\frac{dB_y}{dx}. \tag{2.18}$$

The trajectory of an individual particle with nominal momentum is expressed by

$$x(s) = x_{co}(s) + x_\beta(s) \tag{2.19}$$

where x_{co} is the closed orbit and x_β is a betatron oscillation described by Eq. 2.9. The closed orbit x_{co} is a particular solution which is periodic $[x_{co}(s) = x_{co}(s+C)]$ and closed after one turn. The individual trajectories are *not* closed. An example is given in Fig. 2.3a for a perfectly aligned accelerator where $x_{co} = 0$. This situation corresponds to the ideal case ($x_{co}^{ideal} = 0$). In the case where the quadrupoles are misaligned (see Fig. 2.3b), the closed orbit is no longer identical with the ideal closed orbit and can go off-centred through the quadrupoles. Orbit correction dipoles are usually installed in the accelerator cells to restore the beam. In order to calculate the corrector strengths the beam position has to be known. Beam position monitors (BPMs) are installed all around the accelerator (LEP contains 500 BPMs). A BPM works like a capacitor. It consists of two metal plates. The passing beam generates charges in both plates. The ratio of the generated charges determines the beam position in the plane of the plates. The averaged signal (at LEP over about 200 revolutions) corresponds to the closed orbit beam position. The strengths of the correctors can be calculated by dedicated algorithms from the measurement of the closed orbit.

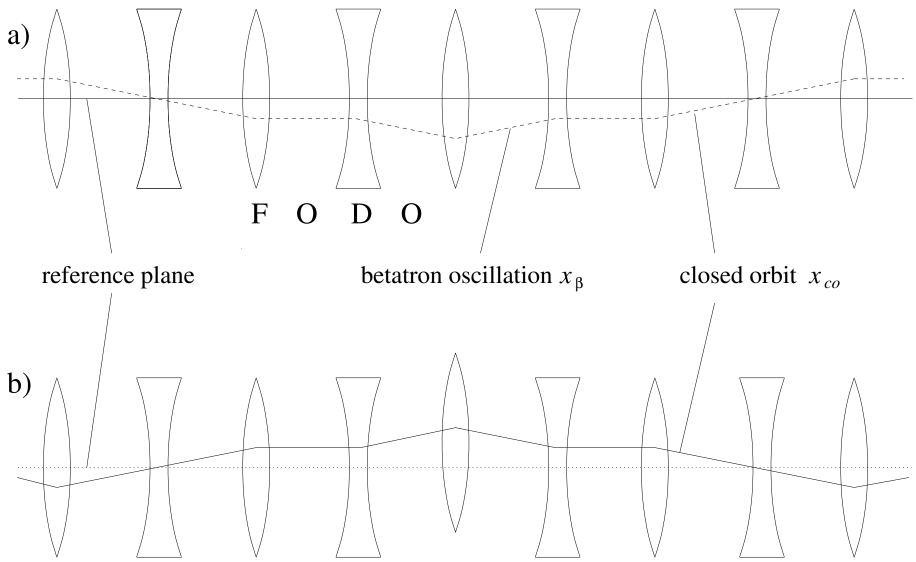

Figure 2.3: Focusing principle: a) perfect ring b) effect of misaligned quadrupoles.

In an accelerator the beam always has a certain momentum spread. A charged particle which is accelerated (curved trajectory) emits photons. This photon emission is known as synchrotron radiation in accelerators. For e^+/e^- storage rings, the equilibrium momentum spread Δp is given by the quantum excitation due to the emission of photons. The emitted power P for a particle with momentum p following a trajectory with an average bending radius $< \rho >$ can be taken from [6]

$$P = \frac{e^2 c}{6\pi\epsilon_0} \frac{\gamma^4}{< \rho^2 >} \tag{2.20}$$

where c is the speed of light in vacuum. The energy loss per turn is given by

$$\Delta E_T = \int_T P dt. \tag{2.21}$$

T is the revolution time which for ultra relativistic particles becomes $T = 2\pi\rho/c$. The integration over one revolution yields

$$\Delta E_T = \frac{e^2}{3\epsilon_0 (m_0 c^2)^4} E^4 \left\langle \frac{1}{\rho} \right\rangle = C_\gamma E^4 \left\langle \frac{1}{\rho} \right\rangle \tag{2.22}$$

where the constant $C_\gamma = 8.85 \cdot 10^{-5}\,\mathrm{m\,GeV}^{-3}$ for electrons. Because of the factor $m_0 c^2$ the synchrotron radiation of electrons is $1.13 \cdot 10^{13}$ times stronger than the synchrotron radiation of protons for the same beam parameters. The opening angle of the photons with respect to the longitudinal direction of the particle is approximately equal to $2\gamma^{-1}$. The recoil momentum of the emitted photon can be composed of a longitudinal component and of a transverse component. The longitudinal component is proportional to the energy loss whereas the transverse component excites the transverse motion of the beam. The energy loss due to the longitudinal component of the recoil momentum of the synchrotron radiation must be replaced every turn by accelerating cavities.

A particle whose momentum differs from the nominal momentum by Δp has a different solution of the Hill's equation. It causes the particle to travel on a different orbit

$$x(s) = x_{co}(s) + x_\beta(s) + D(s) \frac{\Delta p}{p} \tag{2.23}$$

where $D(s)$ is the dispersion function. It is periodic and satisfies the horizontal equation of motion (see Eq. 2.5) for $\Delta p/p = 1$

$$\frac{d^2D(s)}{ds^2}\left(\frac{1}{\rho^2(s)} - k_x(s)\right)D(s) = \frac{1}{\rho(s)}. \tag{2.24}$$

The horizontal dispersion D_x differs greatly from zero only in the horizontal plane because the bending radius in a dipole magnet depends on the particle's momentum and the trajectories vary for particles with different momenta. This produces dipole kicks which generate the dispersion. At LEP the average D_x is in the order of 1 m. Dispersion in both planes is created by the focusing deflection in the quadrupoles which depends on the momentum. It is significantly smaller than the dispersion due to the dipole magnets. Thus, the vertical dispersion D_y of LEP is about 2 cm.

The change in the path length of an off-momentum particle around the accelerator is described by the momentum-compaction-factor α

$$\frac{\Delta L}{L} = -\alpha \cdot \frac{\Delta p}{p} \simeq -\alpha \cdot \frac{\Delta E}{E} \tag{2.25}$$

where α is obtained from the closed integral over the dispersion function

$$\alpha = \frac{1}{C}\oint \frac{D(s)}{\rho(s)}ds. \tag{2.26}$$

At LEP α is about $4 \cdot 10^{-4}$ at 45 GeV.

Off-momentum particles also perform energy (momentum) oscillations in the presence of the RF cavities which are called synchrotron oscillations. The number of these oscillations per turn is expressed in the synchrotron tune Q_s.

$$Q_s \propto \sqrt{U_0\left(\alpha - \frac{1}{\gamma^2}\right)} \tag{2.27}$$

where U_0 is the total accelerating voltage of the RF cavities, α given by Eq. 2.26 and $\gamma = E/E_0$. Whereas the betatron tunes $Q_{x,y}$ are much larger than unity, the synchrotron tune Q_s is mostly in the order of 0.1. The value of Q_s can affect the beam lifetime. The possibility of losing particles in the longitudinal motion is expressed by the quantum lifetime τ_Q which depends on Q_s. In case of a very small τ_Q the particle loss due to a Q_s value that is too small becomes dominant and limits the beam lifetime. Therefore Q_s is chosen to ensure a minimum quantum lifetime of about 100 hours.

Furthermore, particles with a different momentum receive a different focusing strength since $k \propto p^{-1}$ (see Eq. 2.18). This changes the number of betatron oscillations and leads to a tune shift. The dependence of the tune on the momentum deviation Δp can be understood as a focusing error which means the imperfection of a quadrupole. It is called chromaticity ξ and is defined by

$$\Delta Q = \xi(p)\frac{\Delta p}{p}. \tag{2.28}$$

In large accelerators like LEP the chromaticity due to the quadrupoles is in the range of $\xi \propto -150$. The associated tune shifts can lead to an unfavourable combination of tunes. For this reason the chromaticity is adjusted to values $\xi \propto 0$ to $+10$ with the help of sextupole magnets. Sextupole magnets focus the beam like quadrupoles but their field depends quadratically on the transverse beam positions. The sextupole magnets are installed at places where the dispersion function is maximal. Particles are focused depending on the value of their momentum offset (see Eq. 2.23).

The transverse magnetic field can be expanded in a series which becomes for the vertical magnetic field B_y

$$\frac{e}{p}B_y(x) = \frac{e}{p}B_{y0} + \frac{e}{p}\frac{dB_y}{dx}x + \frac{1}{2!}\frac{e}{p}\frac{d^2B_y}{dx^2}x^2 + \frac{1}{3!}\frac{e}{p}\frac{d^3B_y}{dx^3}x^3 + ... \tag{2.29}$$

Eq. 2.29 changes for the horizontal magnetic field B_x to

$$\frac{e}{p}B_x(y) = \frac{e}{p}B_{x0} + \frac{e}{p}\frac{dB_x}{dy}y + \frac{1}{2!}\frac{e}{p}\frac{d^2B_x}{dy^2}y^2 + \frac{1}{3!}\frac{e}{p}\frac{d^3B_x}{dy^3}y^3 + ... \tag{2.30}$$

Magnets are usually designed to produce a field corresponding ideally to a single component of series 2.29, 2.30. The Table 2.1 summarises the definitions and impacts of the introduced magnet types. The first terms correspond to dipole magnets. In the horizontal plane they are used to bend

Magnet multipole	Definition		Impact
	horizontal	vertical	
Dipole	$\frac{1}{\rho} = \frac{e}{p}B_{y0}$	$\frac{e}{p}B_{x0}$	bending
Quadrupole	$k_x = \frac{e}{p}\frac{dB_y}{dx}$	$k_y = \frac{e}{p}\frac{dB_x}{dy}$	focusing
Sextupole	$m_x = \frac{e}{p}\frac{d^2B_y}{dx^2}$	$m_y = \frac{e}{p}\frac{d^2B_x}{dy^2}$	chromaticity compensation

Table 2.1: Definition of different magnet types.

the particles on the desired trajectory. Dipoles are also important in order to correct quadrupole misalignment in both planes. The second terms describe the field of quadrupole magnets which focus the beam. The energy dependence of the quadrupole focusing, the chromaticity, is compensated by sextupole magnets. Octupole magnets are also installed in LEP. In general, the i^{th} order magnet multipole is used to correct the $(i\text{-}1)^{th}$ order.

Storage rings are designed to produce as many particle collisions as possible in the interaction points where the beams are colliding. The performance of a storage ring with colliding beams is given by the luminosity $\mathcal{L}$. The event rate dN/dt is proportional to the cross-section which characterises a given process and to the luminosity

$$\frac{dN}{dt} = \sigma\mathcal{L}. \tag{2.31}$$

The luminosity $\mathcal{L}$ is a function that solely depends on storage ring parameters and can be expressed as

$$\mathcal{L} = \frac{1}{4\pi}\frac{kf_{rev}N^2}{\sigma_x\sigma_y} \tag{2.32}$$

where N is the number of particles per particle ensemble, called bunch, and k is the number of bunches per beam. σ_x and σ_y express the horizontal and vertical beam size at the interaction points. Eq. 2.32 assumes that the intensity is equal for every bunch and that both beams have the same number of bunches. During the 1997 LEP run the positron and the electron beam contained 4 bunches with an intensity of 10^{11} to 10^{12} particles per bunch. $\mathcal{L}$ is optimised by careful tune settings, chromaticity adjustments, orbit corrections, etc. This leads to a luminosity in the order of 10^{31} to $10^{32}\text{cm}^{-2}\text{s}^{-1}$.

2.2 Transverse Spin Polarization in Storage Rings

The spin of fermions is an internal degree of freedom. It is a quantum phenomenon which is described by the spin operator S. The spin eigenstates are the solutions of the Dirac equation. The most precise calculation also takes effects like field quantisation and vacuum polarization into account. These corrections explain the gyro-magnetic anomaly g compared to a Dirac particle.

The Correspondence Principle of quantum mechanics establishes that the expectation value of quantum operators follows equivalent rules to a classical variable. Therefore the spin can be treated as a classical vector $\vec{S}$. A fermion with the rest mass m_0, charge e and spin $\vec{S}$ carries a magnetic momentum μ

$$\vec{\mu} = \frac{ge}{2m_0}\vec{S}. \tag{2.33}$$

The interaction of external electro-magnetic fields with the spin induced magnetic momentum has to be considered. In an accelerator it is useful to group the external fields in 3 main classes where the index refers the field direction with respect to the particle's momentum:

- Transverse magnetic fields $\vec{B}_\perp$. In storage rings $\vec{B}_\perp$ is dominated by the horizontal bending field B_y.
- Longitudinal magnet fields $\vec{B}_{||}$. The solenoid magnets of the experimental detectors are an example. Due to this field the paths of charged particles which are produced in beam collisions are bent and their momenta can be determined.
- Electric fields $\vec{E}$. Their influence is usually small compared to the strength of magnetic fields.

Thomas derived the equation of spin motion for a relativistic Dirac particle [7] in the presence of external fields. His results were modified by Bargmann, Michel and Telegdi [8] who took higher order corrections like the gyro magnetic anomaly into account. Their solution is known as the Thomas-BMT equation

$$\frac{d\vec{S}}{dt} = \vec{\Omega}_{BMT} \times \vec{S}. \tag{2.34}$$

The time derivative of the spin vector is equal to the vector product of the spin revolution frequency Ω_{BMT} and the spin vector. In the presence of external fields $\vec{B}_\perp$, $\vec{B}_{||}$ and $\vec{E}$, $\vec{\Omega}_{BMT}$ is given by

$$\vec{\Omega}_{BMT} = -\frac{e}{\gamma m}\left[(1+a\gamma)\vec{B}_\perp + (1+a)\vec{B}_{||} - (a\gamma + \frac{\gamma}{1+\gamma})\vec{\beta} \times \frac{\vec{E}}{c}\right] \tag{2.35}$$

where $a = (g-2)/2 = 0.001159652193(10)$. A quantitative analysis of Eq. 2.35 allows the classification of these fields [9]:

- Electric fields $\vec{E}$ are negligible as their effect is small compared to magnetic fields.
- The influence of longitudinal magnetic fields $\vec{B}_{||}$ decreases with energy. Consequently, longitudinal magnetic fields coming from imperfections of the accelerator do not strongly contribute. The spin rotation by the solenoid fields is reduced as the particle's energy is increased.

- The contribution of transverse magnetic fields is energy independent for ultra-relativistic particles.

Eq. 2.34 and 2.35 describe the precession of the spin in external fields. In an *ideal* storage ring where $\vec{B}_{||} = \vec{0}$ and $\vec{E} = \vec{0}$, the spin precesses around the vertical bending field B_y. The number of spin oscillations per revolution is defined as the spin tune ν. Relative to the revolution frequency the spin precession $\vec{\Omega}_a$ is

$$\vec{\Omega}_a = \vec{\Omega}_{BMT} - f_{rev} = a\gamma f_{rev} \tag{2.36}$$

where the spin tune is defined as $\nu = a\gamma$. It is proportional to the beam energy $E_{beam} = \gamma E_0$, where $E_0 = m_0 c^2$. As a consequence a measurement of the spin tune ν can be used to determine the beam energy since

$$\gamma = \frac{\nu}{a}. \tag{2.37}$$

This fact motivates polarization studies since the measurement of ν is only possible for a beam polarization level of a sufficient value [10]. For example, a beam energy of 45.6 GeV corresponds to a spin tune of 103.5 at LEP. The method how to determine the spin tune is explained later.

For an ensemble of N particles the spin polarization $\vec{P}$ can be defined as the normalised vector sum of the single spin vectors $\vec{S}_i$

$$\vec{P} = \frac{1}{N}\sum_{i=1}^{N} \vec{S}_i. \tag{2.38}$$

The polarization level corresponds to the absolute value of $\vec{P}$. The statistical definition of the polarization is based on the difference of the number of spins that are pointing in a certain direction $N_{\uparrow\uparrow}$ and the number of spins pointing in the opposite direction $N_{\uparrow\downarrow}$

$$P = \frac{\mid N_{\uparrow\downarrow} - N_{\uparrow\uparrow} \mid}{N_{\uparrow\downarrow} + N_{\uparrow\uparrow}}. \tag{2.39}$$

2.2.1 Equilibrium Polarization

When an electron emits a photon, there is a certain probability to flip the spin. Sokolov and Ternov calculated the two transition rate probabilities for a spin flip as a function of the initial spin direction parallel or anti-parallel to the bending field (Sokolov-Ternov-Effect [10]) and found an asymmetry. Assuming an accelerator with a bending field B_y, the transition rate R for a spin flip due to photon radiation in a bending field with radius ρ for a particle with rest mass m_0 and charge e is given by

$$R = \frac{5\sqrt{15}}{16}\frac{e^2\gamma^5\hbar}{m_0^2 c^2 \rho 3}\left[1 + \frac{8}{5\sqrt{3}}(\vec{S}e_y)\right] \tag{2.40}$$

where $\hbar$ is the Heisenberg constant. $\vec{S}$ denotes the spin direction before emitting a photon. On average at LEP, a particle emits 10^{11} photons before a spin flip occurs. R changes the sign depending on the initial spin direction. The polarization is given by the normalised difference of the rates having the final spin direction parallel $R_{\uparrow\uparrow}$ or anti-parallel $R_{\uparrow\downarrow}$ to the vertical bending field

$$P_{ST} = \frac{R_{\uparrow\uparrow} - R_{\uparrow\downarrow}}{R_{\uparrow\uparrow} + R_{\uparrow\downarrow}} = \frac{8}{5\sqrt{3}}\frac{\oint \rho(s)^{-3} ds}{\oint \mid \rho(s)^{-3} \mid ds} = 92.4\%. \tag{2.41}$$

Because $R_{\uparrow\uparrow}$ is larger than $R_{\uparrow\downarrow}$ a particle with charge e tends to align its magnetic moment parallel to the vertical bending field. This leads to the build up of polarization in e^+/e^- storage rings. According to Eq. 2.41 the maximally achievable polarization is 92.4% since $R_{\uparrow\downarrow}$ is not zero. The polarization level P for initially unpolarized beams increases with time exponentially

$$P(t) = P_{ST}\left(1 - \exp(\frac{t}{\tau_p})\right) \tag{2.42}$$

where τ_p is the polarization build up time

$$\tau_p = \left(\frac{8m_e}{5\sqrt{3}r_e\hbar}\right)\cdot\left(\frac{\mid\rho^3\mid}{\gamma^5}\right). \tag{2.43}$$

At LEP τ_p is 351 min for $E_{beam} = 44.7$ GeV.

Imperfections which create non-vertical magnetic fields disturb the spin motion and result in a depolarizing effect (see Section 2.3). It induces a depolarizing rate which can be expressed by a depolarization time τ_d. The relevant time constant is now the effective polarization build up time τ_{eff} which is given by

$$\frac{1}{\tau_{eff}} = \frac{1}{\tau_p} + \frac{1}{\tau_d}. \tag{2.44}$$

The time dependence of the polarization (see Eq. 2.42) becomes

$$P(t) = P_{ST}\frac{\tau_{eff}}{\tau_p}(1 - \exp(\frac{t}{\tau_{eff}}). \tag{2.45}$$

For a given τ_d associated with the imperfections, the maximum achievable polarization level P_∞ is reduced by the term τ_{eff}/τ_p

$$P_\infty = P_{ST}\frac{\tau_{eff}}{\tau_p} = \frac{P_{ST}}{1+\frac{\tau_p}{\tau_d}}. \tag{2.46}$$

A significant reduction occurs when the depolarizing time τ_d is in the order of the τ_p or shorter.

2.2.2 $\vec{n}$-axis

Derbenev and Kontratenko [11] introduced the concept of the n-axis. It corresponds to the closed orbit of the particle motion. The n-axis is the only solution of the spin motion equation (see Eq. 2.34) with the periodicity

$$\vec{n}(s) = \vec{n}(s + C). \tag{2.47}$$

This means that the n-axis is stable in time. Other solutions $\vec{S}$ of Eq. 2.34 which differ from $\vec{n}$ are rotating around $\vec{n}$. Therefore the projection of the spin vectors of a particle ensemble with respect to the n-axis is time independent and the n-axis expresses the direction of the equilibrium polarization $\vec{P}_\infty$. The n-axis can be used to calculate the spin transport matrix $\mathbf{T}$ which is similar to the beam transport matrix of linear optics. In a perfect storage ring the n-axis points in the bending field direction e_y. Misalignment of quadrupoles and high order magnetic fields can cause a tilt between e_y and $\vec{n}$. In general, $\vec{n}$ becomes a function of all phase space variables of the transverse and longitudinal motion for an ensemble of particles

$$\vec{n} = \vec{n}(x, x', y, y', s, \frac{\sigma_E}{E}) \tag{2.48}$$

where (σ_E/E) is the relative energy spread.

2.2.3 Spin Diffusion

In 1966 Baier and Orlov predicted depolarizing effects of synchrotron radiation (spin diffusion) [12]. To demonstrate the increasing importance of depolarizing effects in high energy storage rings, a single electron on the closed orbit is considered. Assuming that the n-axis is identical to the spin vector $\vec{S}$, Fig. 2.4 illustrates the influence of synchrotron radiation on the spin precession at a constant s position of the storage ring.

- First the electron follows the initial orbit and the spin vector is parallel to the $\vec{n}_0 = \vec{n}$-axis. At this longitudinal position the spin vector always has the same direction (Fig. 2.4a).
- After emitting a photon (at $t = t_0$), the electron has a different energy and its motion is disturbed. The electron immediately starts to damp towards the dispersion orbit (see Section 2.1). The periodic solution of the dispersion orbit is different to the initial orbit and can cause another direction of the $\vec{n}$-axis. It has now an angle θ to $\vec{n}_0$. The spin vector starts oscillating with the spin precession frequency $\vec{\Omega}_a$ and an angle ψ to the $\vec{n}$-axis. Immediately after the photon emission, both angles are the same $\psi = \theta$ (Fig. 2.4b).
- The synchrotron radiation damps the oscillation and brings the electron back to the initial orbit. After the oscillation is damped ($t = t_0 + \delta t$) the $\vec{n}$-axis returns to the $\vec{n}_0$ axis, but the precession angle between the $\vec{S}$ and $\vec{n}$ remains constant (Fig. 2.4c and d).

For an ensemble of N particles the projection of $\vec{S}_i$ on $\vec{n}$ is the residual polarization $\vec{P} = \sum \vec{S}_i/N$. The n-axis recovers the initial n_0 direction with time but the spins of the ensemble change their phase relation due to energy differences ΔE of the particles after photon emission. The process of spin kick, damping and phase relation change of the spin vectors is called spin diffusion. It causes a polarization reduction ΔP which is given by the polarization vector before the photon emission $\vec{P}_1$ and after the spin diffusion $\vec{P}_2$

$$\Delta P = \mid \vec{P}_2 - \vec{P}_1 \mid = \mid \vec{P}_1 \mid - \mid \vec{P}_1 \mid \cdot \cos(\psi). \tag{2.49}$$

With $\mid \vec{P}_1 \mid \equiv P$ Eq. 2.49 becomes

$$\Delta P = P[1 - \cos(\psi)]. \tag{2.50}$$

For small perturbations the approximation

$$\cos(\psi) \approx 1 - \frac{1}{2}\psi^2 \tag{2.51}$$

is applicable. Assuming that the relative energy difference $\Delta E/E$ and the amplitudes of the orbit oscillations due to the photon emission are proportional, ΔP can be expressed as

$$\frac{\Delta P}{P} \approx \frac{1}{2}\psi^2 \approx= \frac{1}{2}\left(\vec{d} \cdot \frac{\Delta E}{E}\right)^2. \tag{2.52}$$

One can deduce the coupling of the spin motion with respect to the orbit motion which is defined as $\vec{d}(s)$. Immediately after the photon emission ($t_0 + \epsilon$) the n-axis changes by $\psi = \theta$. The nominal E is reduced by ΔE so that $\vec{d}$ is given by

$$\vec{d}(s) = \psi\frac{E}{\Delta E} = E\frac{\vec{n}(s)_{t_0+\epsilon} - \vec{n}(s)_{t_0}}{\Delta E} = \gamma\frac{\Delta\vec{n}}{\Delta\gamma} \approx \gamma\frac{\partial\vec{n}_0(s)}{\partial\gamma}. \tag{2.53}$$

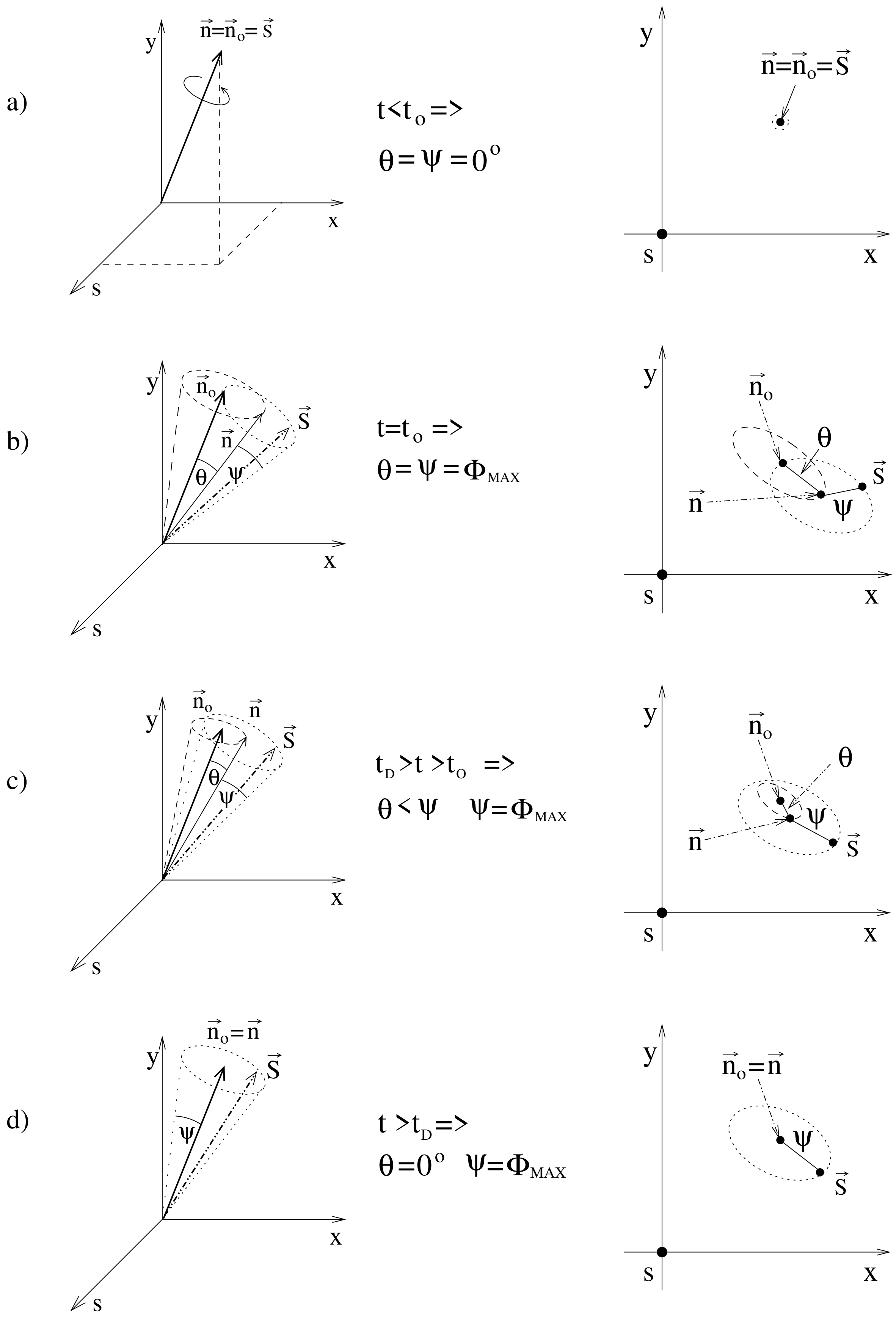

Figure 2.4: Spin vector $\vec{S}$ a) before, and after emitting a photon b), c) and d).

$\vec{d}$ is an important parameter for depolarization. It is orthogonal to $\vec{n}$ and depends on s. It is proportional to the energy derivative of $\vec{n}$ in the linear approximation.

Derbenev and Kontratenko gave the general formalism for the equilibrium degree of polarization P_∞ with respect to the spin-orbit motion coupling [13]

$$P_\infty = \frac{8}{5\sqrt{3}}\frac{\alpha_-}{\alpha_+} \tag{2.54}$$

where $\alpha_-\alpha_+$ are given by

$$\alpha_- = \frac{1}{2\pi R}\left(\oint \frac{ds}{\mid \rho(s) \mid^3} e_y \cdot (\vec{n} - \vec{d})\right) \tag{2.55}$$

$$\alpha_+ = \frac{1}{2\pi R}\left(\oint \frac{ds}{\mid \rho(s) \mid^3}\vec{e}\left(1 - \frac{2}{9}(e_s \cdot \vec{n})^2 + \frac{11}{18} \mid \vec{d} \mid^2\right)\right). \tag{2.56}$$

It can be shown that Eq. 2.46 and 2.54 are equivalent descriptions of the equilibrium polarization.

2.3 Depolarizing Resonances

A beam can be depolarized resonantly by applying a periodic external field which is orthogonal to the leading magnetic field and whose frequency is identical or very close to the spin tune. The resonant depolarization occurs if the spin deflections due to the external field add up coherently over many turns. Therefore the phase relation between the perturbation frequency and the spin precession has to be constant. The condition can be fulfilled if the external field frequency is varied or if the beam energy is shifted without varying the tune settings. If the spin deflections due to the external field do not correlate to the spin tune, the phase difference increases over several turns and the effect disappears in the time average.

Besides the desired resonant depolarization for beam energy calibration, the equilibrium polarization is often limited by spin resonances due to the interaction of the spins with the accelerator lattice. Depolarizing resonances are excited if the spin tune is equal to any combination of the orbit tunes Q_x, Q_y, Q_s (see Section 2.1, Eq. 2.12 and 2.27) and an integer since under such conditions perturbations remain in phase with the spin

$$\nu = k \pm l \cdot Q_s \pm m \cdot Q_x \pm n \cdot Q_y, \qquad k, l, n, m \in \mathbb{N}. \tag{2.57}$$

The reduction of the equilibrium polarization depends on the resonance strength and on its width. An example is given in Fig. 2.5. The different classes of spin resonances contained in Eq. 2.57 are listed below.

Integer Resonances

Integer resonances or imperfection resonances obey the condition

$$\nu = k, \qquad k \in \mathbb{N}. \tag{2.58}$$

In such a case a perturbation of the spin remains in phase from one turn to the next, leading to very strong and fast depolarization. The strengths of the integer resonances are proportional to the angle between $\vec{P}$ and $\vec{n}_0$. The strongest integer resonances corresponds to the LEP super symmetry $S = 4, 8$

$$\nu = \mathrm{INT}(Q_y) + k \cdot S, \qquad k \in \mathbb{N}. \tag{2.59}$$

The betatron oscillations of particles are amplitude modulated with the frequency of the LEP symmetry which leads to an excitation of side frequencies of the betatron frequency [14].

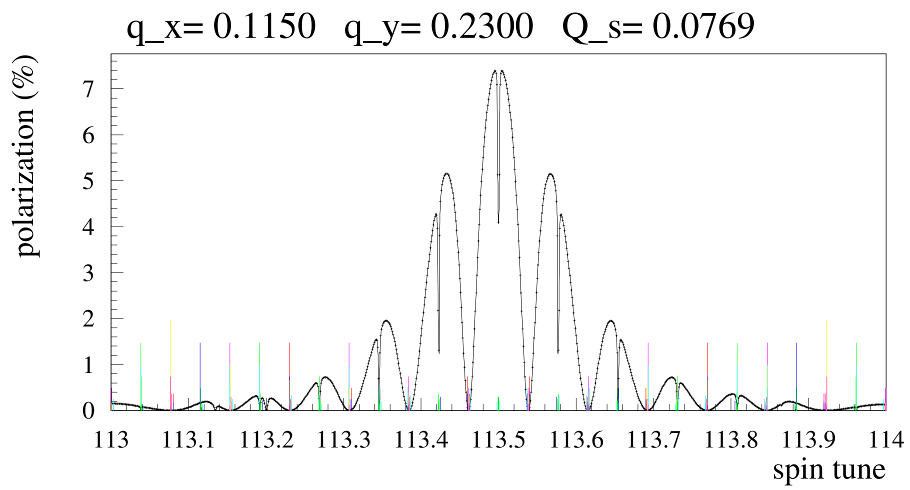

Figure 2.5: Example of the polarization between two integer resonances at 50.0 GeV as a function of the spin tune. The fractional part of the betatron tunes and the synchrotron tune are given. The solid curve corresponds to the polarization depending on different types of resonances which are also shown as lines. The favourable tune settings are discussed in Section 3.3.1.

Linear resonances

Linear or first order resonances (intrinsic resonances) are defined as

$$\nu = k \pm Q_s, \tag{2.60}$$
$$\nu = k \pm Q_x, \tag{2.61}$$
$$\nu = k \pm Q_y, \qquad k \in \mathbb{N}. \tag{2.62}$$

These resonances correspond to the interaction of the spin with the betatron and synchrotron motion of the particles. The linear Q_x, Q_s resonances are mainly excited by the integer resonances next to the spin tune which is derived for an ideal storage ring in the Appendix A (Section A.2). The strength of the Q_s and Q_y resonance is also dependent on the vertical dispersion [9]. At LEP the r.m.s. value of the vertical orbit is minimised for polarization experiments to 250–300μm. This procedure normally reduces the vertical dispersion D_y as well (see Section 3.2).

Non-linear Resonances

Higher order multipole magnets like sextupoles [9] excite non-linear spin resonances which result in the resonance condition

$$\begin{aligned} \nu &= k \pm l \cdot Q_s \pm m \cdot Q_x \pm n \cdot Q_y, \\ l+m+n &\geq 2 \qquad k,l,n,m \in \mathbb{N}. \end{aligned} \tag{2.63}$$

At LEP, the strengths of most non-linear resonances do not limit the maximum polarization degree. However, the higher order synchrotron resonances are very important.

Synchrotron Sidebands

An important subclass of non-linear resonances are the synchrotron sidebands

$$\nu = k \pm n \cdot Q_s, \tag{2.64}$$
$$\nu = k \pm Q_x \pm n \cdot Q_s, \tag{2.65}$$
$$\nu = k \pm Q_y \pm n \cdot Q_s, \qquad k, n \in \mathbb{N}. \tag{2.66}$$

The synchrotron sideband strength is analytically estimated using an algorithm proposed by Buon, Mane, Montague and Yokoya [15, 16, 17]. The synchrotron sidebands of integer and linear betatron resonances are derived using the spin integrals given in Appendix A (Eq. A.9). Their strength is proportional to the *tune modulation index* λ^2

$$\lambda^2 = \left(\frac{a\gamma}{Q_s} \frac{\sigma_E}{E} \right)^2. \tag{2.67}$$

λ^2 is a function of the spin tune $a\gamma$, the synchrotron tune Q_s and the longitudinal emittance expressed by the relative energy spread σ_E/E. It scales with the fourth power of energy. The typical range for λ^2 is between 0.1 and 1 at LEP for energies between 41.2 and 60.6 GeV. In this range σ_E/E increases from $6.2 \cdot 10^{-4}$ to $9.6 \cdot 10^{-4}$. In order to compensate for the energy dependence of σ_E/E, the value of Q_s has to be increased. The equations to calculate the strengths of the m^{th} order synchrotron resonance of an integer or a linear betatron resonance are given in Appendix A (Section A.3). The higher order synchrotron resonances decrease with λ^2. It follows that the complete synchrotron sideband spectrum can be calculated when λ^2 and the strengths of the first order resonances are known. Most polarization algorithms include the influence of the linear synchrotron and betatron resonances between two integer resonances. A two parameter fit derives the resonance strengths and is used to calculate higher order synchrotron sidebands.

Chapter 3

LEP

3.1 LEP Parameters

Storage rings like LEP are usually composed of arcs, where a regular FODO cell structure is repeated many times, and of straight sections (insertions) which provide room for experimental detectors, RF cavities and special magnets like wigglers [1].

LEP is composed of eight arcs (octants) and eight straight sections, four of them housing experiments where the beams are collided. With a circumference of 26658.9 m it is the largest accelerator of the world. LEP is designed to collide two beams with up to four trains, each train consisting of one or two bunches separated by a distance of a few hundred meters. The eight interaction points (IPs) are labelled according to the straight sections. The names and the locations of the four experiments are L3 (IP2), ALEPH (IP4), OPAL (IP6) and DELPHI (IP8) (see Fig. 1.1).

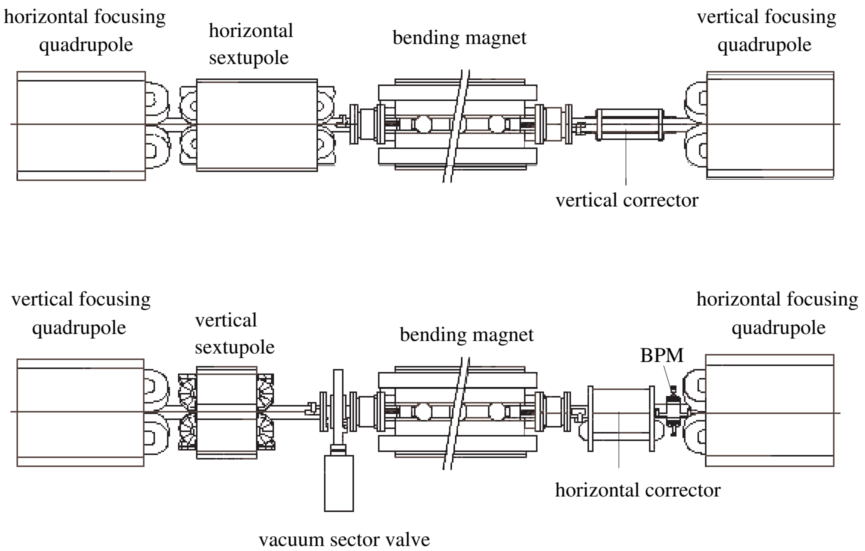

Figure 3.1: Side view of a standard LEP cell divided to a horizontal and a vertical focusing half-cell, taken from the 'LEP-design-report' [1]. The bending magnets are shortened.

In order to avoid collisions at the other IPs, the beams are separated by electro-static fields. RF cavities are installed in the even IPs to accelerate the particles to the energy at which the beams are brought into collision and to compensate for the energy loss due to synchrotron radiation in the arcs.

The LEP standard arc cell is a FODO lattice which is shown in Fig. 3.1 divided into two half cells. The elements and their terms which a LEP cell holds are:

- The horizontally focusing quadrupole magnet QD - the F of the FODO lattice QD.
- A horizontal sextupole magnet $SD.QD$.
- Six bending magnets $B2L/M/R.QD$ (each has a bending angle of 1.87 mrad).
- In two out of every three cells a vertical corrector dipole magnet $CV.QD$.
- The horizontal defocusing quadrupole magnet QF - the *D* of the FODO lattice.
- A vertical sextupole magnet $SF.QF$.
- A vacuum sector valve — every sixth cell is connected with a vacuum pump to obtain the very high vacuum needed not to lose particles due to gas collisions.
- Another six bending magnets $B2L/M/R.QF$.
- In two out of every three cells a horizontal corrector dipole magnet $CH.QD$.
- A beam position monitor for both planes $PU.QD$.

There are 240 such cells. Depending on its cabling (which can vary from cell to cell), a sextupole magnet focuses or defocuses in a given plane. In the injection region, the dipoles are replaced by shorter magnets with higher fields to make room for the fast kicker magnets required to inject the beam.

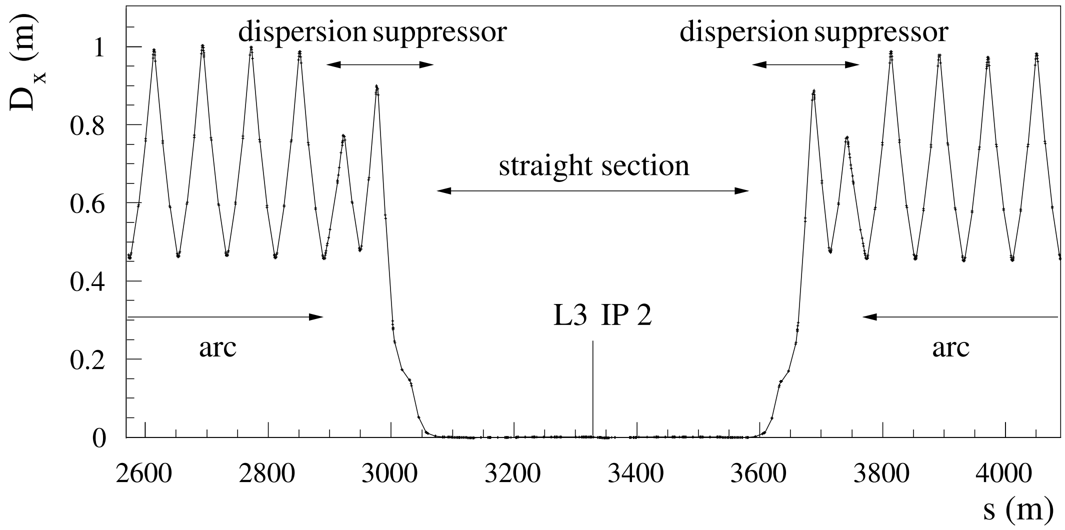

Figure 3.2: Horizontal dispersion D_x as a function of the longitudinal coordinate s at LEP around IP2. It is significantly reduced in the dispersion suppressors.

The areas between the straight sections and arcs are called the dispersion suppressors. They are used to reduce the horizontal dispersion in the straight sections (see Fig. 3.2). Their structure is slightly different to the arcs. The main difference is the variation of the bending angle between two cells of the dispersion suppressor. The quadrupoles in the dispersion suppressors and straight sections are labelled as QL in the odd IPs and QS in the even IPs.

The cells in LEP are labelled by an integer number

$$n_{cell} = \mathrm{IP} \cdot 100 + j$$

where IP is the interaction point number and j is an integer $(0 \leq j \leq 99)$. j is incremented from 0 to 99 starting in the middle of the octant on the left side of the IP and ending in the middle of the octant on the right side of each IP. The IPs correspond to cell numbers

$$n_{cell}^{IP} = \mathrm{IP} \cdot 100 + 50.$$

In 1997 LEP was operated during most of the time with an optics having a horizontal betatron phase advance ϕ_x of $90°$ per cell and a vertical phase advance ϕ_y of $60°$ (90/60 optics). At the end of the 1997 run a 102/90 optics was successfully tested. It minimises the emittance and will be used in 1998 because its luminosity potential might be better than the 90/60. In addition it allows running at a beam energy which is about 0.4 GeV higher than for the 90/60. Table 3.1 summarises some characteristic parameters of LEP.

Description	Symbol	Value
Circumference	C_0	$\simeq$ 26658.9 m
Average radius		$\simeq$ 4242.9 m
Bending radius	ρ	3096.4 m
Maximum beam energy in 1997	E_{beam}	93.5 GeV
Revolution frequency	f_{rev}	11 246 Hz
Number of bunches (in physics)	k_b	2×4 to 2×8
Phase advance for physics optics horizontal/vertical per cell	ϕ_x, ϕ_y	90 / 60 or 102 / 90
Phase advance for polarization optics per cell		60 / 60
Synchrotron radiation energy loss per turn at 92 GeV	E_s	$\approx$ 2 GeV

Table 3.1: Some parameters of LEP, taken from the 'LEP design report' [1, 18].

3.2 Energy Calibration

The beam energy E_{beam} is an important parameter which is required to determine precisely the masses of the W and Z. In a storage ring the beam energy E_{beam} is deduced by the bending field and most exactly determined with the $g-2$ measurement of electrons based on the resonant spin depolarization method. Its accuracy is to the order of a few 10^{-6} [19] and within a magnitude more absolute than any other method. As described in Section 2.2 the spins of the circulating particles align to each other and the beam polarizes with time. The transverse spin polarization level is observed by a Compton laser polarimeter [20, 21]. A circularly polarized laser beam is brought into collision with the electron beam of LEP at IP1. The cross-section depends on the polarization levels of both the particle and the photon beam. The distribution of the backscattered photons is shifted vertically when the direction of the circular polarized light is changed from left to right and when the particle beam is polarized. The vertical shift is proportional to the polarization P and detected with a W-Si strip detector 250 m away from the interaction point. The average statistical error of the polarization level ΔP_{stat} is about

$$\Delta P_{stat} = 0.6 \frac{\%}{\sqrt{min}}. \tag{3.1}$$

In addition, there are uncertainties due to an error of the polarization scale ΔP_{scale} which is proportional to the polarization level $\Delta P_{scale} = 0.048 \cdot P[\%]$. Different sources lead to an error of the polarization measurement (one minute) of

$$\Delta P = 0.8\% + \Delta P_{scale}. \tag{3.2}$$

The scale error dominates only beyond a polarization level of 20%.

The polarization is reduced resonantly by applying an oscillating horizontal magnetic RF field to the beam which is orthogonal to the bending field. The field of the fast kicker magnet which is used at LEP can be modulated at frequencies in the range 0 to $\sim$10 kHz. It interferes with the spin precession and rotates the spin vector by a small amount. If the phase relation between the RF frequency f_{kick} and the spin tune ν is constant, the small spin rotations add up coherently over many particle revolutions and depolarization occurs. This condition requires

$$k \cdot f_{kick} = \nu \cdot f_{rev} \tag{3.3}$$

where $f_{rev} = 11246$ Hz is the revolution frequency of LEP and k is any integer. In that case the polarization vector is rotated by $90°$ around the horizontal axis in about 10^4 turns which corresponds roughly to one second. The frequency of the fast kicker magnet is varied until resonant depolarization is observed. From this measurement only the fractional part q_ν of the spin tune $\nu = k_\nu + q_\nu$ is obtained. The given frequency range of the kicker magnet covers the full range of q_ν. The integer part k_ν is determined from the calibration of the main bending field. An error of one unit on k_ν is excluded because the energy range between two integers of the spin tune corresponds to 440 MeV which is much larger than the accuracy of the magnetic measurement. In ideal conditions the polarization could be flipped from parallel to anti-parallel every few seconds.

There is still an ambiguity since the depolarization can also occur on the mirror frequency $(1 - q_\nu)$ (see Fig. 3.3). This ambiguity is solved with a second depolarization after a known energy

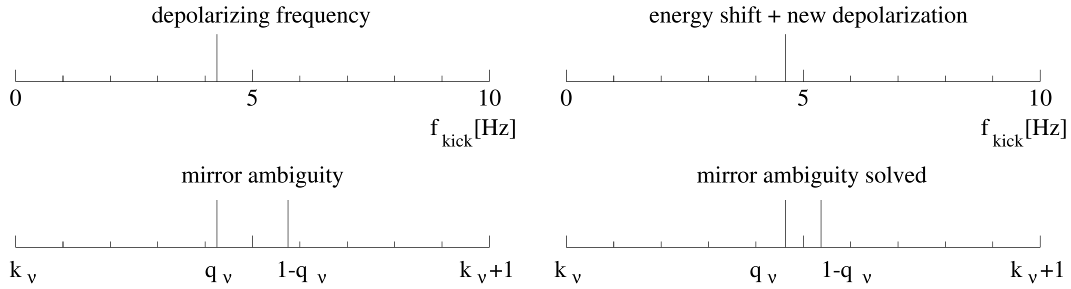

Figure 3.3: The mirror ambiguity. It is solved with a second depolarization after a known energy shift without modifying the tune settings. The figure shows the RF frequency of the kicker magnet f_{kick} (top) and the fractional part of the spin tune q_ν (bottom).

shift via an RF frequency shift. A frequency shift of the RF cavities changes the beam position in the quadrupoles and the integrated magnetic field seen by the beam which changes the beam energy without varying the tune settings. Another uncertainty stems from the fact that depolarizing can also occur on synchrotron sidebands $q_{side} = q_\nu \pm Q_s$. In order to separate a depolarization on a synchrotron sideband of the spin tune, another depolarization is made after a slight change of Q_s which does not change the position of q_ν (see Fig. 3.4).

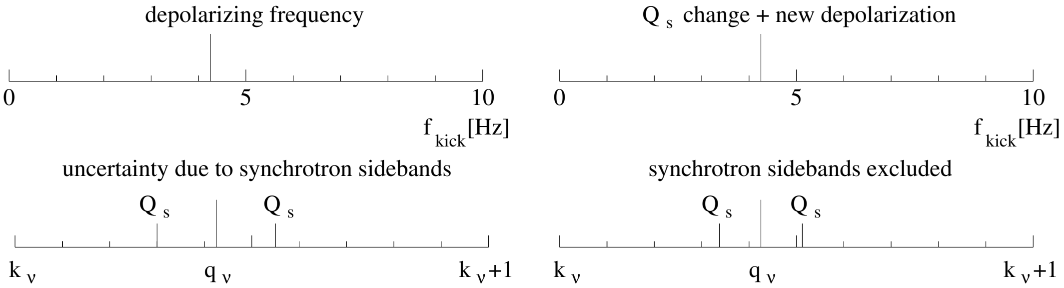

Figure 3.4: The Q_s uncertainty. The depolarization can occur on synchrotron sidebands. This is excluded with a new depolarization after a slight Q_s change which does not affect q_ν. The figure shows the RF frequency of the kicker magnet f_{kick} (top) and the fractional part of the spin tune q_ν (bottom).

The highest polarization value was observed in 1993 with $P = 57 \pm 3\%$ at 44.7 GeV [22]. A minimum polarization of about 3–5$\%$ is required for resonant depolarization. The relation of the spin tune and the beam energy is given by

$$E_{beam} = \frac{m_e c^2}{a} \cdot \nu = 440.6486(1) MeV \cdot \nu + \delta \tag{3.4}$$

where $m_e c^2$ is the electron rest mass. Due to higher order effects of the spin motion, ν is no longer strictly proportional to E_{beam} and the true energy can be shifted by δ. The estimated error is $\delta = 0.2$ MeV at 45.6 GeV [22, 23]. An experimental verification with limited accuracy gave an upper limit of $\delta =$1.1 MeV [19].

Since 1996 the dipole field is continuously monitored by NMR probes during physics data acquisition. These instruments determine the magnetic field using the *N*uclear *M*agnetic *R*esonances. The left diagram in Fig. 3.5 shows the position of an NMR probe in a dipole magnet. During the 1997 LEP run sixteen NMR probes were installed in the eight LEP arcs for bending field recording. Their intrinsic precision is better than $5 \cdot 10^{-6}$. However, the field measurements are limited to an accuracy of $\Delta E/E \cong 10^{-4}$ because the field measurements are very local and do not perfectly represent the integrated magnetic field of the LEP concrete-iron dipole magnets.

Besides the local field measurements of the NMR, a special *flux loop* system spans the whole ring. It consists of induction coils which are installed in each dipole magnet. The voltage induced in the loop during a magnet cycling is used to monitor the magnetic field of the dipoles. The precision of this method is about $\Delta E/E \cong 10^{-4}$. The flux loop is divided into eight induction coils. Each coil covers the bending magnets of one octant. In total 96.5% of the integrated bending field is considered. The principle of the flux loop is illustrated in the right diagram of Fig. 3.5. Both magnetic measurements have to be calibrated with resonant depolarization. They are explained in detail in [24]. Resonant depolarization was used at LEP I at a beam energy of 45 GeV [24]. As the spin polarization disappears beyond 60 GeV this method is not available at LEP II beam energies of 90 GeV [25]. As a consequence the magnetic instruments (NMR probes and flux loop) can only be

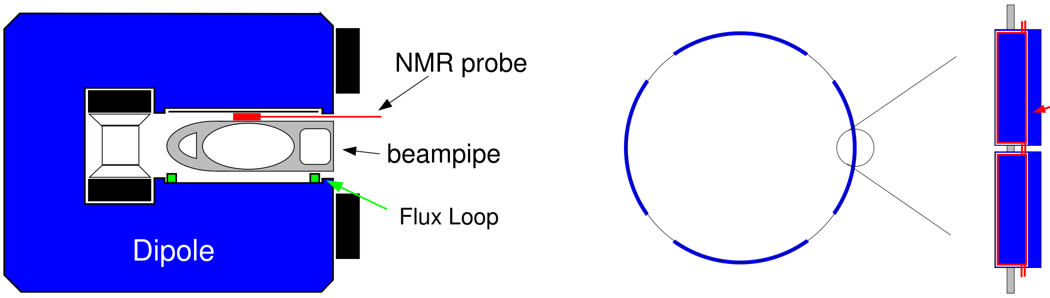

Figure 3.5: left: NMR probe position in a LEP-dipole magnet; right: principle of the flux loop.

calibrated at lower energies with resonant depolarization. The beam energy uncertainty is given by extrapolating the calibration results to the physics beam energy. The extrapolation error depends on the linearity of the calibration range and on the distance between the highest calibration point and the maximum energy (see Fig. 3.6).

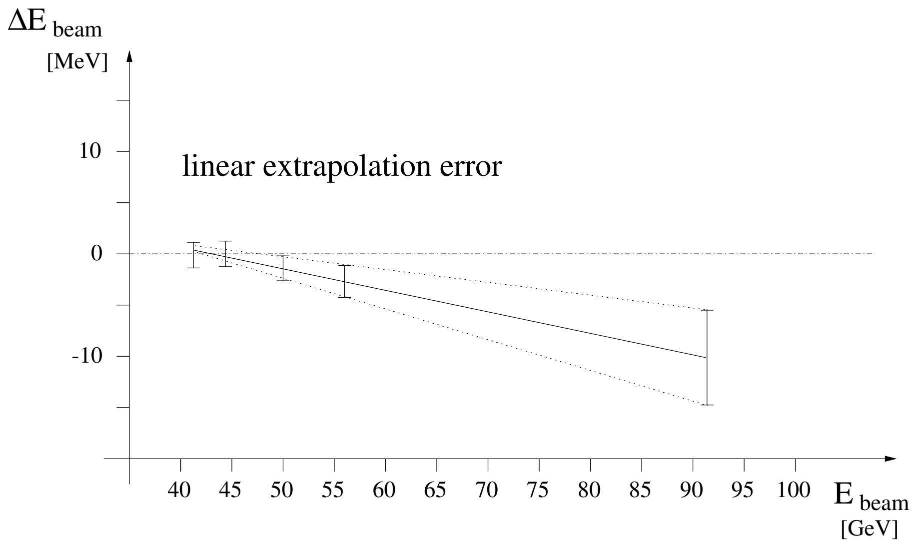

Figure 3.6: Schematic diagram of the difference ΔE_{beam} of the NMR and resonant depolarization beam energy estimates as function of the beam energy. The measured differences are available in the energy range between 41–60 GeV. The lines indicate the extrapolation and its uncertainty to the beam energy of 91.5 GeV.

3.3 Methods of avoiding Depolarizing Effects

During the 1996 LEP run several attempts were made to observe polarization at higher energies. A calibration at 50.0 GeV was only possible in one fill [26]. As a large lever arm is needed to prove the linear extrapolation method between the calibrated energies to the maximum energy and to reduce the beam energy error at 90 GeV, an effort was made to enhance the polarization at energies 50–60 GeV [27]. First of all, the solenoids of the LEP experiments are switched off because their field depolarizes the beam. Although it is possible to compensate their effects, the bumps used for this purpose have a strong depolarizing effect at higher energies as they create a large vertical dispersion.

3.3.1 Tune Settings

The tune settings play an important role in order to achieve a high polarization level. To minimise the influence of the very strong integer resonances [14, 21] the fractional part of the spin tune has to be around 0.5. The synchrotron tune Q_s is set to a fraction of an integer $Q_s = 1/N$ during energy calibration such that the synchrotron sidebands of the integer resonances overlap. The smaller the Q_s value becomes, the higher the order of the synchrotron resonance around the fractional spin tune 0.5. This is a preferable situation since the strength of synchrotron resonances decreases from one order to the next with λ^2 (see Section 2.3). On the other hand a larger value of Q_s is chosen at higher energies to compensate the effect of the increased energy spread σ_E (see Eq. 2.67). In addition, a sufficient beam lifetime must be secured and requires a larger synchrotron tune when the beam energy is increased. The fractional parts of the betatron tunes q_x, q_y are set to be approximately a multiple of the synchrotron tune. In this case all synchrotron and betatron resonances overlap and the number of "separated" spin resonances is reduced. Such tune settings cannot be used in a machine since they correspond to very dangerous synchro-betatron resonances

$$k \cdot Q_{x,y} = n \cdot Q_s + m; \qquad k, n, m \in \mathbb{N} \tag{3.5}$$

leading to almost immediate beam loss or very poor beam lifetimes. During polarization experiments the operator tries to get as close as possible to the desired tune settings. The fractional part of the tune settings which have been used during the last LEP run are summarised in Table 3.2.

Energy	ν	Q_s	q_x	q_y
41.2 GeV	93.5	0.072	0.113	0.228
44.7 GeV	101.5	0.067	0.107	0.231
50.0 GeV	113.5	0.083	0.106	0.230
55.3 GeV	125.5	0.111	0.135	0.256
or		0.091	0.120	0.205
60.6 GeV	137.5	0.111	0.135	0.256

Table 3.2: Optimum tune settings at the polarization energies. The table summarises the fractional part of the tune settings which have been used during energy calibration. They are chosen to obtain the best possible overlap of the spin resonances and at the same time to avoid beam resonances.

3.3.2 Influence of different Optics

Every imperfection of the ring excites resonances and causes a spin precession with a tilt to the n-axis. Misaligned quadrupoles give a deflection dependent on the beam position. To first order, the best possible polarization is obtained when the r.m.s. kick strength coming from the quadrupoles is as small as possible. The quantity to be minimised is

$$\sqrt{\beta_{F_{quad}} < \beta > k^2_{F_{quad}} + \beta_{D_{quad}} < \beta > k^2_{D_{quad}}} \tag{3.6}$$

where k_i denotes the strength and β_i the value of the β-function of the focusing and defocusing quadrupole magnet of the arc cell. $< \beta >$ is the average beta function of the FODO cell (see

Section 2.1). It should be noted that the expression is only approximate. Reducing the phase advances, and therefore the k, is compensated by a larger beta function. For this reason the gain to be expected for very low phase advances is not very large. A restriction is given by the horizontal emittance. A smaller horizontal phase advance causes a larger horizontal emittance which limits the minimal horizontal phase advance to $60°$. A drawback of weaker horizontal focusing is the larger Q_s required to guarantee a sufficient beam lifetime. A weaker focusing leads to a larger dispersion which enhances the effects of synchrotron resonances. An optics with a phase advance of $60°$ in both planes (60/60) was finally selected since it seemed to give the best compromise [28]. The comparison of the 60/60 optics with the 90/60 optics which is used for physics is presented in Section 3.6. As a consequence of the use of a different optics for polarization measurements at higher energies, a cross-calibration with the physics optics is required. The cross-calibration was made at 44.7 GeV.

3.3.3 Harmonic Spin Matching

Integer resonances have strong depolarizing effects because they excite all betatron and synchrotron spin resonances (see Section 2.3). The polarization level can be significantly increased by compensating the influence of the integer resonances. The related technique is called *Harmonic Spin Matching* [29]. From the T-BMT Eq. 2.34 follows that the spin only precesses in the bending field of a storage ring. A Fourier analysis of the vertical orbit in the spin precession frame expresses the vertical orbit as a function of the bending angle and gives the strengths of the sine and cosine components of the integer resonances. In particular, the components a_k, b_k of harmonic k are

$$a_k = \frac{1}{\pi}\sum_{i=1}^{N_{BPM}} y_i \cdot \Delta\theta_i \cdot cos(k \cdot \theta_i) \tag{3.7}$$

$$b_k = \frac{1}{\pi}\sum_{i=1}^{N_{BPM}} y_i \cdot \Delta\theta_i \cdot sin(k \cdot \theta_i) \tag{3.8}$$

$$c_k = \sqrt{a_k^2 + b_k^2} \tag{3.9}$$

where N_{BPM} is the number of the single vertical orbit position measurements y_i; and θ_i is the integrated bending angle at that BPM [21]. The influence of different bending angles between three BPMs is taken into account by the local bending at the orbit measurement $\Delta\theta_i = (\theta_{i+1} - \theta_{i-1})/2$. The strength c_k is obtained from the spin-orbit motion coupling vector $\gamma\frac{\partial\vec{n}}{\partial\gamma}$ [23]

$$(\gamma\frac{\partial\vec{n}}{\partial\gamma}) \propto \nu^2 \sum_k \frac{c_k^2}{(\nu - k)^4}. \tag{3.10}$$

In addition to Eq. 3.10 the spin-orbit motion coupling also depends on the harmonic content of the vertical dispersion D_y [23]

$$(\gamma\frac{\partial\vec{n}}{\partial\gamma}) \propto \nu^2 \sum_k \frac{D_{y_k}^2}{(\nu - k)^4}. \tag{3.11}$$

At LEP, a harmonic compensation of the vertical dispersion is not established.

Eq. 3.10 shows that the integer resonances k next to the spin tune ν have the strongest influence. Their effect scales with the square of the spin tune. The strength of any components decreases with the difference to the spin tune by the power of four (see Eq.3.10). This means that the polarization level can be increased by compensating the four Fourier components of the two integer resonances next to the spin tune using precalculated closed orbit bumps which have a known effect on the Fourier spectrum. The *Harmonic Spin Matching* can be used in two different ways [22]:

Empirical HSM

The maximum level of polarization can be found by scanning the orbit bump amplitudes empirically until the maximum polarization is achieved for each Fourier component. This method is called empirical HSM. It allows the best compensation of the integer resonances. Unfortunately this can be a lengthy procedure because the polarization build up time is about 350 minutes at 45 GeV. This means that the effect of each bump amplitude change can be evaluated only after 15 minutes.

Deterministic HSM

It is possible to calculate the Fourier spectrum of the vertical orbit and compensate them using adequate amplitudes of the harmonic bumps. This procedure is known as deterministic HSM. Deterministic HSM is preferable since it requires less time than empirical HSM. The quality is limited by the accurate knowledge of the beam position. Errors on the vertical beam positions y_i are shown in Fig. 3.7. They are divided into three types:

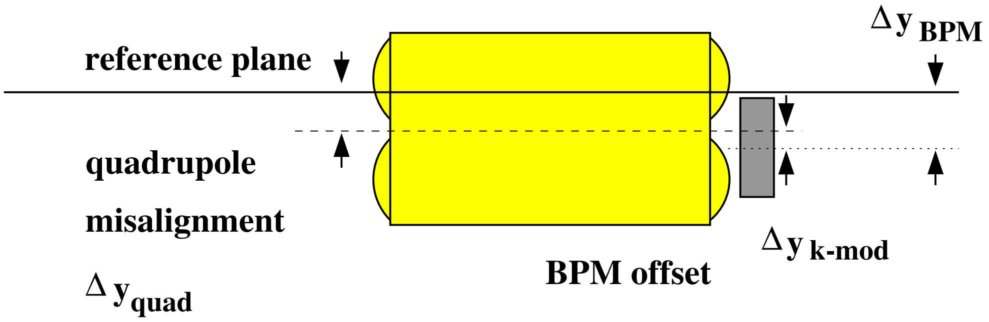

Figure 3.7: Beam position monitor misalignment with respect to the reference plane.

- The quadrupole misalignment with respect to the LEP reference plane.
- The geometric BPM offset relative to the magnetic centre of the adjacent quadrupole.
- The electronic offset in the BPM signal processing chain.

The effects of these error sources are studied in Chapter 3.3.3. The quadrupole positions of LEP are measured during every shutdown. The misalignment data is analysed in Section 4.2. Both errors concerning the beam position monitors are detected at LEP with the *k-modulation* technique. It is a dynamic beam based measurement which has been developed over the last four years [30, 31]. Its results and principle are presented in Section 4.3.

Following Nyquist's law that at least two points per period are required to detect a harmonic oscillation, the number of available beam position monitors limits the highest measurable spin harmonic which corresponds to the Nyquist frequency f_{Ny} (at LEP f_{Ny} is given by $\nu = 138.8$). The number of working BPMs and the $\Delta\theta_i$ in the arcs and dispersion suppressors add further uncertainties to the harmonic calculations (see Section 4.1).

Implementation of HSM

The local bumps which are used to compensate the harmonic components of the integer resonances are evaluated and tested with simulations (see Chapter 3.3.3). The formulae used to calculate the bumps are given in Appendix A, Section A.1. At beam energies beyond 45 GeV the most efficient

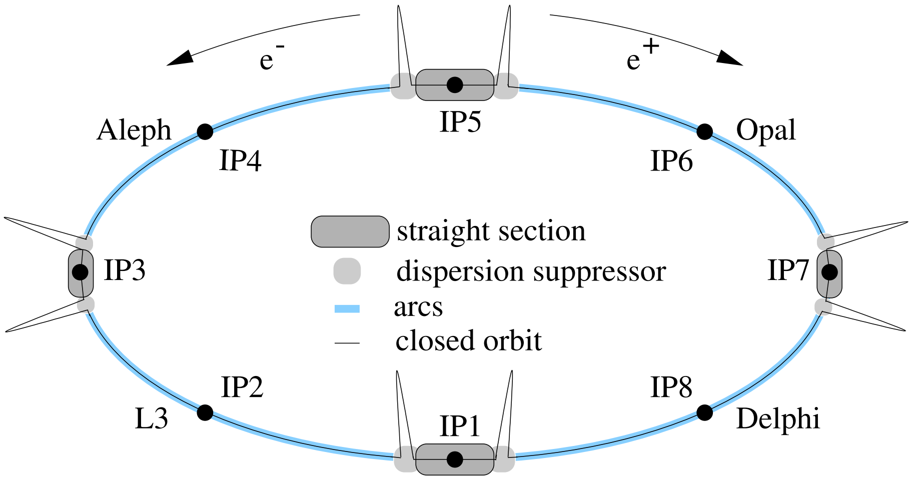

Figure 3.8: Positions of the local bumps to compensate integer resonances at LEP; the detailed tunnel structure is only shown for the odd interaction points (IP) as the HSM bumps are implemented there.

bumps with relatively small amplitudes $\lesssim$5 mm use three neighbouring corrector magnets in the dispersion suppressors. Two corrector magnets bumps in the arcs which gave very successful results at 45 GeV [21] become less effective at higher energies. In order to form a two-corrector bump, a phase advance of a multiple of π between both correctors is required. With a vertical betatron phase advance of $60°$ this means that a π phase advance corresponds to three standard cells between both correctors. At higher energies ($\approx$ 60 GeV) the spin precession phase advance between two successive vertical correctors approaches π, i.e. 3π between the chosen correctors. Thus, the additional deflection of the second corrector magnet which closes the local orbit bump also cancels the effect in the spin precession and no harmonic compensation is possible (see Section 3.8). In the dispersion suppressors the betatron phase advance is not regular and more correctors are available for harmonic compensation at higher energies.

Eight bumps each using three corrector magnets (three-corrector bumps, see Appendix A, Section A.1 are required for the harmonic compensation in order to adjust four Fourier components (sine and cosine of two integer resonances). Fig. 3.8 shows a diagram of the bump positions. The orbit bumps are implemented in the dispersion suppressors symmetrically around the interaction points IP1, IP3, IP5 and IP7. The corrector magnets CV.QL16, CVA.QL14 and CVA.QL12 form the bump.

chapterSimulation Studies of Polarization Polarization experiments at LEP are incompatible with colliding beam conditions for physics for two reasons. First, the beam-beam interaction is strongly depolarizing and the beams must be separated to observe any polarization. Secondly, LEP is presently operated at a beam energy of beyond 90 GeV, well above the reach of polarization. To optimise the use of the machine time dedicated to polarization and energy calibration, it is important to study the influence of various machine parameters on polarization in advance. In particular, the choice of the polarization optics relied on simulations. The comparison of simulations and polarization measurements gives an idea of the simulation quality and is presented in Section 5.3.

All simulations are based on the program package MAD (*M*ethodical *A*ccelerator *D*esign) [32], a program widely used for machine studies and design. MAD is a tool for charged-particle optics in alternating-gradient accelerators and beam lines and has been developed at CERN. For polarization purposes MAD contains an interface to SITF-SODOM [33]. These programs calculate the polarization level in storage rings using the closed orbit evaluated with MAD. The optics functions such as the beta function given by MAD are in very good agreement with the measurements in the real machine, i.e. optics calculations or orbit bumps behave in the predicted way (see Section 5.1). Most polarization simulations for this study were made with the SITF program [34].

3.4 Calculation of the Polarization Level

Several algorithms have been developed to simulate the equilibrium polarization level. Only those which calculate the time independent final polarization level have been used. Spin tracking programs like SITROS [35] have not been considered. Linear polarization simulations are sufficient for many problems. They allow the estimation of important parameters and the comparison of different machine settings. Non-linear polarization models are essential in order to get a realistic and quantitative view. The measured polarization values and the simulation results are compared in Section 5.3.

SITF

SITF is based on an algorithm introduced by Chao [36] and coded by Ackermann, Kewisch and Limberg [34]. It calculates the equilibrium polarization from the first order perturbation theory. Using the closed orbit given by MAD, a one turn spin map is calculated taking linear orbit perturbations into account. $\vec{n}$ and $\vec{d}$ are evaluated including integer and linear spin resonances (see Appendix A, Section A.2).

BESSEL

The most important non-linear resonances are the synchrotron sidebands around the integer resonances (see Section 2.3). The SITF results are fitted to get the linear resonances strengths (see Appendix A, Eq. A.12 and A.14). The input data for the program BESSEL written by Böge [37] is given by the fit results, the spin tune modulation index λ^2 (see Eq. 2.67) and the orbit tunes. BESSEL calculates analytically the synchrotron sidebands using modified Bessel functions (see Appendix A, Eq. A.11 and A.13).

SODOM

Yokoya proposed another more general model to calculate the non-linear influence on the spin motion [38]. In SODOM the $\vec{n}$-axis solution is numerically calculated for non-emitting particles for every position of the storage ring. This formalism avoids the high order perturbation theory. In order to calculate $\vec{d}$ the direction of $\vec{n}$ is slightly varied in the phase space. $\vec{d}$ is derived by a Fourier analysis of each $\vec{n}$ modification. As the higher order calculations are very time consuming, SODOM was mainly used to cross-check the SITF/BESSEL results.

3.4.1 Simulation Model

In MAD, field and position errors can be assigned to every element of the accelerator. The closed orbit is calculated by iterations. It can be obtained for a non-radiating particle or for a radiating particle once the RF voltage has been fixed. For numerical reasons the closed orbit is first calculated considering the positions, strengths and errors of the linear elements in the accelerator. Numerical iterations are made to reduce the beam displacements in both planes after including the non-linear elements such as sextupoles. The polarization subroutines and Fourier analysis programs only use the closed orbit data to simulate the *Harmonic Spin Matching*. In order to estimate the optimised deterministic HSM, a distribution width of the quadrupole misalignment of σ_{QUAD} =150 μm and a BPM offset uncertainty of σ_{BPM} =50 μm are assumed. The quadrupole positions are assigned randomly. The vertical BPM position is given by the adjacent quadrupole position plus the random distributed offset. The same procedure is made to assign the vertical sextupole position. Their Gaussian distributed offset is added to the adjacent quadrupole position and has a width of σ_{SEXT} =40 μm. HSM is performed by calculating the Fourier components only with the vertical readings at the beam position monitors. For the simulation of the empirical HSM, the vertical beam position at the middle of every bending magnet is used to scale the HSM bump amplitudes. This calculation is much more precise since there are about 1800 bending 2-core magnets compared to 500 BPMs. The parameters used for the simulations are listed in Table 3.3. All field and position errors are set randomly according to a Gaussian distribution with the width given in Table 3.3. To get a realistic result, 10 different seeds are chosen for each simulation which reduces statistical fluctuations. The spin polarization is finally averaged over the fractional spin tune band 0.45–0.55 (11 points). It follows that every linear polarization value given in this chapter is based on 10 SITF runs and averaged over the range 0.45–0.55 in spin tune.

3.4.2 Linear and non-linear Simulations

Linear polarization simulations are sufficient to estimate important parameters and to compare different machine conditions. Non-linear polarization models are, however, crucial to get a realistic impression. In Fig. 3.10 the polarization level P between two integer resonances is plotted versus the spin tune ν for the linear SITF result and for the synchrotron sidebands (BESSEL result).

The non-linear results are derived from a fit to the SITF output, for which the linear results are averaged. SITF calculates the depolarization time τ_{d_i} for each pair of linear resonances between two integers and for the combination τ_S. Following Eq. 2.45 the depolarizing effect of a resonance i can be expressed as the ratio τ_p/τ_{d_i}. According to Appendix A, Eq. A.12 and A.14 the strength of each linear resonance pair $i = s, x, y$ in an integer spin tune interval are fitted with the two parameter function

$$\frac{\tau_p}{\tau_{d_i}} = \frac{S_i^1}{(q_\nu + q_i)^2} + \frac{S_i^2}{(q_\nu + 1 - q_i)^2} \tag{3.12}$$

Number of machines	10
Spin tune range for $< P >$	0.45-0.55 (11 points)
R.m.s. of quadrupole misalignment	150 μm
R.m.s. of sextupole misalignment	40 μm
R.m.s. of pickup offset	50 μm
R.m.s. of bending tilt	24 μrad
R.m.s. of quadrupole tilt	24 μrad
R.m.s. of sextupole tilt	24 μrad
R.m.s. of relative bending field error	$7.0 \cdot 10^{-4}$
R.m.s. of relative quadrupole field error	$3.0 \cdot 10^{-4}$
R.m.s. of relative sextupole field error	$0.5 \cdot 10^{-4}$
Orbit corrections to target r.m.s.	$< x >$=400 μm, $< y >$=200 μm
Dispersion for 60/60 optics	$< D_x >\approx$1.1 m, $D_{y_{rms}}$ $\approx$0.01 m

Table 3.3: Machine parameters for the simulations.

where S_i^1, S_i^2 are the fitted resonance strengths, q_i refers to the fractional part of the orbit tunes and q_ν to the fractional part of the spin tune. The fit of the linear synchrotron resonances is used to calculate the synchrotron sidebands of the integer resonances whereas the fits of the linear betatron resonances give the input for the synchrotron sideband calculation of the betatron resonances. According to the fit results, the first order synchrotron resonances are stronger than the betatron resonances by an order of magnitude. A fit example is given in Fig. 3.9. BESSEL calculates the

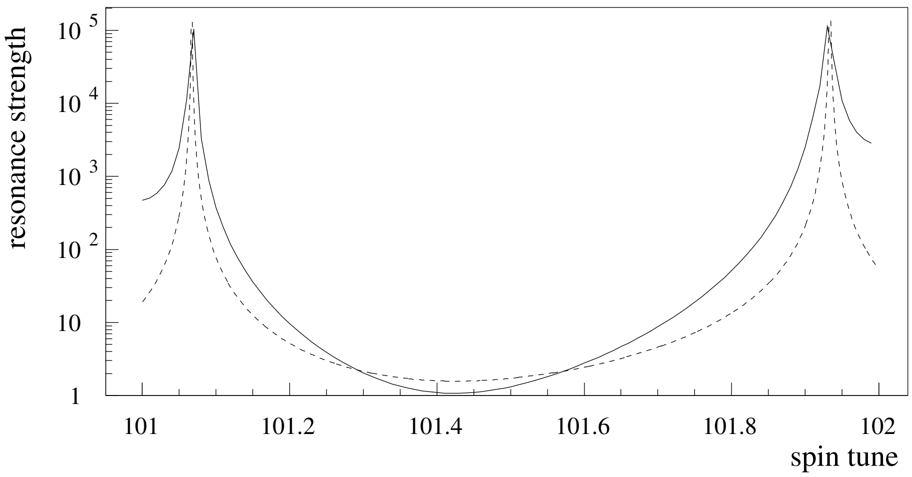

Figure 3.9: Fit example of the linear synchrotron resonances at 44.7 GeV for the 60/60 optic. The solid curve is the SITF result whereas the dashed line indicates the fit. One can see that the quadratic fit expresses only approximately the SITF curve calculated with first order perturbation theory.

synchrotron sidebands strengths in terms of a depolarizing time τ_{B_i} as a function of the linear resonances strengths S_i^1, S_i^2, the tune modulation index λ^2 and the fractional part of the tunes. The three different τ_{B_i} are combined

$$\frac{1}{\tau_{B_{TOT}}}(\nu) = \sum_{i=1}^{3} \frac{1}{\tau_{B_i}}(\nu). \tag{3.13}$$

The envelope $P(\nu)$ between two integer resonances is evaluated by

$$P(\nu) = \frac{92.4\%}{1 + \frac{\tau_p}{\tau_{B_{TOT}}}(\nu) + \frac{\tau_p}{\tau_S}(\nu)}. \tag{3.14}$$

An example of the linear and non-linear simulations at two energies is given in Fig. 3.10. The

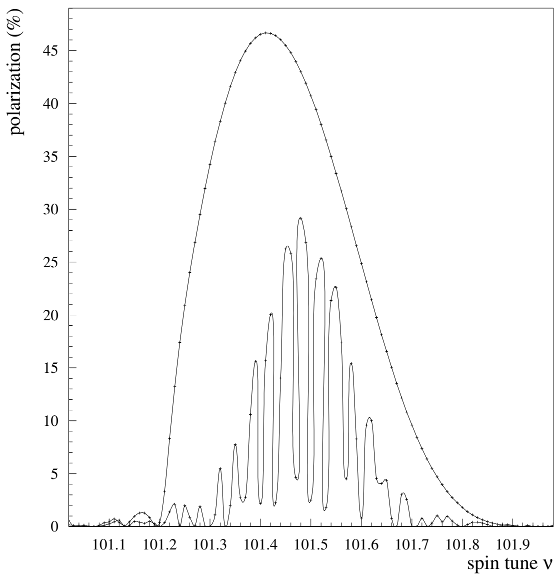

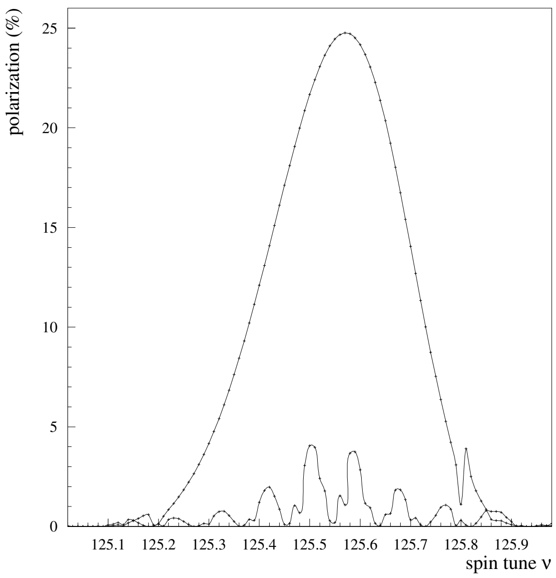

Figure 3.10: Comparison of linear and non-linear polarization calculations at 44.7 and 55.3 GeV for the 60/60 optics. The linear curve only includes the influence of the linear resonances and gives a much higher polarization level at the fractional spin tune 0.5. The difference between the linear and non-linear strengths scales with λ^2. The polarization curves are not symmetric around the fractional spin tune 0.5 because the enclosing integer resonances differ in their strength.

non-linear model differs by a denser array of resonances. The reduction of the polarization level envelope is much more important. The difference is a factor of 1.5 at 44.7 GeV and 6 at 55.3 GeV. This is a consequence of the stronger synchrotron sidebands which scale with the spin tune modulation index. In this case λ^2 increases by a factor of 2.3 from 44.7 to 55.3 GeV. In addition, the synchrotron tune at the higher energy is about 50% larger.

3.5 Energy Dependence

Since the strength of the integer and linear resonances scales with γ^2 (see Eq. 3.10) and the strength of the synchrotron sidebands scales with γ^4 (see Eq. 2.67) calibrations with resonant depolarization become much more difficult beyond 45 GeV. The possibility of finding polarization decreases rapidly with energy. Fig. 3.12 demonstrates the required improvement of HSM from 50–60 GeV.

The polarization level P is approximated following Eq. 2.54 and 3.7 by the depolarizing strength of the integer resonances k, k+1 next to the spin tune

$$P = \frac{P_{max}}{1 + \delta + d \cdot (c_k^2 + c_{k+1}^2)} \tag{3.15}$$

where δ expresses a reduction in the achievable equilibrium polarization level, $P(\infty) = P_{max}/(1+\delta)$, d is the fitted resonance strength and $c_k = \sqrt{a_k^2 + b_k^2}$. An example of the fitted sine component b_{113} is given in Fig. 3.11.

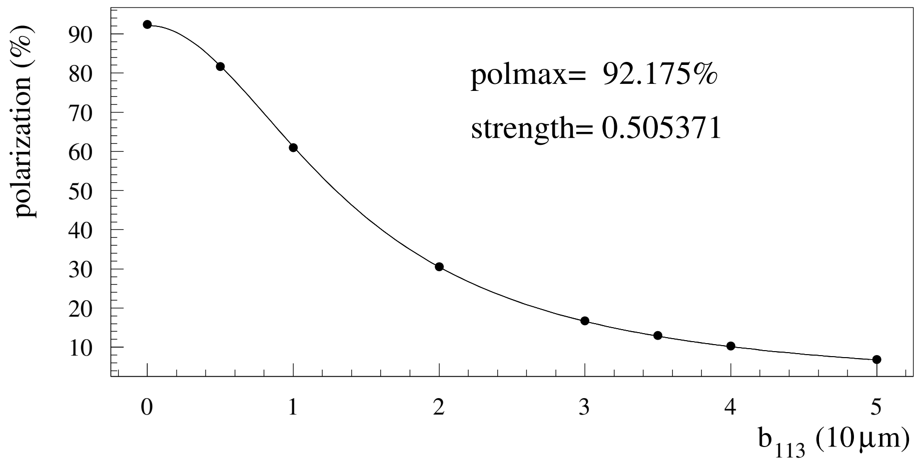

Figure 3.11: Dependence of the polarization level on the sine component b_{113} for a perfect ring. The fit parameters are also listed in the drawing. The achievable polarization is 92.175% and the strength is derived to be $d = 0.505$.

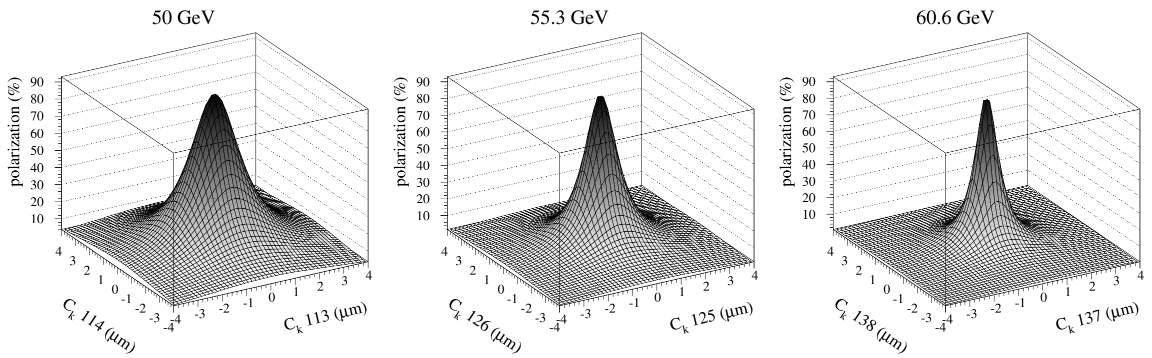

Figure 3.12: Polarization dependence on the strength of integer resonances next to the spin tune at 50.0, 55.3 and 60.6 GeV assuming a perfect storage ring. Although under these conditions P_{max} remains energy independent, the probability of finding polarization diminishes if the resonance compensation is not perfect since the width of the polarization area in the resonance phase space decreases with energy.

The result of these fits are shown in Fig. 3.12 for a perfect machine where $P_{max} = 92.4\%$. For a more realistic model (see Fig. 3.13) which includes quadrupole misalignment, the highest polarization level P_{max} is significantly reduced. At 60.6 GeV the volume (area) in the space of the spin harmonics where a sufficient polarization level for energy calibration can be observed is very small. A random search for polarization by empirical HSM would be extremely difficult and lengthy since the observed level is most of the time in the noise range of the polarimeter. A precise deterministic HSM is required to enable polarization observation. The level can be optimised afterwards by empirical HSM.

At energies significantly higher than 45 GeV non-linear resonances and particularly the synchrotron sidebands are very strong and limit the equilibrium level of polarization as it is shown

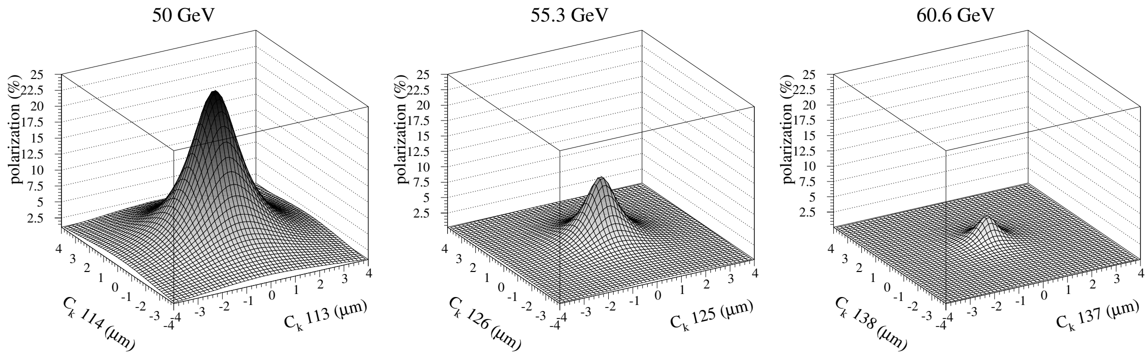

Figure 3.13: Polarization dependence on the strength of integer resonances next to the spin tune for a storage ring with imperfections. P_{max} decreases from 25% at 50.0 GeV to 11% at 55.3 GeV and 4.5% at 60.6 GeV.

in Fig. 3.14. A tool has been developed to evaluate the best tune settings during polarization experiments. Fig. 3.14 is one example of the program output. It shows that at higher energies the observation of polarization is much more sensitive to orbit and tune changes than at LEP I beam energies since the maximum level is much lower.

3.6 Comparison of Polarization and Physics Optics

A polarization optics [28] with a $60°$ phase advance in both transverse planes has been developed to reduce the vertical kicks and to avoid using the super-conducting quadrupoles left and right of the four LEP experimental detectors (QS0s). The optics used for the physics is matched with $90°$ phase advance in the horizontal plane and $60°$ phase advance in the vertical plane. The

50.0 GeV	Q_s	P_{lin}	P_{det}	P_{emp}
		[%]	[%]	[%]
60/60	0.076	42.0 ± 1.6	9.2 ± 1.9	16.3 ± 3.3
90/60	0.076	35.3 ± 1.6	7.3 ± 1.5	13.1 ± 2.6
	0.063	38.1 ± 1.6	8.1 ± 1.6	14.2 ± 2.8

55.3 GeV	Q_s	P_{lin}	P_{det}	P_{emp}
		[%]	[%]	[%]
60/60	0.091	37.0 ± 1.6	6.5 ± 1.3	11.5 ± 2.3
90/60	0.091	27.3 ± 1.6	4.1 ± 0.4	7.1 ± 1.4
	0.063	37.1 ± 1.6	4.2 ± 0.5	8.4 ± 1.7

Table 3.4: Results of non-linear polarization simulations for the 90/60 and 60/60 optics at 50.0 GeV (top) and 55.3 GeV (bottom). The table contains the Q_s values; the calculated polarization with deterministic HSM in the linear P_{lin} and non-linear model P_{det}; the polarization with empirical HSM P_{emp}. The deterministic HSM assumes the uncertainties of the vertical readings which are given in Table 3.3.

simulated polarization levels of both optics at 50.0 and 55.3 GeV are summarised in Table 3.4. These energies are chosen as an example for the general result that the 60/60 optics always shows

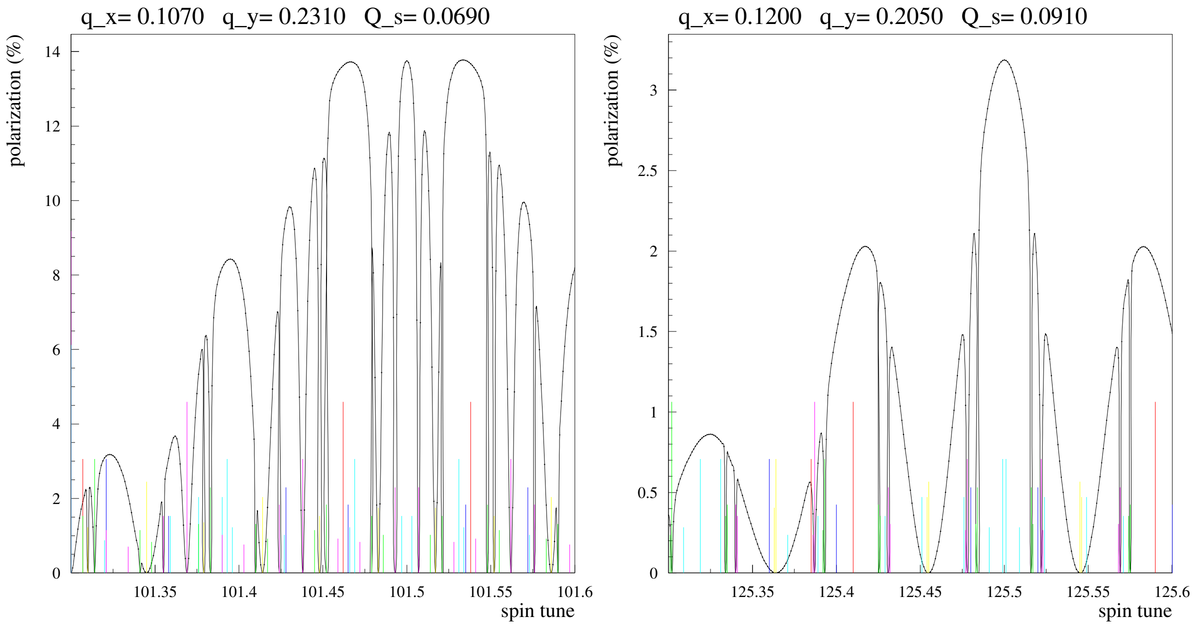

Figure 3.14: Tune settings at 44.7 and 55.3 GeV and the predicted polarization level versus spin tune. The different spin resonances are drawn as lines. The line length indicates the resonance order. The polarization value is printed with a solid curve as a function of spin tune. At both energies the envelope due to the integer resonance strengths is visible. The synchrotron sidebands occur stronger at the higher energy and limit the polarization value. In the given example the maximum level at 44.7 GeV is 14% compared to less than 4% at 55.3 GeV. The width of the highest polarization region at the higher energy is much smaller as a consequence of the stronger synchrotron resonances.

a higher polarization level in linear and non-linear simulations. The distribution width of the results of the different seeds is similar for both optics and energies, it is in the order of 5% polarization. It follows that the error of the mean value is 1.6% polarization. Since the linear polarization levels differ by 6.7% at 50.0 GeV and 9.3% at 55.3 GeV, the higher polarization value of the 60/60 optics cannot be explained with statistical fluctuations. The error of non-linear calculations is dominated by the uncertainty of the fit parameters. The relative error of the fitted resonance strengths is about 10%. The sideband calculation itself is analytical. The final error is given by the combination of the BESSEL and SITF output. It leads to an uncertainty of about 20%. The BESSEL algorithm has a systematic limit when τ_d is much larger than τ_p for the highest polarization points. For this reason non-linear calculations are only applied after HSM. The different non-linear results for deterministic and empirical HSM show that the advantage of the 60/60 optics increases with energy. At 55.3 GeV the deterministic HSM value of the 90/60 optics reaches only 63% of the level of the 60/60 optics. The average polarization level in the linear model of the 60/60 optics relative to the 90/60 optics at different energies between 41.2 and 60.6 GeV is shown in Fig. 3.15. The dotted line indicates the difference in the initial polarization without applying HSM. This is very useful in reality to optimise the tune settings before starting HSM.

Apart from the polarization, some parameters of both optics are given in Table 3.5. The required Q_s of the 60/60 optics increases from 44.7 to 55.3 GeV by 50% for a minimum quantum lifetime τ_Q of 100 hours whereas Q_s is almost constant for a sufficient τ_Q with the 90/60 optics. The defocusing quadrupole strength k_{QD} is just slightly smaller in the polarization optics. The focusing strength k_{QF} is reduced by 26%. The r.m.s. values of the vertical dispersion D_y are similar, whereas the average horizontal dispersion $< D_x >$ more than doubles. The highest polarization is achieved when the n-axis points exactly in the bending field direction e_y. The average tilt $\sphericalangle(e_y, \vec{n})$ between e_y and $\vec{n}$ is 31% smaller with the 60/60 optics which was expected according to the simulated polarization values. In summary, the 60/60 optics is expected to give higher polarization despite the fact that Q_s has to be increased. The larger horizontal dispersion does not seem to harm polarization.

Optics	Q_s	x_{rms}	y_{rms}	$< D_x >$	$D_{y_{rms}}$	$\sphericalangle(e_y, \vec{n})$	k_{QF}	k_{QD}
		[mm]	[mm]	[m]	[m]	[mrad]	[m^{-2}]	[m^{-2}]
60/60	0.091	0.40	0.18	1.08	0.026	0.097	0.016036	-0.016041
90/60	0.063	0.40	0.20	0.51	0.024	0.140	0.021736	-0.017765

Table 3.5: Parameters of the 60/60 and 90/60 optics averaged over ten different seeds at 55.3 GeV. The parameters are the result of MAD simulations after orbit corrections.

3.7 Influence of Various Parameters

To understand the results for the 60/60 optics the Q_s influence is simulated separately. The effect of the solenoid fields and their compensation was studied with 90/60 optics.

3.7.1 Synchrotron Tune

Due to the weaker horizontal focusing, the Q_s value increases to maintain the beam lifetimes. For a larger Q_s, the order of synchrotron sidebands near the fraction part 0.5 of the spin tune is lower which leads to a depolarizing effect since the resonance strength decreases with the resonance order. A larger Q_s also diminishes the spin modulation index λ^2. As pointed out in Section 2.3, the synchrotron sidebands strengths scale with λ^2 and get weaker with a larger Q_s which has a positive effect on the polarization. The comparison of the 60/60 and 90/60 optics already indicated that at higher energies the positive effect of a larger Q_s value is stronger. Calculating the maximum polarization value dependent on different synchrotron tunes at 55.3 GeV, this result is confirmed. The polarization level increases slightly with the synchrotron tune from an average value of 7.4% to 8.0%. The spread for a given Q_s is due to changes of the betatron tunes. The tune settings in the calculations follow the conditions given in Section 3.3.1. The simulations assume that the strengths of the linear resonances stay constant with small tune variations. This can be different in reality.

3.7.2 Solenoid Field Compensation

In order to use the energy calibration points of the polarization optics for extrapolation to the physics energy, at least one cross-calibration with the physics optics is needed. This is done at 44.7 GeV with the solenoid magnets switched on to provide machine conditions as similar as possible to a normal physics coast. The spin rotation in each solenoid field is compensated with two bumps using three correctors left and right in the dispersion suppressors of the even interaction points. The bumps are built with correctors CV.QS14, CV.QS16 and CV.QS18. Since the amplitudes are very large, even small and typical optics errors inside the bump create a non-closure that

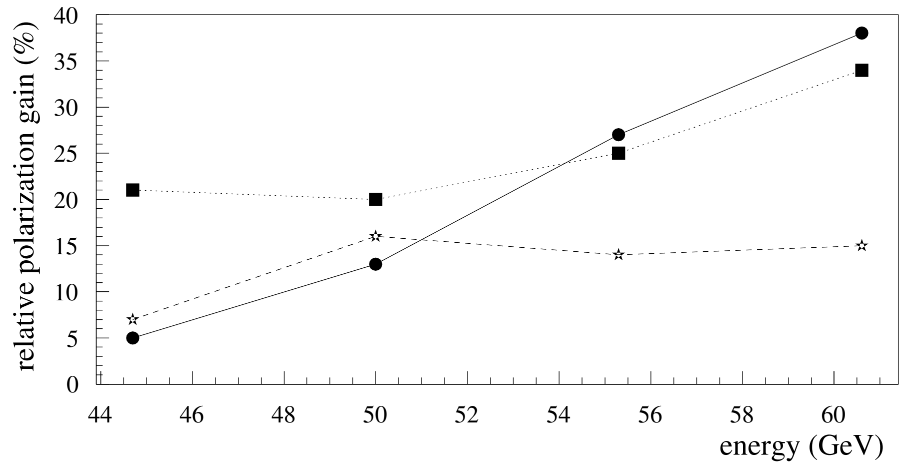

Figure 3.15: Polarization gain of the 60/60 relative to the 90/60 optics from 44.7 to 60.6 GeV in percent. The squares represent the initial polarization curve; the circles refer the deterministic HSM results; and the stars correspond to the level of the empirical HSM.

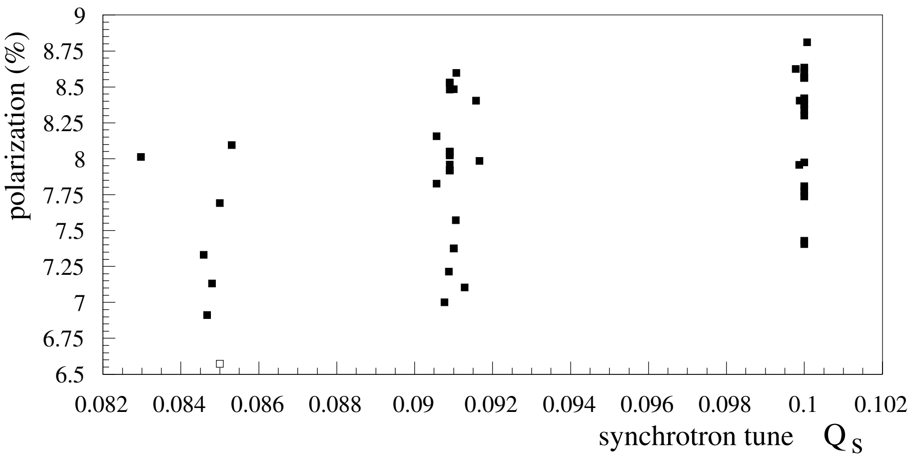

Figure 3.16: Polarization in the non-linear model versus Q_S at 55.3 GeV. The different levels are due to changes of the fractional parts of the betatron tunes. Based on the assumption that the linear resonance strengths remain constant, a larger Q_s has a positive influence.

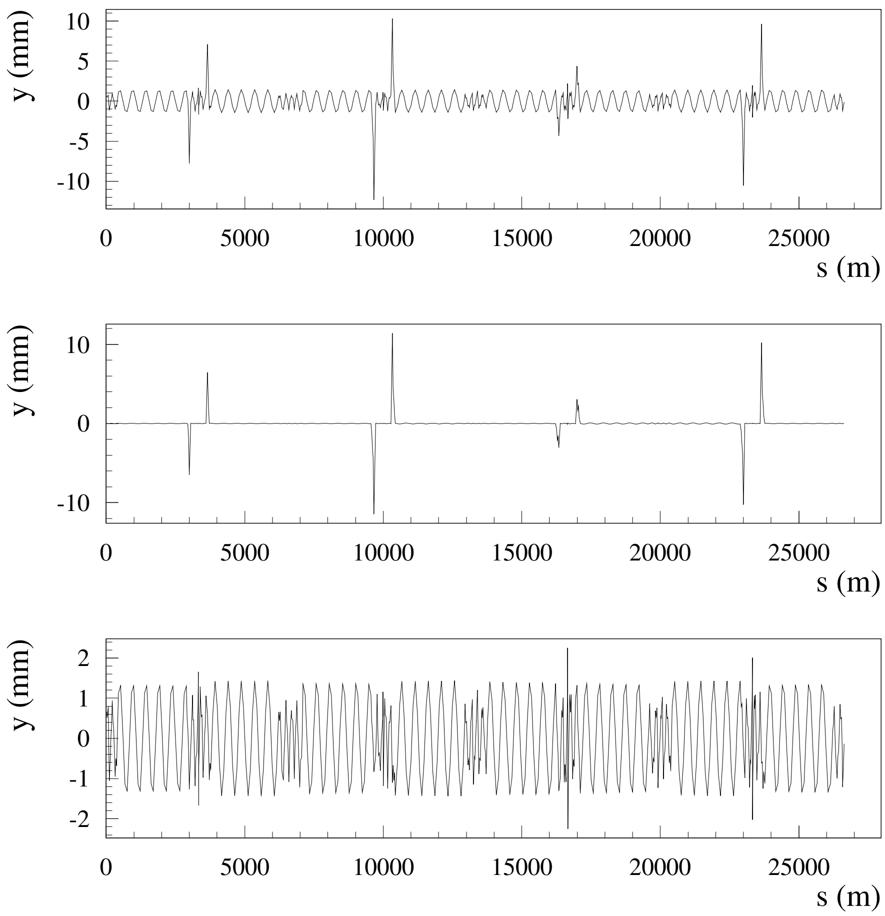

Figure 3.17: Closure of the orbit bumps for solenoid field compensation. Top: the vertical orbit with a betatron oscillation due to non-closed bumps. In the middle: the vertical orbit after bump closure adjustment. Bottom: the difference orbit with the residual betatron oscillation.

propagates as a betatron oscillation into the whole ring (see Fig. 3.17). In the real machine it is not possible to determine where the focusing errors originate and the bump closure is adjusted with a few other orbit correctors. For the same reason it is not easy to simulate this effect and find the best cure, as all magnets (correctors, quadrupoles and dipoles) are involved in the compensating effect of the bump. However, the best solution is to change the strengths of one of the correctors used for the bump to close it. As an example Table 3.6 gives the effect on the polarization of a corrector error of 2%.

The optimised polarization level at 44.7 GeV is 89% instead of 92.4%. As the spin rotation angle in the solenoid field decreases with energy (see Eq. 2.35) the compensation bumps have to be rescaled and optimised for every spin tune. Nevertheless, the achievable polarization level diminishes with energy to 78% at 50.0 GeV, 67% at 55.3 GeV and 41% at 60.6 GeV even for an ideal machine in the linear model. This indicates the limitations of solenoid compensation and proves that the solenoids should be switched off for polarization measurements at higher energies.

IP	4 (ALEPH)			6 (OPAL)		
P	78%	45%	81%	85%	73%	86%
Corrector	CV.QS18	CV.QS16	CV.QS14	CV.QS18	CV.QS16	CV.QS14

Table 3.6: Examples of the polarization reduction for a 2% change of one of the three corrector magnets in the solenoid compensation bumps for the ALEPH and OPAL detectors. It should be noted that this a very large error compared to the tolerances on the correctors ($< 10^{-3}$). In reality the bumps are not closed because the optics functions vary from the design in that area.

3.8 Sensitivity on Errors of the vertical Orbit

As already indicated in Fig. 3.7, the quality of deterministic HSM depends on the quality of the vertical orbit readings. This can be simulated by changing the r.m.s. of the beam position monitor offsets with respect to their adjacent quadrupole. Quadrupole alignment data can also be evaluated.

Efficiency of HSM Bumps

The efficiency of two-corrector π bumps in the arcs and three-corrector bumps in the dispersion suppressors are simulated for different energies in order to judge which kind of local orbit bumps best suits for harmonic compensation. The efficiency is defined by the bump amplitude needed for a Fourier component change of 10 μm. The results are listed in Table 3.7. The π bump amplitudes

Energy [GeV]	44.7	50.0	55.3	60.6
2-corr. y_{max} [mm]	2.2	5.3	10.5	-
3-corr. y_{max} [mm]	2.9	3.6	4.1	5.4

Table 3.7: Amplitude of HSM bumps in the arcs and in the dispersion suppressors.

become unreasonably large at 50.0 GeV whereas the amplitudes of the three-corrector bumps are still acceptable even at 60.6 GeV.

Calibration of HSM Bumps

The use of compensation bumps in the dispersion suppressor is complicated by the fact that the orbit sampling is better in that area and that the bending angle between the beam position monitors changes. The harmonics calculated from the monitor readings must therefore be "recalibrated". The calibration is achieved by calculating the harmonics from the beam position in each dipole (program ORBIT) which is much more accurate and regular since the number of dipoles is very large and since the bending angle per dipole is constant (except from some weak bending magnets in the dispersion suppressors and the injection dipoles). The number obtained from the beam position at the dipoles is then compared to the same calculation done with the BPM readings (program FTAPO). The scaling factor is shown in Table 3.8 for different spin tunes. The factors between FTAPO and ORBIT are dependent on the beta function at the s positions where the beam position is taken and on the spin precession phase advance. This leads to an energy dependence. The statistical scatter of the factors is about 0.4 which corresponds to a relative uncertainty of $20 - 35\%$. Separated scale factors for the dispersion suppressors and the arcs cannot be reasonably introduced since the width of the statistical scatter is too large.

Spin tune	113	114	125	126	137	138
Cosine	1.7	2.1	1.5	1.8	1.4	1.7
Sine	1.7	1.3	1.5	1.2	1.4	1.2

Table 3.8: Normalisation factors for the bump amplitudes to scale the FTAPO sampling to the true harmonics calculated with ORBIT.

3.8.1 Beam Position Monitor Offsets

Fig. 3.18 demonstrates the polarization level dependence on the vertical offsets of the beam position monitors. The horizontal axis shows the BPM offset r.m.s. The initial and deterministic HSM polarization values are improved by more than 50% if the distribution width σ_{BPM} is reduced from 300 to 50 μm. The saturation at 50 μm can be explained by the contribution of the misaligned quadrupoles. For σ_{BPM} >400 μm the harmonic content of the BPM offsets is on average larger than the orbit harmonics. Deterministic HSM can then decrease the initial polarization level. Based on these simulations [39] every BPM offset in the bending area of LEP was determined with *k-modulation*. The measurement principle and its results will be presented in Section 4.3.

3.8.2 Influence of the Quadrupole Misalignment

For the previous HSM simulations a quadrupole misalignment r.m.s. of 150 μm in the vertical plane was assumed. In principle, the real quadrupole alignment data is available and can be used. The ideal orbit is defined by the magnetic centre of the well-aligned quadrupoles. For the case of misaligned quadrupoles, the orbit that passes through the centre of each quadrupole contains kicks (see Fig. 3.19a). These kicks can be reduced if the quadrupole positions are known and the vertical corrector magnets are used to correct the beam to the reference plane (see Fig. 3.19b). This method is not reasonable if the quadrupoles are shifted in a systematic way. In this case the attempt to move the orbit to the reference plane would produce larger kicks than those due to the misalignment.

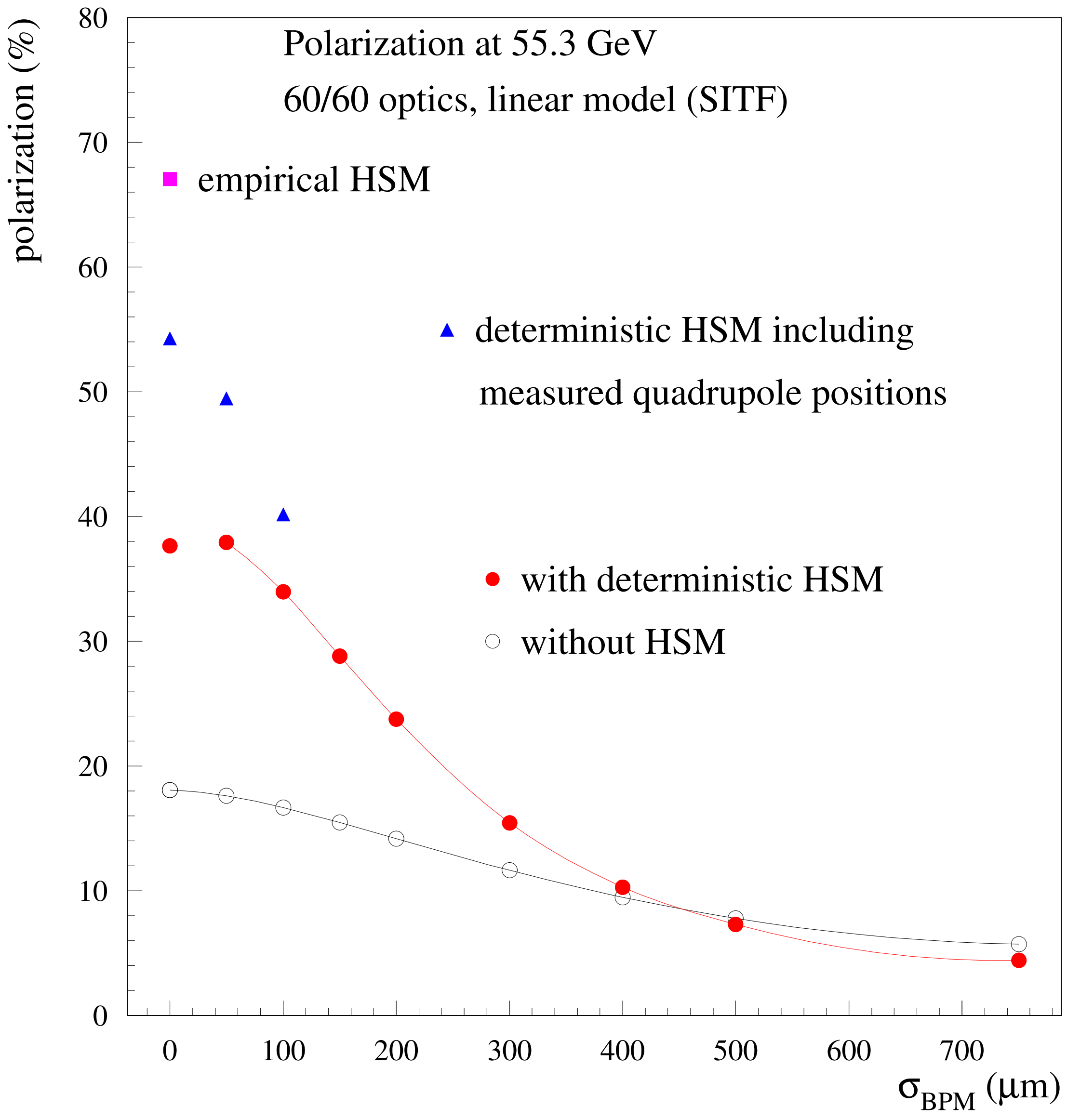

Figure 3.18: Polarization versus BPM offset r.m.s. for a linear model (60/60 optics at 55.3 GeV). The open circles show the initial polarization whereas the filled circles represent the polarization with deterministic HSM. Reducing the uncertainty of the vertical quadrupole positions, deterministic HSM can be improved (triangles). The polarization which is obtained with empirical HSM is also shown.

Besides the direct use of the alignment data, the harmonic contribution can be calculated and its harmonics can be added to the HSM bump amplitudes without changing the orbit around the machine. In simulations it is not possible to differ between both methods. MAD corrects the orbit to the centre of the beam position monitors. Thus, assigning misplacements to the quadrupoles and leaving the BPMs centred around the reference plane with their offset distribution is equivalent to using the alignment data to improve the deterministic HSM. Similar results are obtained by reducing the width of the error distribution of the quadrupoles. The impact of the alignment data is given in Fig. 3.18 (triangles). The achievable polarization increases by about 30% when the r.m.s. of the quadrupole position error is diminished from 150 μm to a negligible value.

The real measurement data were taken for the quadrupole position as simulation input. A measurement inaccuracy of 40 μm was added randomly to the quadrupole displacement. The Fourier components of the alignment data remain similar when the lowest harmonics are removed or the data is smoothed. As a consequence, the simulated polarization level only changes in the range of the statistical error when the differently treated alignment files are used. This justifies the choice of a quadrupole position error r.m.s. of 150 μm for the simulations.

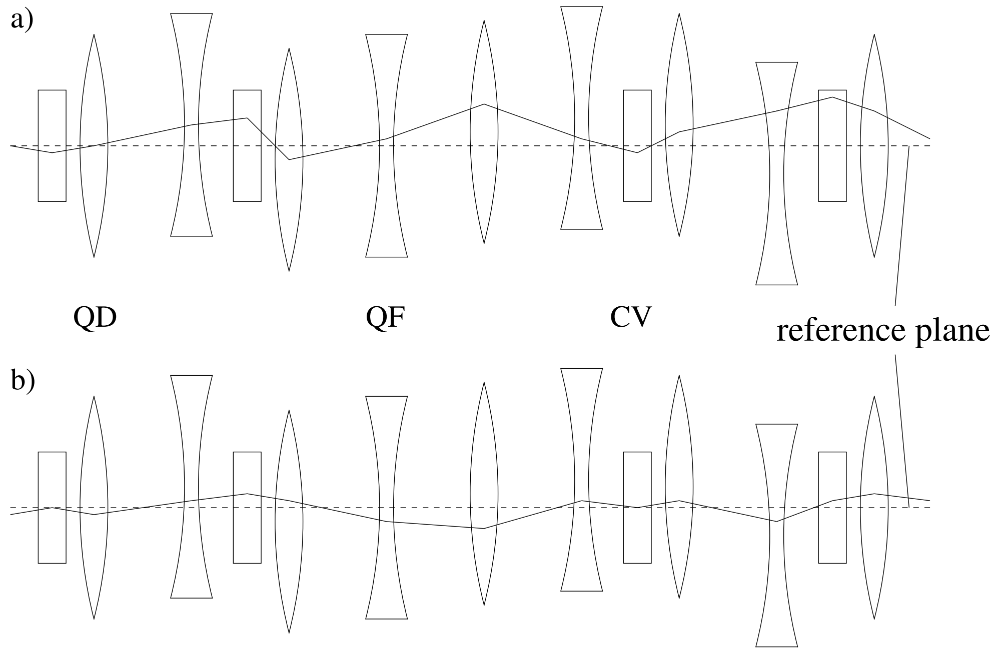

Figure 3.19: Effects of quadrupole misalignment. QF corresponds to the vertical defocusing quadrupole and QD to the vertical focusing quadrupole. The description QD and QF is given by the focusing effect of the quadrupoles in the horizontal plane (see Section 3.1). CV is a vertical corrector magnet. Using the correctors to adjust the beam towards the magnetic centre of misaligned quadrupoles induces vertical kicks (top) which can be reduced if the misalignment is used to correct the beam towards the reference plane (bottom). The diagrams also show the fact that only two out of three standard arc cells at LEP are equipped with a vertical corrector dipole magnet.

Chapter 4

Deterministic Harmonic Spin Matching

Deterministic HSM is used to reduce the time required to increase the polarization level, whenever this is possible. For beam energies around 45 GeV, this method was established very successfully by Assmann [21]. To improve deterministic HSM compared to empirical HSM a precise Fourier analysis of the integer resonances is essential as explained in Section 3.3.3. The error of the vertical BPM readings is the only uncertainty in the harmonic calculation (see Eq. 3.7).

4.1 Fourier Analysis

LEP has 500 beam position monitors. They are positioned at every vertically focusing quadrupole in the arc and at nearly every quadrupole in the dispersion suppressors and straight sections. The technical aspects are described in [40, 41]. The bending angle $\Delta\theta$ between two of the 240 BPMs in the arcs is 22.61 mrad. This limits the highest measurable Fourier component in the spin precession frame to $\nu = 138.8$. In the dispersion suppressor the local bending angle at a BPM changes from 0.75 mrad to 22.61 mrad. The different local bending at the BPM is taken into account in Eq. 3.7. Whereas FTAPO calculates the harmonic content only with BPM readings as sampling points, ORBIT is only available for simulations where the beam position is known everywhere (see Section 3.8). The effect of the irregular sampling is deduced by the comparison of the results of both programs.

Available BPMs

The Fourier components depend on the number of working BPMs. As a reconstruction of the orbit position at a faulty BPM is not precise, the missing reading is set to 0.0. For 15 faulty BPMs in the arcs and a vertical orbit r.m.s. of 250 μm, a statistical estimate leads to a Fourier component error of 3.5 μm. This value is deduced by Eq. 3.7. The average contribution of a missing BPM in the arc to the harmonics is obtained from the vertical position r.m.s. σ_y, the average local bending angle $\Delta\theta$ and the average of the square of the cosine/sine functions (0.5)

$$\sigma_{a_j/b_j} = \sigma_y \cdot \frac{\Delta\theta}{\pi} \cdot 0.5 \Rightarrow 0.9\mu\mathrm{m} \tag{4.1}$$

when $\sigma_y = 250\,\mu$m. This means the largest influence of a single BPM on the harmonic content is $\pm$ 1.8 μm. If several BPMs are unavailable their contributions add up quadratically, i.e. for 15 BPMs one finds $\sigma_{a_j/b_j} = 0.9 \cdot \sqrt{15} = 3.5\,\mu$m.

Fig. 4.1 shows the probability that a given BPM was not returning a useful reading in an orbit acquisition. 16 BPMs in the arcs or dispersion suppressors were failing for a significant amount of time. The harmonic contents of orbit acquisitions taken during polarization measurements in 1997 are presented in the Appendix B. In order to compare the different polarization fills, the Fourier

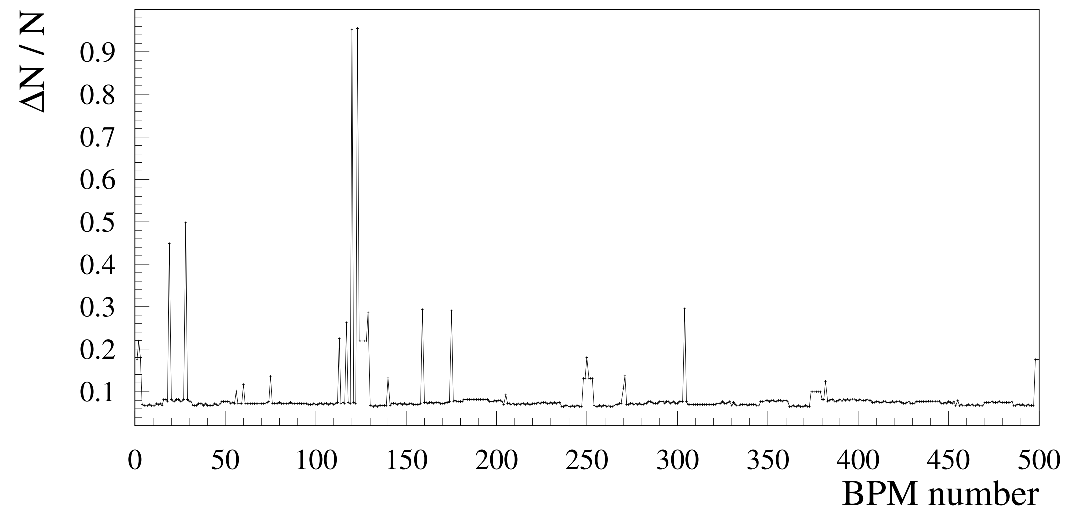

Figure 4.1: Probability for each BPM to return a useless reading for an orbit acquisition. The average level of 7% was due to network problems but occurred for certain orbits. Usually acquiring a second orbit just after the failed one returns normal signals. Most of the BPMs were only partially missing during polarization experiments.

component uncertainty due to the missing vertical readings has to be studied. The contribution of a single beam position monitor changes with the harmonic number k since $a_k \propto \cos(k \cdot \theta)$; $b_k \propto \sin(k \cdot \theta)$. The periodicity is illustrated in Fig. 4.2 for one BPM.

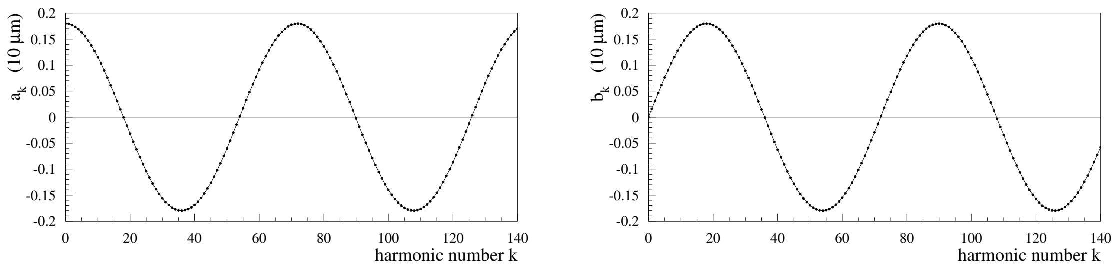

Figure 4.2: Contributions to the harmonic components of a single vertical BPM in the arc assuming a missing reading of $\sigma_y = 250\,\mu$m.

Fig. 4.3 gives the estimated average effect of the 16 BPMs as a function of the spin tune. The single BPM contributions are added quadratically. The maximum error is 3.6 μm whereas the average is 2.4 μm which is smaller than the statistical estimate. This is as expected since some of the BPMs are located in the dispersion suppressors where the local bending $\Delta\theta$ is smaller. Therefore they contribute less. In addition, the missing readings of unavailable BPMs can cancel their contribution due to the phase advance between them.

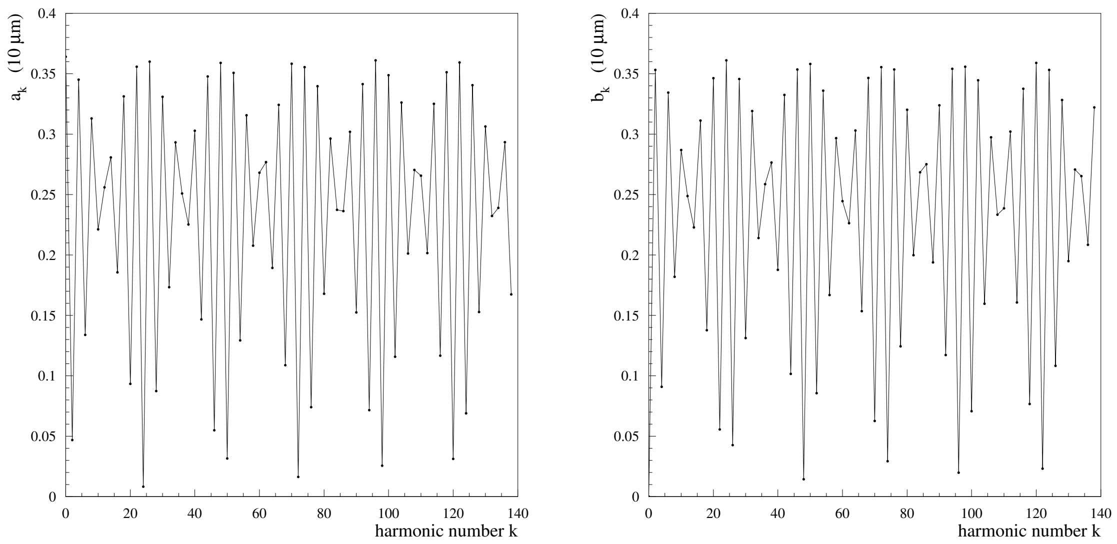

Figure 4.3: Average estimated influence on the harmonic content of the 16 BPMs which did not always work properly during the 1997 LEP run.

Figure 4.4: Screen shot of the program FOURIER. The Fourier components around the spin tune 101.5 of LEP fill 4405 are shown versus time. Time is given in hours since the start of the program. Changes of up to 15 μm are visible which are due to changes in the orbits made by the operators as well as orbit drifts.

If the assumption that a missing vertical reading corresponds to 250 μm is not used, an example at 44.7 GeV of an orbit acquisition shows the large variation of the Fourier components when the readings of the 16 BPMs are set to zero (see Table 4.1). The differences in the Fourier components are up to 15 μm compared to the simulated 3.5 μm for the statistical case. The difference is explainable by larger beam displacements at the missing BPMs. The impact of missing BPM readings led to the development of the FOURIER program which allows the continuous observation of the orbit harmonics versus time (see Fig. 4.4). The example shows the time variation of the components at 44.7 GeV during three hours of stable colliding beams in units of 10 μm. Changes up to 15 μm are visible. This large time distribution shows the importance of observing the harmonics in order to readjust the amplitudes of the HSM bumps and to provide stable conditions for a polarization build up. The program was written and tested at the end of the 1997 LEP run and will be used for future energy calibration measurements. The harmonic contribution of a single BPM for a given orbit can be studied. In addition, orbit data can be reloaded and compared with the online acquisition. This gives the opportunity to use the information of an old successful HSM compensation. The BPM set used for the evaluation of the harmonics can be modified to recalculate the required HSM bump amplitudes with respect to the available BPM readings.

Fourier components [10 μm]				
N_{PU}	a_{113}	b_{113}	a_{114}	b_{114}
All BPMs	3.57	-4.69	-0.92	-1.51
16 BPMs wrong	4.96	-3.59	-1.53	-1.56

Table 4.1: Fourier components of an orbit acquisition at 50.0 GeV with and without 16 BPMs which were not always available during the 1997 LEP run. The example is taken from LEP fill 4242, 03-10-1997, 00:23:31.

4.2 Alignment of Quadrupole Magnets

Motivated by simulations (see Fig. 3.18) an attempt was made to use the quadrupole alignment data. The difference in vertical position of the quadrupole magnets and their tilts are measured every year during the shutdown. Quadrupole positions which differ by more than 350 μm with respect to the average are readjusted just before the next startup. The cut in the distribution of the vertical differences leads to a width of 150 μm, which is similar to what was used for the simulations. The data of the years 1992 to 1996 is shown in Fig. 4.5. To analyse time dependence of the movements the data sets are compared to the latest data from 1996. The typical r.m.s. of the movement from one year to the next is about 50 μm.

The measurement procedure uses the two reference points on each quadrupole. It is sketched in Fig. 4.6. The differences between the first vertical position of the reference points of quadrupole j to the second reference on the same magnet and to the two points of the consecutive quadrupole $j+1$ are determined first. It is followed by a difference measurement of reference point number 2 on quadrupole j to the 2 references on magnet $j+1$ and to the first reference point of quadrupole j. This principle is then repeated for the quadrupoles $j+1$ and $j+2$, etc., for about 20–25 magnets. The measurement sequence is then repeated in the opposite direction. If the second measurement between two reference points differs by more than 80–120 μm, a third determination is made. The distribution of the variations for the difference measurements of two reference points has an r.m.s.

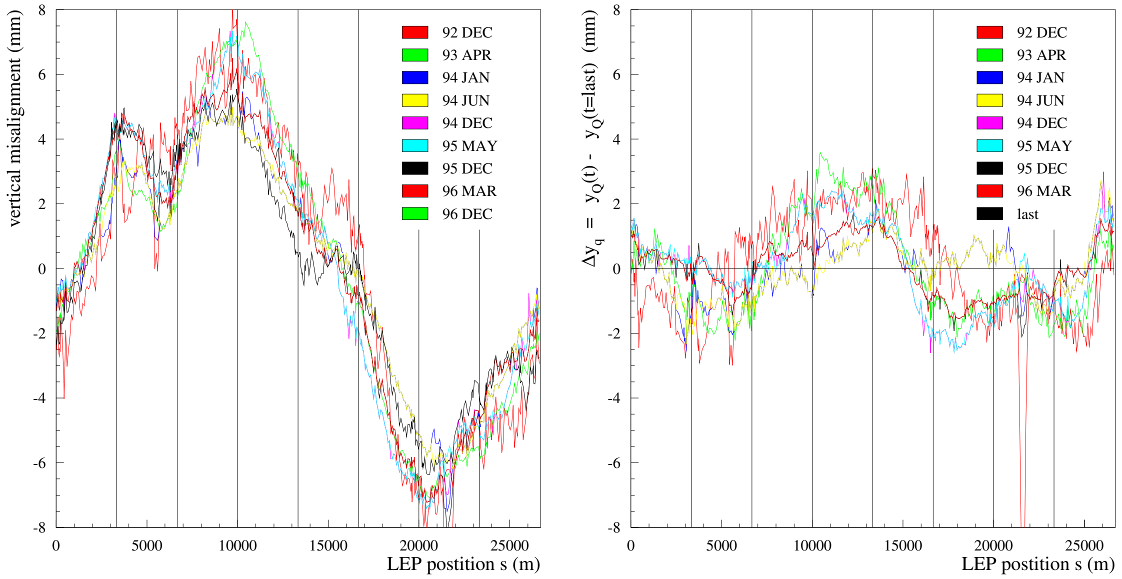

Figure 4.5: Vertical alignment of quadrupoles from 1992 to 1996: absolute position [mm] versus the longitudinal coordinate s [m] (left); movement of the vertical position with respect to the last measurement of 1996 (right). The vertical lines show the interaction points.

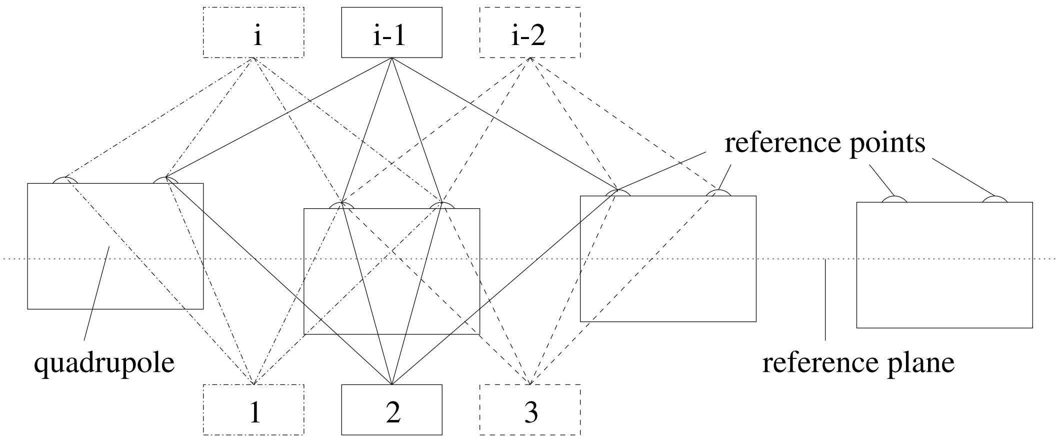

Figure 4.6: Measurement principle of the vertical quadrupole displacement compared to the LEP reference plane. The diagram illustrates that the vertical difference of two neighbouring quadrupoles is measured twice. The numbers $1, 2, 3, \dots i-2, i-1, i$ indicate the position number of the measurement instrument.

width of $\sigma_{\Delta y} = 40\,\mu$m. This indicates the "short length" quality of the procedure, but it does not exclude long range systematic effects. After having returned to the initial quadrupole, the magnet tilts are calculated with the measurements of the difference in vertical position of the two reference points on the same quadrupole. The vertical quadrupole positions are determined by the differences between the reference points of two consecutive magnets. The non-closure over the whole ring (840 quadrupoles) of the measurement procedure is defined as the different position of the quadrupole where the measurement sequence has started and ended. Over the last years it has been about 0.8 mm [42]. The position of quadrupoles that are realigned are remeasured with respect to the neighbouring 20–25 quadrupoles. Realignments are made as late as possible, so as to avoid accidental displacements during work in the tunnel that would remain undetected until the next year.

At the end of 1997 the alignment measurement was made again after the end of the LEP run. In order to study the alignment data from one quadrupole to the next, the lowest harmonics are taken out. The original data set h0 has peak to peak position differences of 12 mm. Removing the first harmonics one after the other one obtains the different sets hi where i corresponds to the highest harmonic which is taken out. The reduction of the r.m.s. is listed in Table 4.2. In addition, the data can be smoothed by subtracting the average positions of $j/2$ preceding and $j/2$ following quadrupoles which leads to the data sets with the ending pj. The peak value in the h2p30 set is reduced within to 1 mm. Fig. 4.7 shows the results of fits and of smoothing

	h0	h1	h2	h4	h2p70	h4p70	h2p30
R.m.s. [μm]	3436	824	426	494	183	242	183

Table 4.2: R.m.s. misalignment for the raw alignment data h0 and after removal of harmonics i in the described order. pj refers to the number of quadrupoles used to define the average position which is subtracted from each position.

on the alignment data. Removing the first harmonic reduces the r.m.s. from $\sigma_{h0} = 3436\,\mu$m to $\sigma_{h1} = 826\,\mu$m. The non-closure of the h0 data is also removed in this step. Then, the fourth is removed, $\sigma_{h4} = 494\,\mu$m. Finally, the second harmonic is fitted to remove the r.m.s. down to $\sigma_{h2} = 426\,\mu$m. The last procedure is applied to smooth the data. As seen in Fig. 4.7, the main effect is coming from the first two steps. A large reduction of r.m.s. is possible if the average vertical position before and after each quadrupole is subtracted. Using, for example, an average over 70 magnets yields an r.m.s. of $\sigma_{h2p70} = 242\,\mu$m. The three parameter fit to remove the i^{th} harmonic is given by

$$y_i = a + b \sin\left(\frac{2\pi}{C} i \cdot y_{i-1} + c\right). \tag{4.2}$$

The data sets h0 of 1997 are shown in Fig. 4.8. Both data sets are in agreement with the previous years (see Fig. 4.5). The first visible sine harmonic is explained by an angle between the measurement plane and the LEP reference plane. When this harmonic is removed one obtains the h1 data sets shown in Fig. 4.9. The peak to peak value is reduced from 14 mm to 7 mm. Both alignment files show a fourth harmonic in the vertical positions. This is due to the fact that each interaction point depth was measured from the surface. The fourth harmonic represents the LEP symmetry and can also be removed. The resulting data sets (Fig. 4.10) have only a peak to peak difference of 4 mm for which the movement over six months (1997 LEP running period) can be studied in more detail.

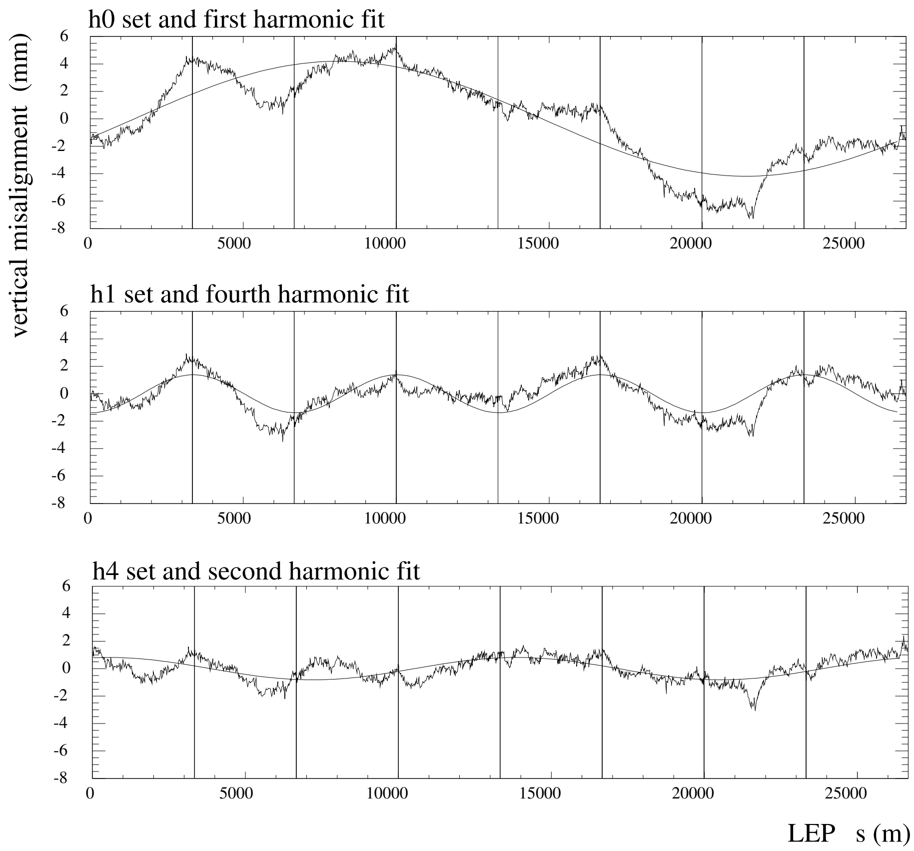

Figure 4.7: Diminishing the peak to peak value of the alignment data: the alignment data set is plotted together with the fitted harmonic component which is removed.

In order to estimate whether the differences between the last two data sets are real or a statistical fluctuation, one has to simulate the error of the measurement procedure. The statistical error of the vertical position differences is $\sigma_{\Delta y} = 40\,\mu$m. It is given by the r.m.s. of the distribution which corresponds to the difference of the measurements between two neighbouring quadrupoles. Since each position between two quadrupoles is measured twice, the error on the difference between two quadrupoles is in principle only $\sigma_{\Delta y_Q} = \sigma_{\Delta y}/\sqrt{2} = 28\,\mu$m. This error adds up randomly over one turn. These *random walks* have been simulated for several seeds and are presented in Fig. 4.11. The envelope grows with the number n of magnets times the statistical error for the difference between two magnets $\sigma_{\Delta y_Q}$.

As the measurement sequence must be close, i.e. the position of the quadrupole should be the same after one full turn, the statistical uncertainty is reduced by a factor of $\sqrt{2}$ to $\sigma_{STAT} = 420\,\mu$m. Fig. 4.12 shows the difference of the last two alignment sets together with the non-closure of $\pm\,0.8$ mm given by the alignment section and the statistical uncertainty range of $\pm\,0.42$ mm. As the fraction of the difference data outside the statistical sigma is about one half of the whole data sample, the movement of the vertical quadrupole position cannot be explained by a statistical fluctuation and has to be considered as real provided that there is no additional systematic measurement error.

After having taken out the first harmonic in the alignment data the residual data file has a vertical peak to peak value of about 4.5 mm. Trying to correct the beam to this reference would be dangerous and is not possible with the correctors installed in LEP (number and strength). The

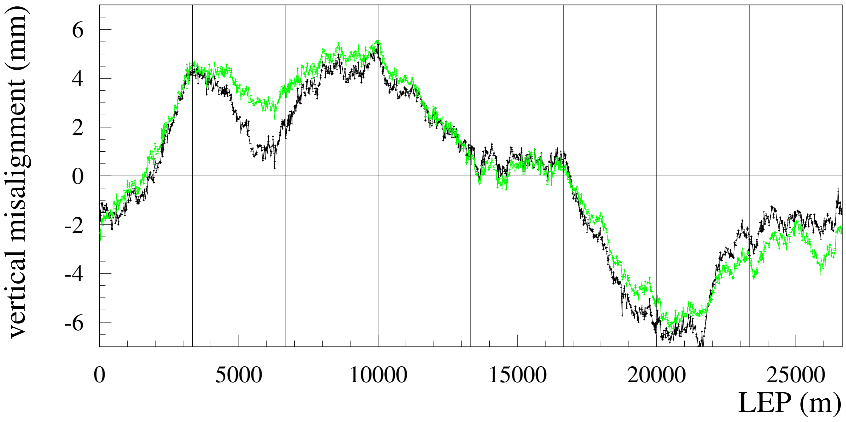

Figure 4.8: Comparison of the original alignment data before and after the 1997 LEP run (h0 sets). The grey set is the measurement before the run, the black one after the run.

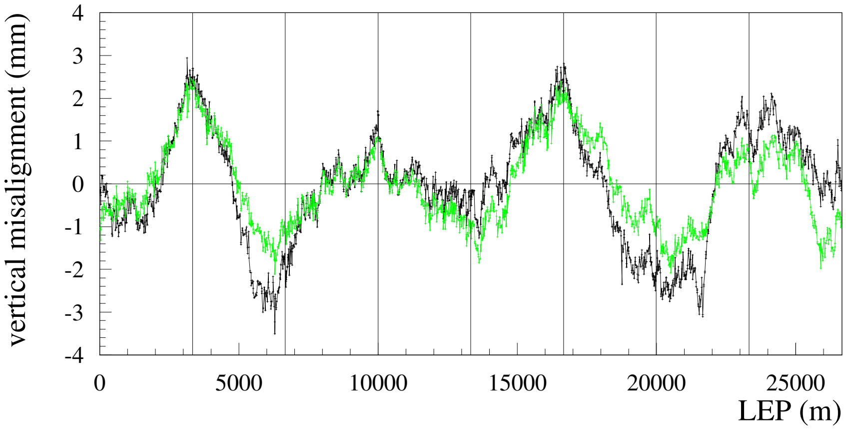

Figure 4.9: Comparison of alignment data before and after the 1997 LEP run after removing the first harmonic (h1 sets). The grey set is the measurement before the run, the black one after the run.

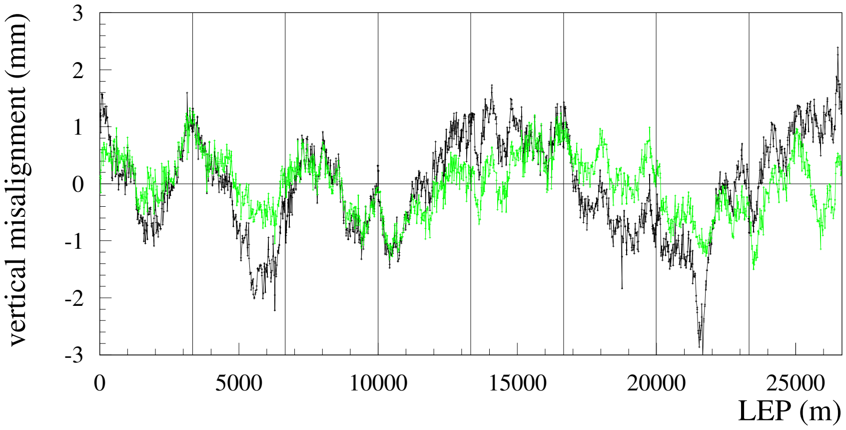

Figure 4.10: Comparison of alignment before and after the 1997 LEP run after removing the first and the fourth harmonic (h4 sets). The grey set is the measurement before the run, the black one after the run.

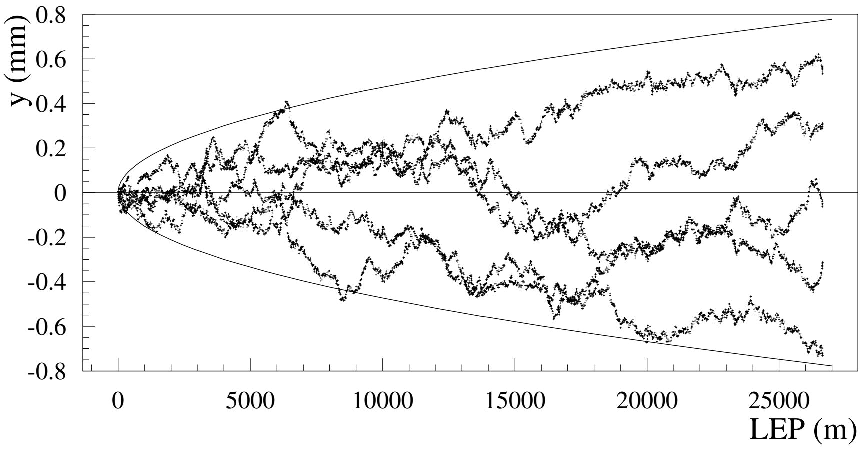

Figure 4.11: Simulation of systematic vertical position errors due to different random walks along the ring. The envelope is given by $\pm\sqrt{n} \cdot \sigma_{\Delta y_Q}$ where n is the number of magnets counted from the starting point.

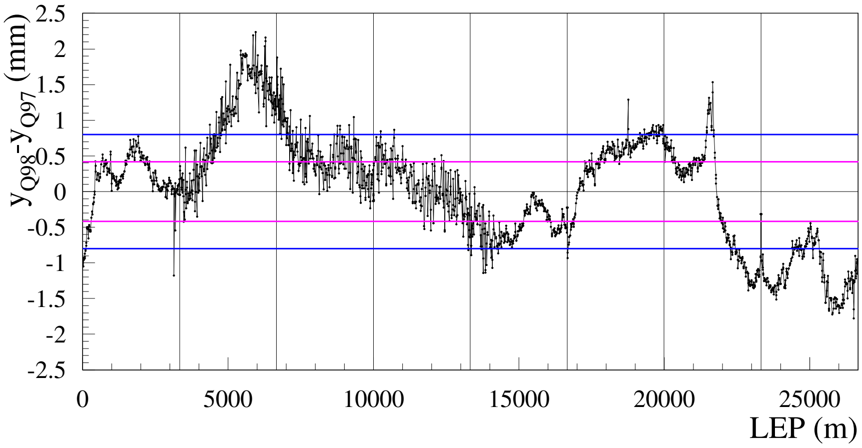

Figure 4.12: Difference between the alignment data before and after the 1997 LEP run. The plot includes the statistical uncertainty sigma at $\pm$ 0.42 mm and the non-closure of the alignment sets at $\pm$ 0.8 mm.

peak to peak value can be diminished by taking out higher components or smoothing the data as described before. A Fourier analysis indicates that high frequency components which correspond to the polarization energies do not change very much in the different alignment files (see Appendix B, Table B.4) since the low frequencies do not affect the higher ones. Only the h0 set has Fourier components which are significantly different from the others and reduces the calculated polarization value by 24% (see Section 3.8.2).

As a conclusion it should be sufficient to correct the beam to a smoothed data file which has a significantly reduced orbit size. As mentioned, only two of three vertical focusing quadrupoles are equipped with vertical correctors. With the existing correctors and orbit correction software [43, 44] it was impossible to steer the beam according to the orbit given by the alignment data in 1997.

The Harmonic contents of the alignment data sets are summarised in Appendix B (see Table B.4). The important components do not differ by more than about 10% or about $\pm$ 3 μm, which is less than the uncertainty due to missing BPMs. Fig. 4.13 gives the Harmonic content of the alignment data versus the spin tune.

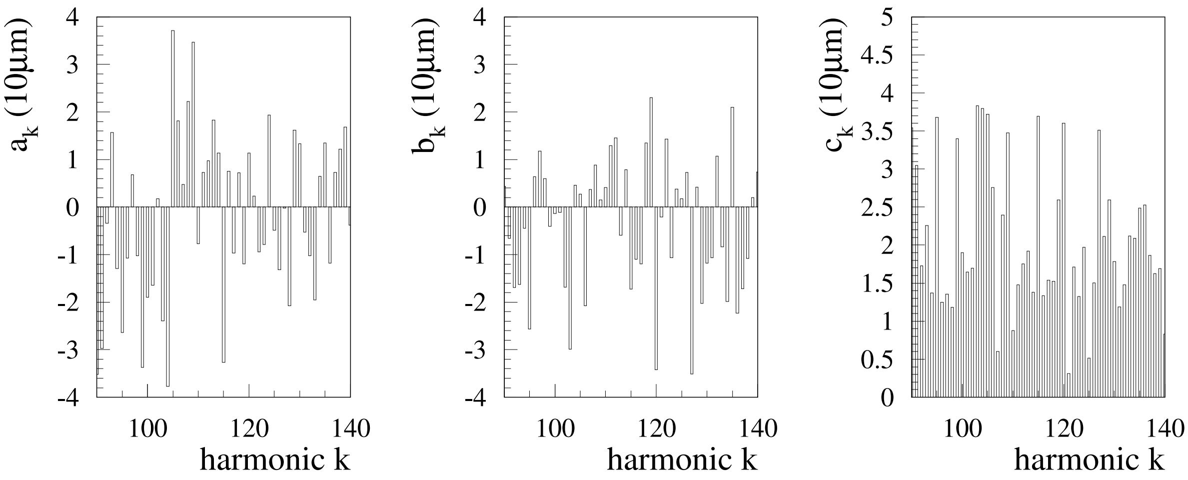

Figure 4.13: Harmonic spectrum of the LEP alignment data. Left: a_k; middle: b_k; right: c_k. The vertical scale is in units of $10\,\mu$m.

The largest harmonic components have amplitudes of about $30\,\mu$m in the spin tune range corresponding to beam energies between 40 and 60 GeV.

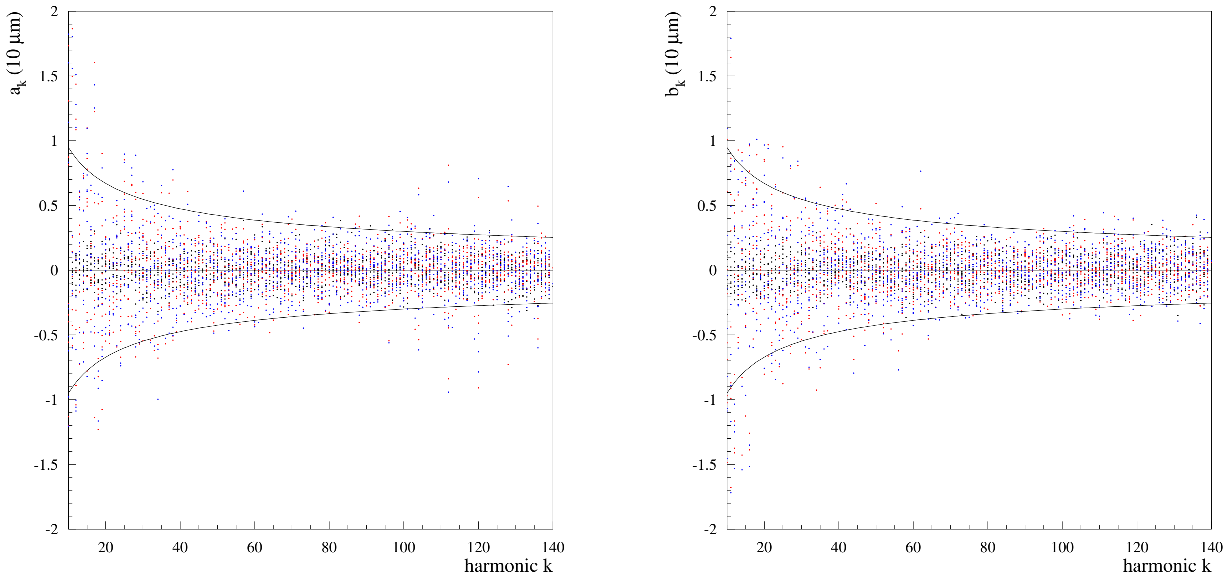

Figure 4.14: The Fourier components (cosine a_k, sine b_k) of the statistical errors of the alignment data. The contribution of the statistical error is smaller at higher frequencies.

The harmonic contribution of the statistical error of the alignment measurements can be seen in Fig. 4.14. The values are derived by analysing the components of different random walks which represent the statistical error.

The contribution of the statistical errors in the range of the polarization energies is in the order of $4\,\mu$m and corresponds to about 1/7 of the alignment harmonics. The statistical uncertainty as a function of the frequency is explained by the number of quadrupoles between two sampling points for a particular frequency. The statistical error grows with the square-root of the number of measured quadrupoles. The highest frequencies $\nu \approx 140$ have a periodicity of two cells (4 quadrupoles) compared to 840 quadrupoles for the lowest frequency.

The large difference between the harmonic contribution of the alignment data and its statistical uncertainty proves that the alignment measurements can add useful information to improve deterministic HSM.

Fig. 4.13 and 4.14 also indicate the best choice of spin tunes and energies which can provide the highest polarization. Due to the straight sections which have no bending magnets LEP has a symmetry of 4 and 8. The sampling points for the Fourier analysis in the spin precession frame (the bending area) are not continuous. The sampling is divided into eight parts with an arbitrary connection in the spin precession frame. This LEP symmetry induces very strong integer resonances every 4 and 8 integers [14].

The largest components represent unfavourable energies for energy calibration as they are depolarizing integer resonances which excite synchrotron sidebands and linear resonances. The spin tunes for energy calibration between 40 and 61 GeV were selected according to this rule. Their neighbouring integer resonances are less strong. This reduces the compensation problems of deterministic HSM. The selected spin tunes are given in Table 4.3.

Spin tune	93.5	101.5	103.5	113.5	125.5	137.5
Energy [GeV]	41.2	44.7	45.6	50.0	55.3	60.6

Table 4.3: Favourable spin tunes and corresponding energy for energy calibration by resonant depolarization.

4.3 Determination of Beam Position Monitor Offsets

Offsets of the beam position monitors relative to the centre of the quadrupoles are important errors for the HSM procedure (see Fig. 3.7). With BPM offsets that are too large, deterministic HSM does not work reliably. For this reason a technique called *k-modulation* for measuring these offsets with the beam itself has been developed since 1993. Initial tests were performed in 1993 and 1994 on the super-conducting QS0 quadrupoles next to the experiments whose power converters could be ramped to execute small current steps around their nominal currents. This led to the discovery of large ($\sim$2 mm) BPM offsets next to these quadrupoles [30, 45]. In 1997, all quadrupoles with an adjacent BPM were equipped with special windings to measure the offsets by k-modulation [39].

4.3.1 Principle

The quadrupole strength k is proportional to the field gradient and defined as

$$k = \frac{e}{p}\frac{dB_x}{dy}, \tag{4.3}$$

which means the magnetic field of a quadrupole B_x linearly depends on the beam position in the magnet. A particle passing at a distance y_Q from the centre of the quadrupole receives a deflection y'

$$y' = k \cdot L \cdot y_Q \tag{4.4}$$

where L is the length of the quadrupole. When the beam position y_Q is fixed, a change of the quadrupole strength Δk leads to a change of the deflection

$$\Delta y' = \Delta k \cdot L \cdot y_Q. \tag{4.5}$$

This deflection changes the closed orbit in the whole ring. If a quadrupole field strength k is modulated with a constant amplitude Δk_0 and frequency f_k the residual orbit variation is detectable at any position around the ring where the phase is adequate. The beam position $\Delta y(s,t)$ then oscillates at the frequency f_k. In other words

$$\Delta y_0(s, y_Q) \;\propto\; \frac{\Delta k_0 \cdot L \cdot y_Q}{2\sin(\pi Q_y)}\sqrt{\beta_Q \beta(s)} \tag{4.6}$$

$$\Delta y(s,t,y_Q) \;=\; \Delta y_0(s,y_Q)\cos(2\pi f_k t + \psi) \tag{4.7}$$

where β_Q and $\beta(s)$ are the beta functions in the modulated quadrupole and at the longitudinal position s, and Q_y is the betatron tune (see Eq. 2.12). The oscillation amplitude Δy_0 depends on the beam position y_Q in the modulated quadrupole which can be changed with local orbit bumps. The amplitude Δy_0 reaches its minimum ($\Delta y_0^{min} \approx 0\,\mu$m) when the beam is centred in the quadrupole ($y_Q = 0\,\mu$m). The adjacent BPM reading at the modulated quadrupole $y_{BPM} = y_{\mathit{off}}$ gives the BPM offset with respect to the quadrupole.

A relative change in the quadrupole strength of $\Delta k_0/k \leq 10^{-3}$ is sufficient to detect the oscillations with the required accuracy. The modulation frequency f_k is in the range of 0.7 to 3.3 Hz to avoid exciting dangerous orbit oscillations. The oscillation $\Delta y(t)$ is detected with two very precise beam position monitors (couplers) left and right of IP1 with a betatron phase advance of $(2n+1)\pi/2$ to guarantee that the orbit oscillation can be seen by at least one of the couplers. In order to modulate several quadrupoles at the same time, a windowing harmonic analysis is used to record the orbit oscillations. The windowing allows a minimum modulation frequency separation of 0.1–0.15 Hz. The beam position in the quadrupole is varied over five positions with orbit bumps. The measurements are fitted with the three parameter function

$$\Delta y = f(y_Q) = a + b \cdot \mid y_{BPM} - y_{\mathit{off}} \mid . \tag{4.8}$$

y_{off} is the BPM offset, b refers to the *slope* of the oscillation amplitude $\Delta y(t)$ depending on the beam position y_Q in the modulated quadrupole, whereas a allows a non-zero oscillation amplitude due to noise when the beam is centred. Fig. 4.15 illustrates the k-modulation principle. A hardware description of the couplers, software of the oscillation detection and analysis of the data in the straight sections can be found in [30, 31].

Before 1997 only the quadrupole magnets with a BPM in the straight sections and in the arc of IP8 were equipped with k-modulation windings able to change k. Motivated by the impacts of the BPM offsets on the achievable polarization level [39] every quadrupole with a BPM in the arcs and dispersion suppressors was provided with additional (so called *back leg*) windings which can be powered separately (see Fig. 4.16).

The whole installation (quadrupole selection, power supply settings such as modulation frequency and amplitude, data acquisition, etc.) is driven from the LEP control room.

16 quadrupoles (one per half octant) can be powered independently and simultaneously with different frequencies limited by the available quadrupole power supplies. The number of quadrupoles and beam position monitors at various locations at LEP is given in Table 4.4.

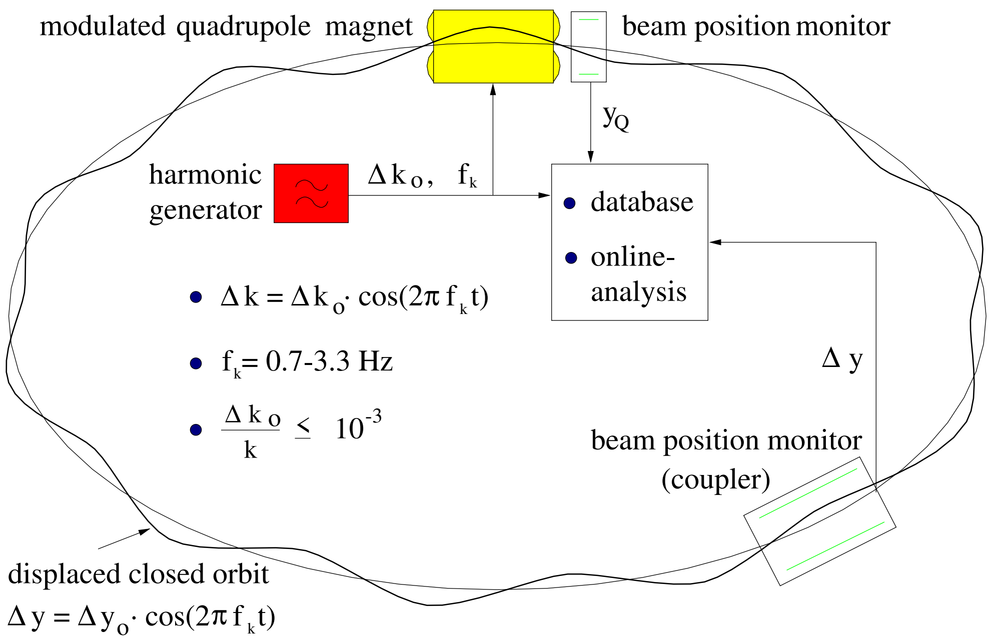

Figure 4.15: Principle of the k-modulation.

Location	Quad. name	Quad. amount	BPM name	BPM amount
Straight section	QS/QL	192	PU.QS/QL	148
Dispersion suppressors	QS/QL	128	PU.QS/QL	112
Arcs	QD	240	PU.QD	240
	QF	248		

Table 4.4: Number of beam position monitors and quadrupole magnets in LEP

4.3.2 Operation

The k-modulation in the arcs and dispersion suppressors is possible while the beams are in collision. Four independent measurements (two coupler readings for electrons and positrons) are available to determine the BPM offsets. The simultaneous calibration of 16 offsets takes 40 minutes. Four corrector bumps are used to steer the beam. The vertical dispersion created by each of these bumps is reduced by a second bump π away in phase. In addition, the phase advance between two modulated quadrupoles of the same octant is chosen to be a multiple of π. This leads to a luminosity reduction of up to 15% with the largest bump amplitude. Normally k-modulation is run only in the last part of the fills.

In the dispersion suppressors the irregular phase advance prevents the use of the dispersion compensation scheme. For this reason physics operation can be strongly perturbed, with luminosity reductions of up to 40%.

In the straight sections the bumps cannot be applied because of background problems in the experimental detectors. As the beams are separated in some quadrupoles they cannot be moved to the quadrupole centre.

A complete beam position monitor calibration consists of the following procedure: the quadrupoles which have to be modulated are selected on the operation console. According to this

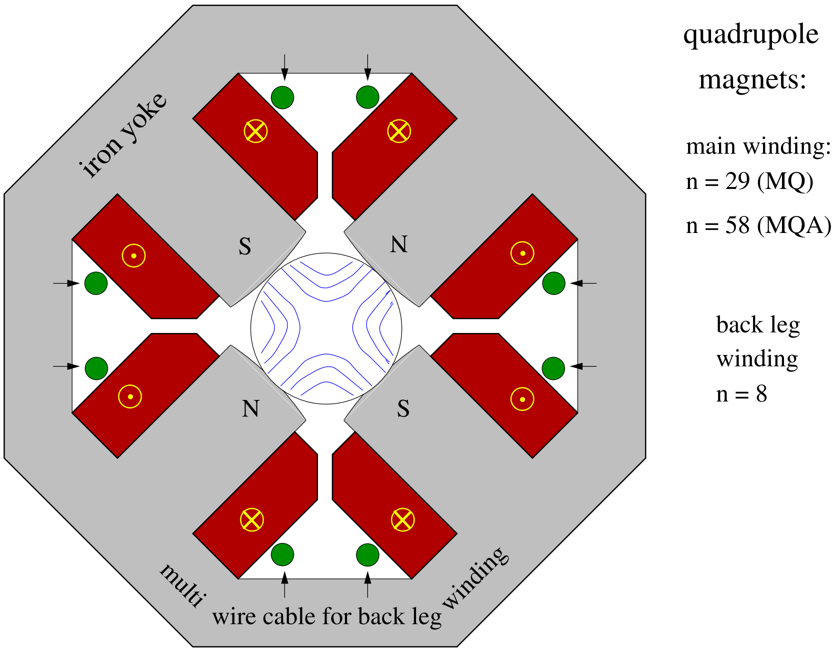

Figure 4.16: Cross-section of a quadrupole magnet with back leg winding.

selection, the harmonic generators are powered to modulate the quadrupoles with individual frequencies and amplitudes. A data acquisition program records the windowing harmonic analysis result of the coupler readings. The beam current is also taken into account to normalise the coupler signal. A second program records the beam position in the modulated quadrupole. The oscillation amplitudes and the BPM readings of each quadrupole are displayed online. New BPM data is provided every minute. A higher data taking frequency would affect the ability of the operators to acquire an orbit reading at any moment. The beam position in the modulated quadrupole is moved with the described local orbit bump to record eight data points at each beam position. Starting the data acquisition without a bump the amplitude is increased in steps of 0.5 mm to $\pm$ 1 mm.

The quality of the k-modulation data was checked for signal overlaps between neighbouring frequencies ($\Delta f_k \gtrsim 0.1$ Hz) as well as for cross-talk between quadrupoles by the induction of the powered back leg windings in the main coils. No significant systematic effect was observed.

The calibration analysis is possible during data taking. During the 1997 LEP run the data analysis was made afterwards in order to take into account fit problems like parameter start values. The fitted offsets were individually checked so as to avoid introducing poor data in the machine.

4.3.3 Measurement Results

An example of a vertical BPM offset calibration is shown in Fig. 4.17. All four measurements are in agreement and give good fits. The average leads to an offset of $-481 \pm 25\,\mu$m. The error is given by the weighted average of the single determinations depending on the fit quality of each measurement. The offsets could not be determined for all BPMs because of unfavourable phase advances between quadrupole and couplers. Some BPMs, like the example of Fig. 4.18, were unusable. This BPM has been known to have unstable and unphysical readings for a long time. In Fig. 4.18 one can see that the average offsets for electrons and positrons each are in agreement ($y_{e^-} = 1178 \pm 71\,\mu$m; $y_{e^+} = -430 \pm 73\,\mu$m) but differ by 1.6 mm, in fact they even change during

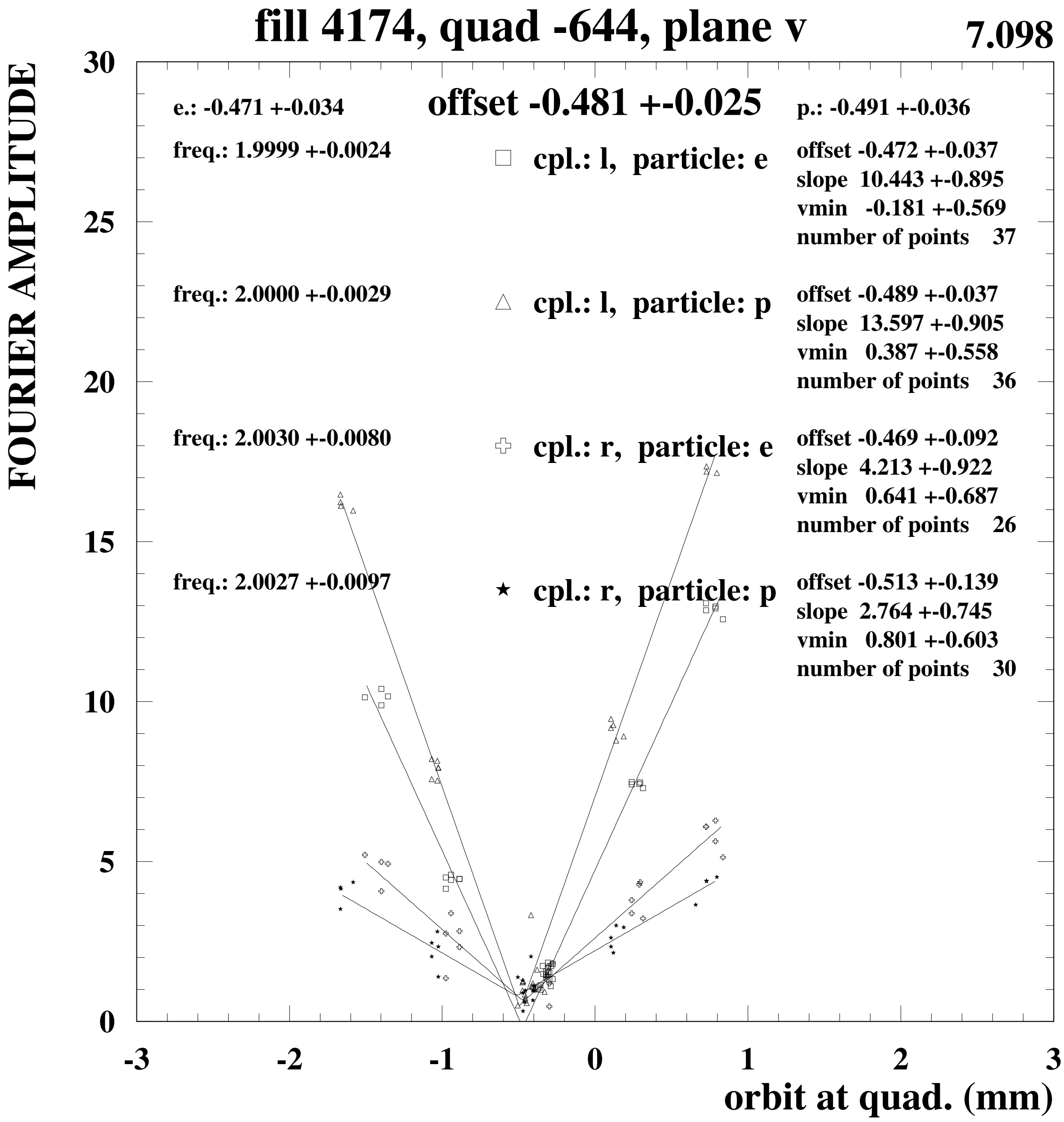

Figure 4.17: Example of the BPM calibration in LEP fill 4174 of BPM PU.QD44.L6. The oscillation amplitude Δy is plotted as a function of the beam position in the quadrupole y_Q. The offset is given by the minimum oscillation amplitude. The different marker types indicate the four measurements for electrons and positrons in both detectors. The data of each measurement is fitted according to Eq. 4.8. The number of data points, results and uncertainties for each fit are also listed in the plot. The BPM offset is derived from a weighted average of the four measurements, yielding an offset of $-481 \pm 25\,\mu$m. All measurements are consistent in this case.

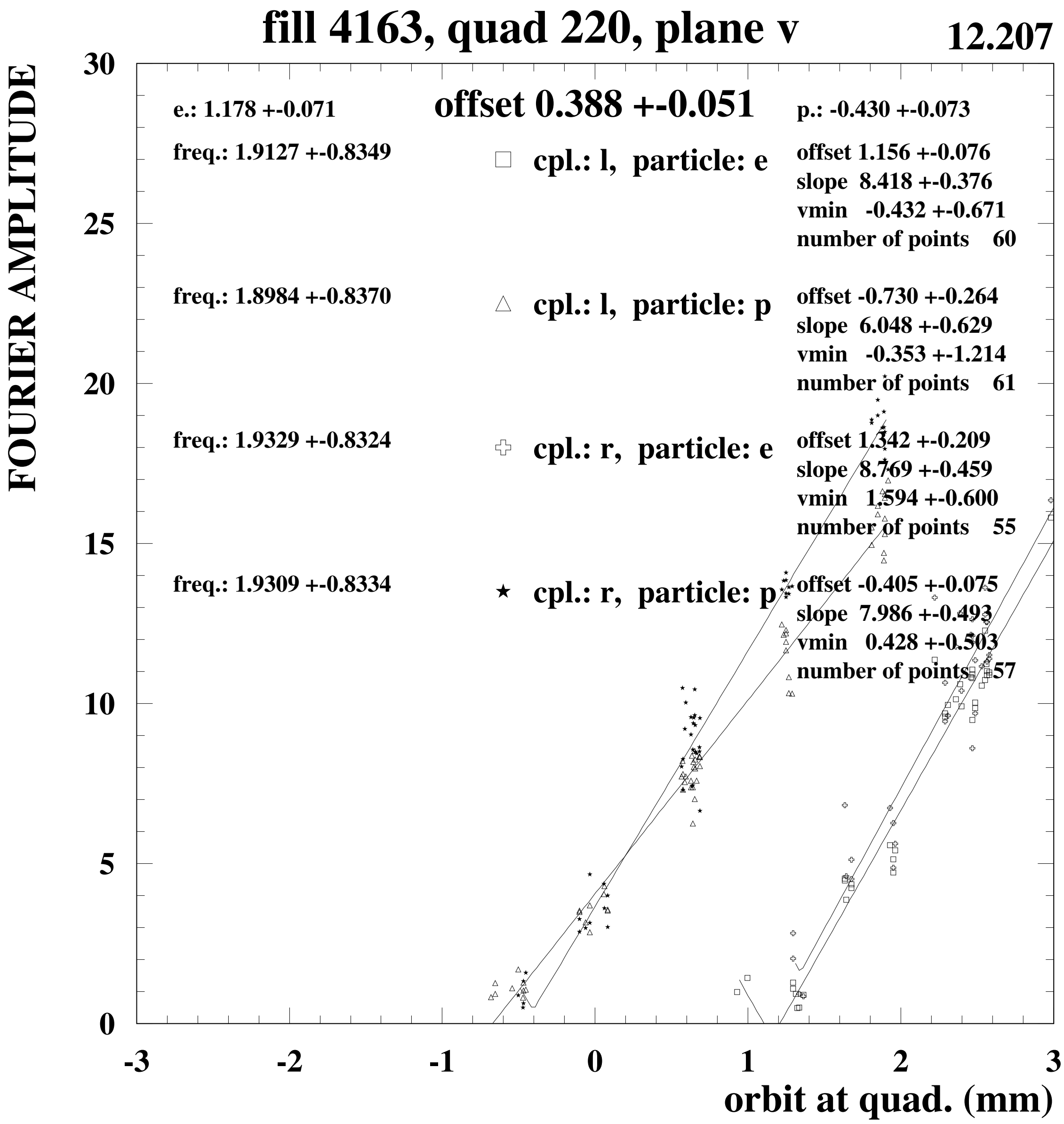

Figure 4.18: Example of an unsuccessful offset determination for PU.QD20.R2 in LEP fill 4163. The fits are consistent for each particle type but the mean value of electrons and positrons differ by 1.6 mm. Four attempts to calibrate the offset failed. In fact this BPM has been known to give fluctuating readings for many years. The origin of the problem is not yet understood. This BPM is one of the 16 BPMs with poor readings described in Section 4.1.

the same fill. As a consequence, the averaged offset cannot be used. Cuts have been introduced to enhance good measurements: the combined error of the four measurements should be less than 55 μm and the e^+ and e^- offsets should not differ by more than 100 μm. Offsets which have been measured more than once without a cut result had to be consistent.

More than 550 measurements of the vertical beam position monitor offsets have been made. 419 offsets have been determined and analysed in September 1997. After cuts, 313 non-zero offsets were used to correct the BPM readings for each orbit acquisition and could be used during polarization measurements. Unsuccessful offset determinations were repeated in the last two months of the 1997 LEP run. 31 monitors out of 353 in the bending area could not be calibrated due to bad BPM readings. This corresponds to 8.8% of the total.

Fig. 4.19 and 4.20 show the vertical offset distributions of electrons and positrons obtained by k-modulation. The mean values differ by 50 μm which indicates an electronic offset. The r.m.s. width $\sigma_{total} \approx 270\,\mu$m is almost as large as expected from earlier k-modulation results in the straight sections. The statistical error distribution of the averaged offsets is shown in Fig. 4.21. The mean error is 30 μm with an r.m.s. of 10 μm. This indicates the precision of the determined offsets by k-modulation.

According to the simulation results from Fig. 3.18 the reduction of the BPM offsets r.m.s. from 270 μm to 30 μm more than doubles the polarization obtained with deterministic HSM in the linear model. About 50 beam position monitors were calibrated several times to check the reproducibility of the procedure and gave consistent results. Table 4.5 summarises the k-modulation results for electrons and positrons. Fig. 4.22 shows all BPM offsets.

Some beam position monitors in the arcs of IP8 were measured in previous years. Surprisingly, some of the 1997 measurements resulted in offset changes of more than 100 μm. It cannot be distinguished if this time dependence is due to a change of the signal attenuation in the electronic equipment or due to a mechanical movement of the BPM relative to the quadrupole. For this reason, at least some of the offsets should be remeasured during the 1998 LEP run. In addition, the 31 faulty BPM offsets may eventually be determined. The calibration of the 148 BPMs in the straight sections is also advisable for machine optimisation. The measurements of 1997 do not indicate any time dependence but they were made on the time scale of a few months. The Fourier components of the BPM offsets are summarised in Appendix B (see Table B.4) and shown in Fig. 4.23. Assuming an average error of 30 μm the error of the harmonic contribution of the BPM offsets is 2.3 μm.

Particle	Mean offset [μm]	Offset r.m.s. [μm]	Mean error [μm]	Error r.m.s. [μm]
e^+	-43	273	40	13
e^-	-90	235	45	18
e^+/e^- average	-65	267	30	11

Table 4.5: Results of the k-modulation.

4.4 Summarising the Errors of the Fourier Analysis

Different sources of vertical position errors leading to an uncertainty in the Fourier analysis have been discussed in this chapter. Fig. 4.24 compares the strength c_k of the integer resonances k

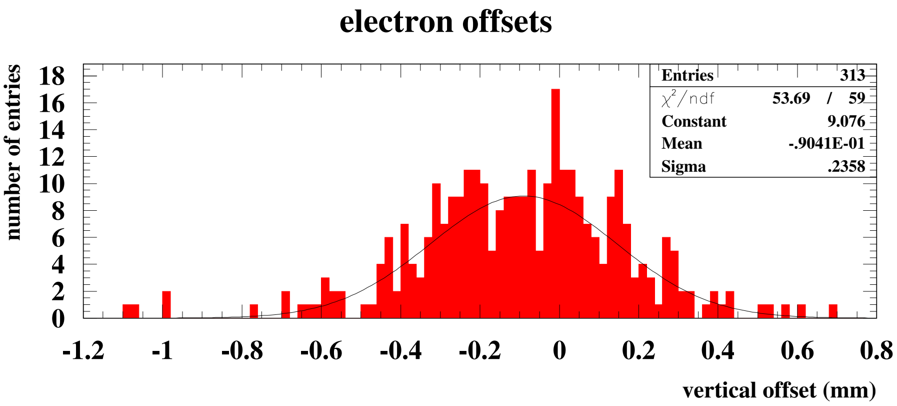

Figure 4.19: Distribution of BPM offsets for electrons.

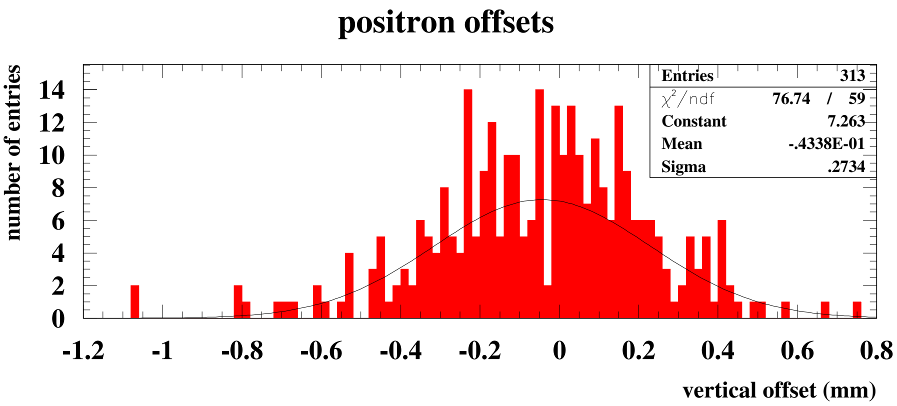

Figure 4.20: Distribution of BPM offsets for positrons.

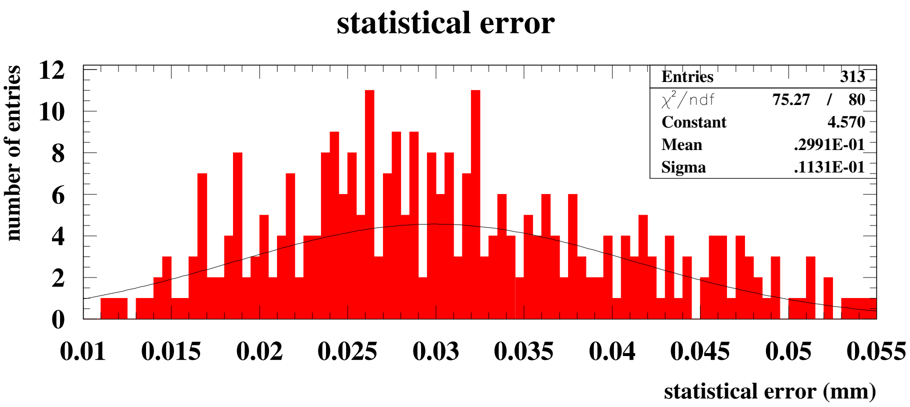

Figure 4.21: Combined statistical error of the BPM offsets measurements.

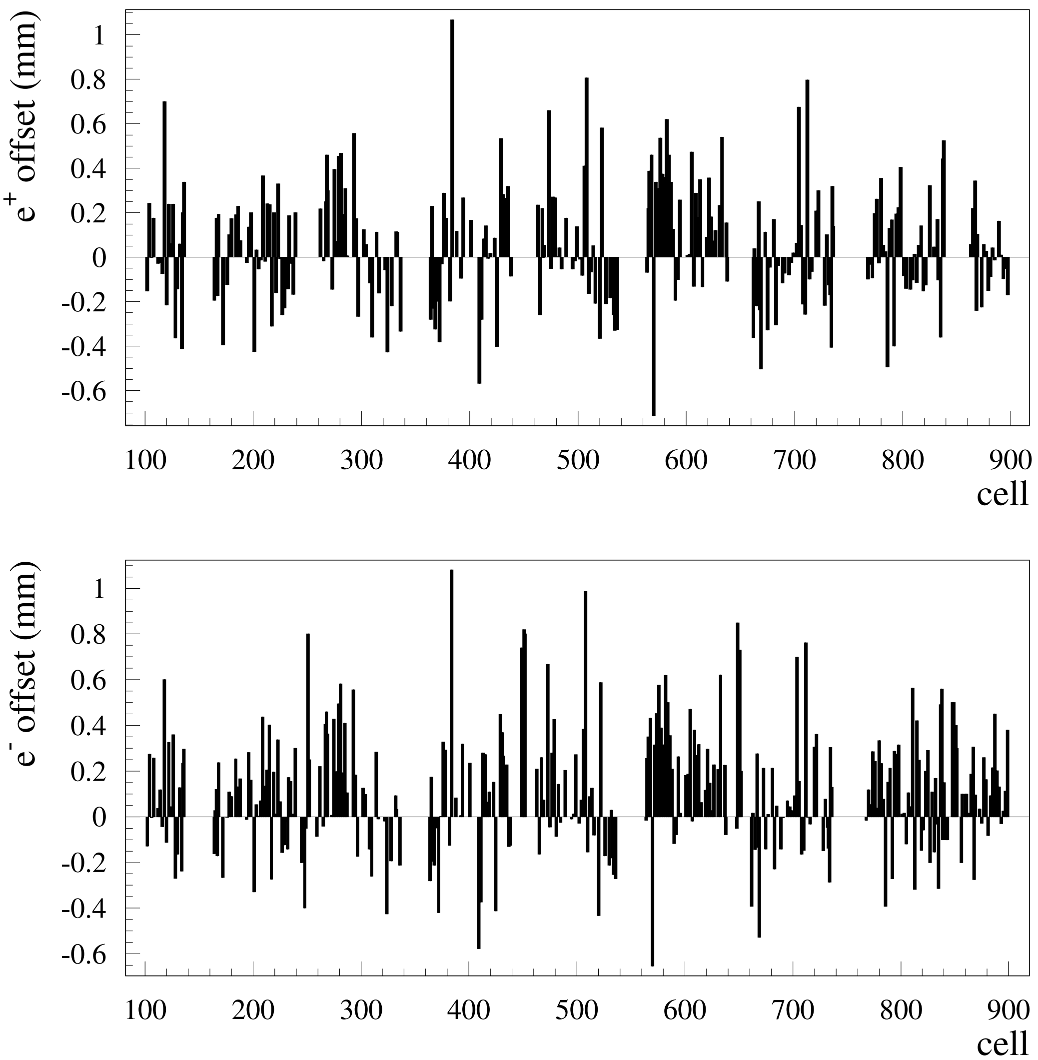

Figure 4.22: BPM offsets determined by k-modulation offsets for positrons (top) and electrons (bottom) as a function of the cell number.

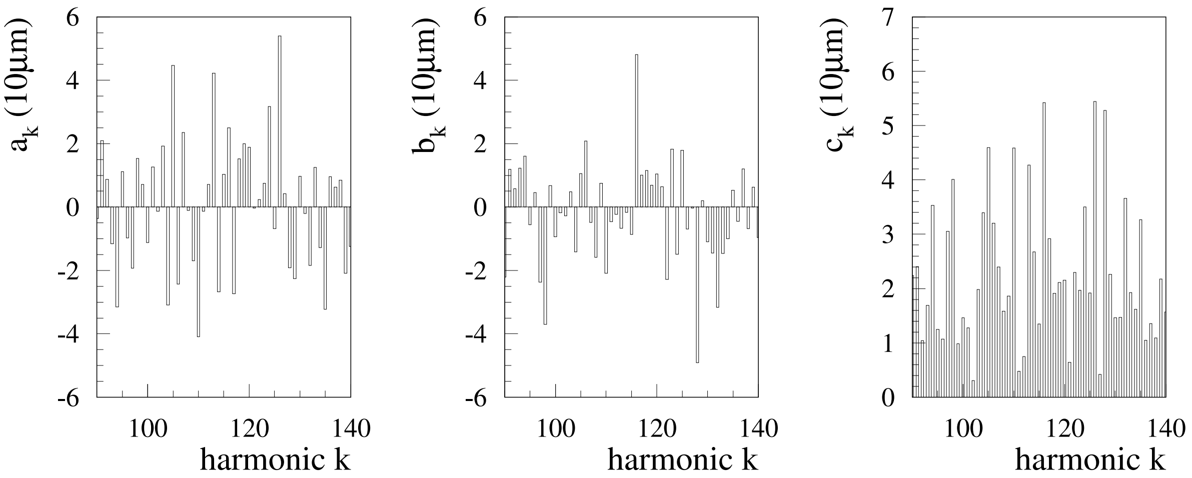

Figure 4.23: Fourier components of the BPM offsets determined with k-modulation. Left: a_k; middle: b_k; right: c_k. The vertical scale is in units of 10 μm.

of the alignment and the k-modulation data for the energy range of 40–60 GeV. On average the k-modulation harmonics are larger than the contribution from the quadrupole alignment. At the energy calibration points of 50.0 and 55.3 GeV the beam position monitor spectrum is high. The

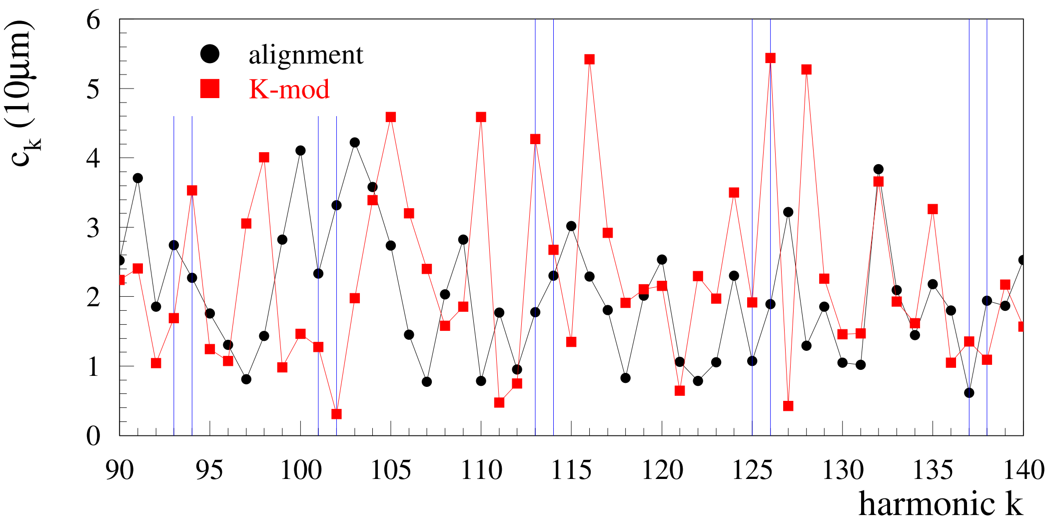

Figure 4.24: Comparison of the strength c_k of the integer resonance k of the alignment and the k-modulation data. The vertical lines indicate the integer resonances that are next to the selected spin tunes for energy calibration.

averaged strength from the k-modulation spectrum in this energy range is $\overline{c}_{kmod} = 21.9\,\mu$m which is 29% larger than the $\overline{c}_{align} = 15.5\,\mu$m from the alignment. As an example of this behaviour the four harmonic components at 50.0 GeV are compared in Table 4.6. The cosine component a_{113} of the k-modulation data is much bigger than any other contribution.

[10 μm]	a_{113}	b_{113}	a_{114}	b_{114}
k-modulation	4.22	-0.67	-2.67	-0.17
Alignment	0.79	-1.59	0.21	2.30

Table 4.6: The four Fourier components of the alignment and k-modulation data at 50.0 GeV.

The errors for the deterministic HSM are given in Table 4.7. It contains the distribution of a *single faulty BPM* in the arcs assuming a beam displacement of 250 μm which corresponds to the vertical orbit r.m.s. during polarization measurements. The contribution of the *faulty BPM set* was presented in Section 4.1. The Fourier components of each BPM are calculated and added quadratically assuming a beam position of 250 μm at each of the 16 BPMs. This leads to an uncertainty in the order of about 2.4 μm in the Fourier analysis. On average a contribution of 3.5 μm is obtained if *16 BPM* readings are not available. The *alignment error* was discussed in Section 4.2. It ranges from 4.1 μm at 41.2 GeV to 3.2 μm at 60.6 GeV. This is small compared to the average alignment contribution of 15.5 μm. The quality of deterministic HSM is improved due to the *results of k-modulation*. This information was not available in previous years. The average contribution of 21.9 μm is more than 9 times larger than the uncertainty due to faulty BPM readings in the 1997 LEP run. The *k-modulation error* contributes 2.3 μm to the harmonic content.

Energy [GeV]	41.2	44.7	45.6	50.0	55.3	60.6
Spin tune	91.5	101.5	103.5	113.5	125.5	137.5
1 faulty BPM (in ARC) [10 μm]	0.18	0.18	0.18	0.18	0.18	0.18
Faulty BPM set (16)[10 μm]	0.23	0.24	0.24	0.23	0.24	0.23
16 BPM arc/max [10 μm]	0.36	0.36	0.36	0.36	0.36	0.36
Alignment error [10 μm]	0.41	0.38	0.38	0.36	0.34	0.32
Error of k-modulation [10 μm]	0.23	0.23	0.23	0.23	0.23	0.23
Results of k-modulation [10 μm]	2.28	1.26	2.32	2.64	2.70	1.55

Table 4.7: Summary of the errors on the Fourier components and k-modulation harmonics in the energy range of 41.2 to 60.6 GeV. The values represent the average strengths of the integer resonances $k, k+1$ next to the spin tune and are calculated with $(c_k^2 + c_{k+1}^2)^{1/2}$.

Despite all this information, especially the gain due to k-modulation, the remaining errors in the Fourier analysis are too large to observe a sufficient polarization level for energy calibration at energies beyond 50 GeV with only deterministic HSM. Since the depolarizing effect of the integer resonances increases with energy (see Fig. 3.12, 3.13) a more precise compensation is required. As a consequence, deterministic HSM must be completed by an additional empirical scan of the spin harmonics.

Chapter 5

Polarization Measurements

Following the predictions by simulation that the 60/60 optics would yield higher polarization (see Section 3.6) the decision was taken to use this optics for 1997. LEP was operated with a 90/60 optics for colliding beams at 45.6 GeV and at 91.5 GeV. For this reason an energy calibration at least at one energy was needed to cross-calibrate both optics. The polarization levels which were obtained with the 60/60 and the 90/60 optics are given in Table 5.1 and plotted in Fig. 5.1. The reduction of the polarization level at higher energy is clearly observed as it was predicted in the simulations. The machine operation is different for polarization measurements. LEP is

Fill	41.2 GeV	44.7 GeV	50.0 GeV	55.3 GeV	60.6 GeV	Optics
4000		5%				90/60
4121		24%	3%			60/60
4237		16%	14.5%			60/60
4242	7 %	13%	8%	3%		60/60
4274		9%				90/60
4279	11%	12%	11%	4.5%		60/60
4280					1-2%	60/60
4372	14%	10%	4%			60/60

Table 5.1: Maximum polarization levels measured in 1997 for the various fills and energies.

filled with eight electron bunches. To obtain a sufficient polarization the vertical orbit r.m.s. is corrected to the smallest possible r.m.s. usually slightly below 0.3 mm. For physics fills, where the emphasis is on small beam emittance and high luminosity, the typical r.m.s. is in the range of 0.5 mm. As mentioned in Section 3.3 the fractional part of the betatron tunes Q_x, Q_y are close to synchro-betatron resonances ($Q_{x,y} = n + m \cdot Q_s$). This is a delicate working point as small tune changes or drifts can lead to coherent beam oscillations or beam losses. In addition, the Q_s is reduced with RF voltage changes during polarization fills. Particularly during the first experiments, part of the beam can be lost during the tune and RF manipulations that are required to setup the machine before the polarization measurement can start. During the 1997 LEP run at least part of the beam was lost five times during the machine settings procedure after the electrons were accelerated to the calibration energy.

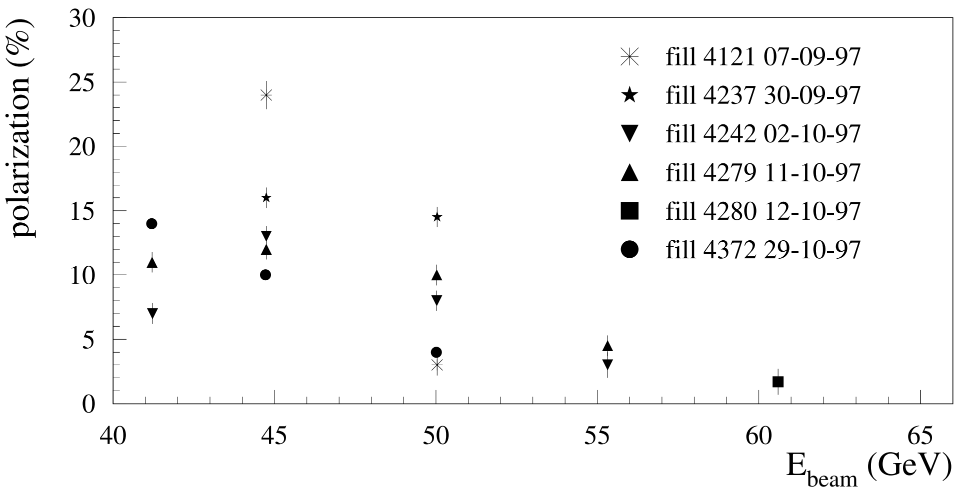

Figure 5.1: Maximum polarization levels measured in 1997 in the various fills as a function of energy. Deterministic and empirical HSM were used beyond 45 GeV. The polarization levels at higher energies fit the predicted energy dependence derived from simulations.

5.1 Polarization Results with the 90/60 Optics

The cross-calibration with the 90/60 optics was successfully made twice during the 1997 run. The solenoid fields were left on in order to calibrate with machine settings as close as possible to physics conditions of the machine. Local orbit bumps are required to compensate the spin rotation in the solenoids (see Section 3.7.2). The bumps are calculated with MAD for a perfect machine. Since the bump amplitudes reach 10 mm, as can be seen in Fig. 5.2, the usual focusing errors found in LEP can easily give a non-closure of the bumps with a betatron oscillation propagating over the complete ring. These oscillations were first corrected without paying attention to which corrector was used and sufficient polarization levels were observed (in 1994 up to 20%). First calibration attempts at 45.6 and 44.7 GeV failed because the polarization did not exceed 3%. A second attempt at 44.7 GeV gave 5% polarization without HSM. For this fill the same correctors that form the solenoid bumps were used to close the bumps. Optimised tune settings and a better corrected

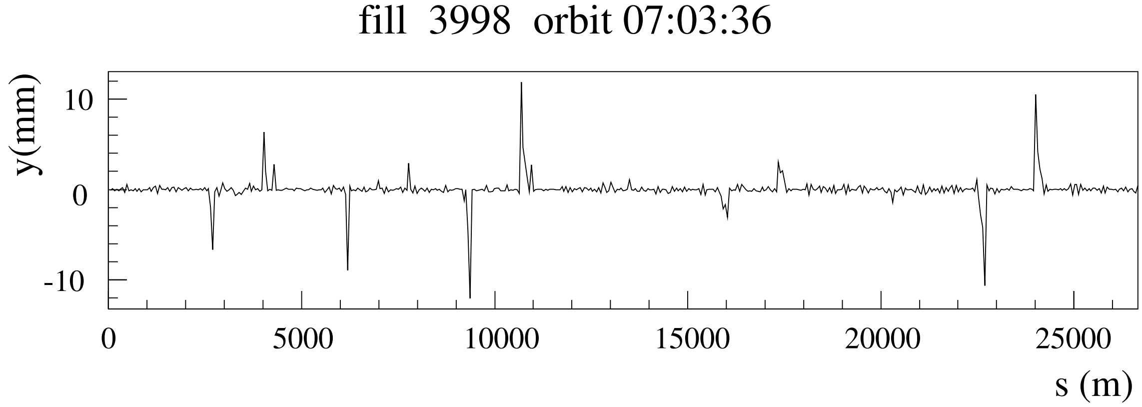

Figure 5.2: Vertical orbit of fill 3998 with the solenoid compensation bumps. The amplitude of the bumps reach 10 mm.

vertical orbit gave 9% polarization in a second cross-calibration (fill 4274). As a consequence of the higher polarization it was possible to complete the measurement in only 4 hours compared to more than 10 hours for the first cross-calibration.

5.2 Polarization Results with the 60/60 Optics

For the first time, polarization was observed at 60.6 GeV and an energy calibration was completed at 55.3 GeV during the 1997 LEP run. Another success was the calibration of 4 different energy points in a single fill, i.e. during a single magnet ramp. The solenoids were switched off for measurements with the 60/60 optics. These results confirm the simulations and justify the effort which has been made to install the k-modulation in the arcs, to switch off the solenoid magnets and to commission the polarization optics.

In 1996 a polarization level of 10% was achieved with the 90/60 optics at 50 GeV. In comparison, the 60/60 optics yielded a maximum polarization of almost 15% at the same energy (see Fig. 5.3) in 1997. In fairness it should, however, be stressed that the situation was also much more favourable for the 60/60 optics (more simulations, k-modulation and alignment information). The beam energy was calibrated four times at 50 GeV. Excepting the first calibration where an equilibrium level of 3% was reached, the k-modulation data was used and polarization levels of $14.5\%, 8\%$ and 11% were achieved. It was also possible in fill 4279 to reload an old polarization orbit of fill 4237 and to observe immediately a level 8%.

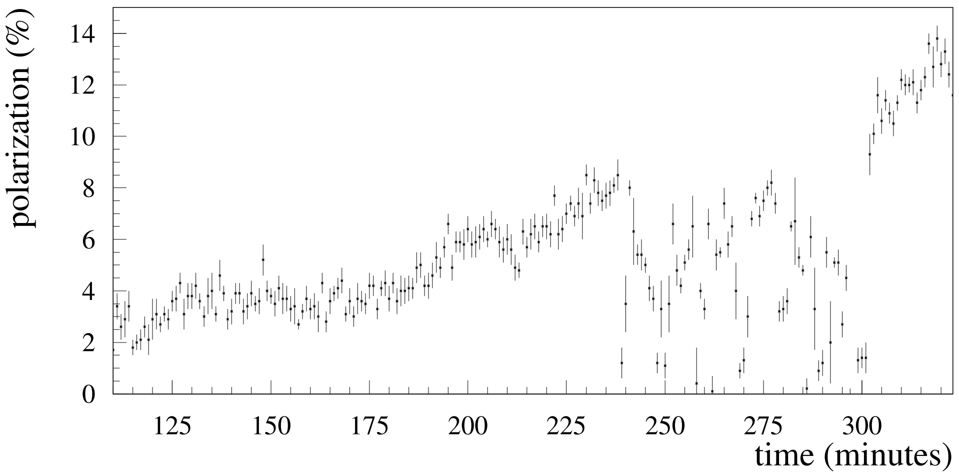

Figure 5.3: The highest polarization level which was ever reached at 50 GeV. The scale is in minutes from the moment when the machine was set to 50 GeV. The plot demonstrates the improvement due to the use of the 60/60 optics; optimised tune settings, deterministic HSM including the k-modulation data and to empirical HSM using the alignment information. The energy calibration was finished before the maximum level was achieved.

As mentioned in Section 3.2 the extrapolation uncertainties of the beam energy depends, among other things, on the linearity of the calibration points and the highest calibrated energy. It was possible to calibrate twice (fill 4242 and fill 4279) at 41.2, 44.7, 50.0 and 55.3 GeV with $P(55.3\,\mathrm{GeV}) = 3$ and 4.5% (see Fig. 5.4).

Since a level of 5% is sufficient for a successful energy calibration, the polarization was not optimised at 41.2 GeV and 44.7 GeV with deterministic or empirical HSM in order to save time

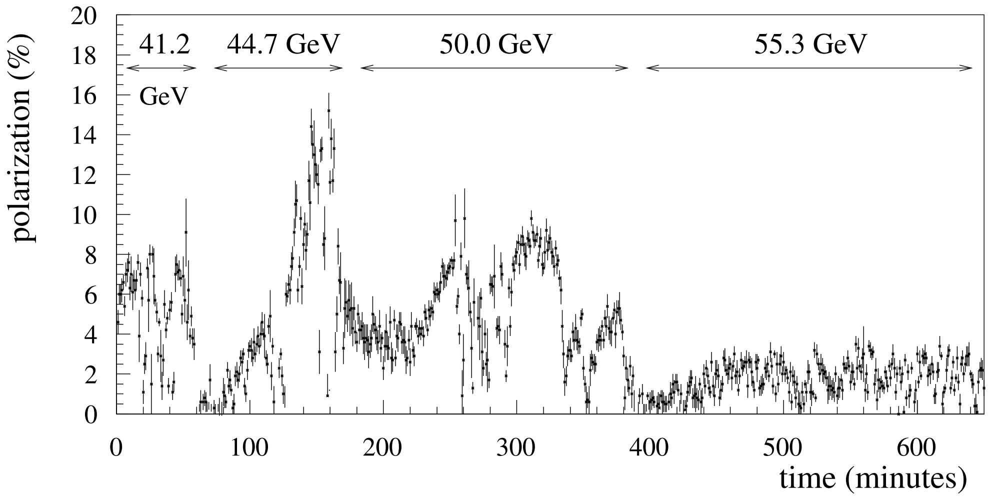

Figure 5.4: Polarization in fill 4242. This was the first time with four energy calibrations in a single fill (i.e. within a single magnet ramp).

and to calibrate at higher energies with the scheduled time. The fastest calibration was made in fill 4279: within 10 hours, three different energies were measured with resonant depolarization.

The 60/60 optics does not use the super-conducting low beta quadrupoles QS0 to avoid the problems of orbit drifts due to a mechanical movement of those quadrupoles. Additional time was allocated for polarization during a 46 hour stop of the cryogenic system in IP8. This time allowed for polarization studies at 50.0 and 55.3 GeV. The tune settings could be optimised and the strength of synchrotron sidebands was observed. The polarization level behaved as predicted by the synchrotron sideband model (see Fig. 5.5). The time was also used to search for polarization at 60.6 GeV in fill 4280. Unfortunately, the polarization level of about 1% was too low for a calibration.

The consistency and quality of the orbit, alignment and k-modulation data can be tested by a comparison of the respective spin harmonics. Indeed, for orbits where the k-modulation data is included, the measured BPM reading harmonics after deterministic and empirical HSM should match the harmonics of the alignment data. The numbers are given in Table 5.2. The orbit harmonics correspond to the highest polarization levels which were achieved at 50.0 GeV. They do not match the alignment components, neither for the 1997 data before the startup nor for the measurements just after the LEP run.

Dataset	a_{113} [10μm]	b_{113} [10μm]	a_{114} [10μm]	b_{114} [10μm]
Fill 4237 (16 BPM wrong)	2.63	-4.67	-0.49	-1.19
Fill 4279 (16 BPM wrong)	1.20	-2.79	-0.78	-1.88
Alignment 97_{start}	0.94	-1.64	0.21	2.30
Alignment 97_{end}	1.83	-0.59	2.25	1.07
k-modulation	4.22	-0.67	-2.67	-0.17

Table 5.2: Comparison of the harmonics corresponding to the highest polarization which was observed after empirical HSM with the alignment and k-modulation data at 50.0 GeV.

It has to be mentioned that this comparison strongly depends on the question whether the polarization was absolutely optimised or only partially. It is further aggravated by the uncertainty of the Fourier analysis due to missing BPM readings. In addition, the differences in the Fourier components after empirical HSM in fill 4237 and fill 4279 indicate that the variations from fill to fill are too large to quantify the precession of deterministic HSM (see Section 5.3).

5.3 Comparison with Simulations

The influence of synchrotron sidebands was observed in fill 4242 and fill 4279. At 50.0 GeV and at 55.3 GeV the polarization level was measured as a function of the spin tune by varying the RF frequency (see Fig. 5.5). The polarization degree followed the curve predicted by simulations.

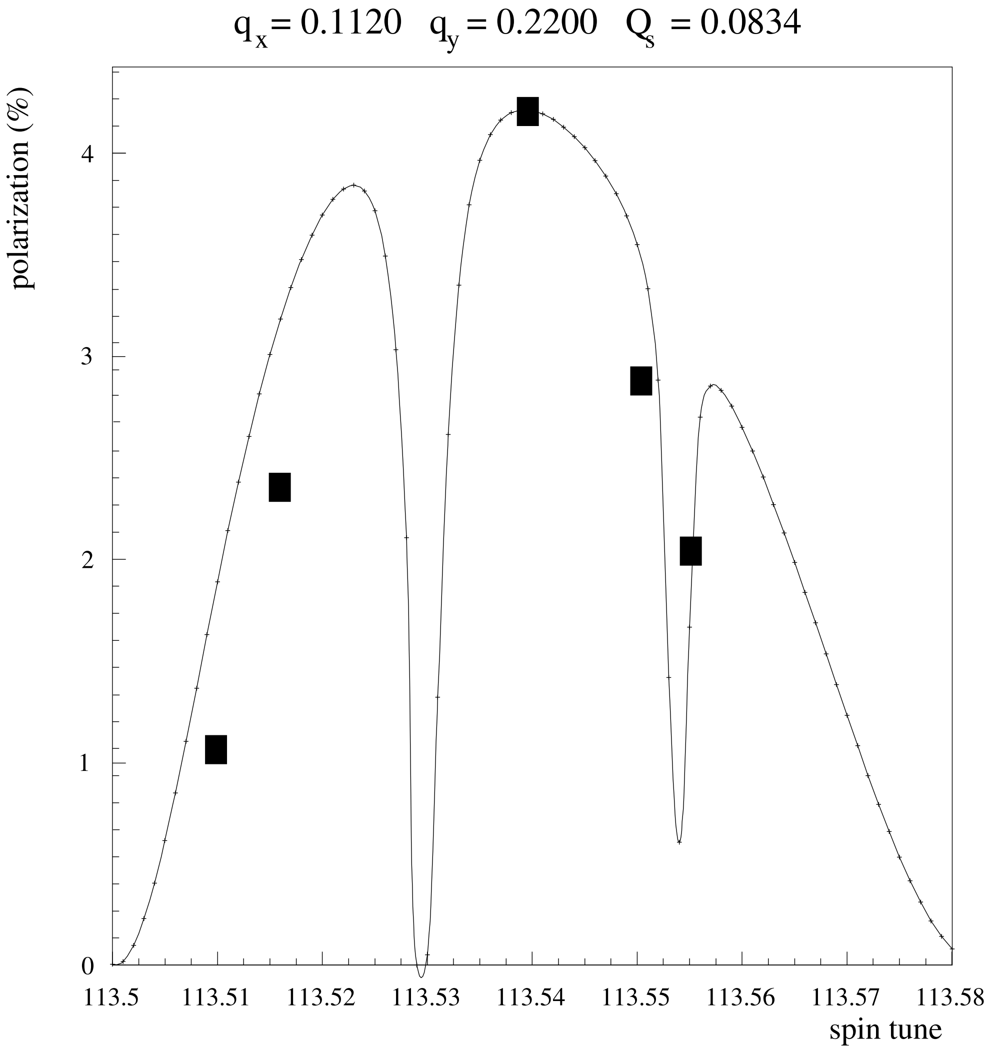

Figure 5.5: Polarization level as a function of the spin tune at 50.0 GeV. The black squares correspond to the measured polarization. The tune settings are indicated above. The energy is shifted by changing the RF frequency. A frequency shift of the RF cavities changes the beam position in the quadrupoles and the integrated magnetic field seen by the beam without varying the tune settings. The solid line represents the simulation prediction. The maximum of the prediction is fitted to the measured polarization value.

After correcting the vertical orbit, setting the tunes and applying deterministic HSM including the k-modulation data polarization was observed immediately at 50.0 and 55.3 GeV. For example, deterministic HSM gave a polarization of only 2.9% at 50 GeV (fill 4121) without the k-modulation data compared with 3.7% when the k-modulation result was included.

It should be noted that the harmonic components of the successful energy calibration fills (see Appendix B) can scatter from fill to fill up to 30 μm even after empirical scan. The sources of the harmonic changes cannot be determined as they are a mixture of harmonic uncertainties due to missing BPMs, orbit corrections, tune settings, etc.

However, an empirical scan of the HSM bumps was needed to finalise the maximum polarization degree, which more than doubled the polarization and gave larger improvements than expected in the simulations (polarization with deterministic HSM including k-modulation results was about 60% of the empirical value, see Fig. 3.18 in linear simulations and about 50% in non-linear calculations).

The SITF and BESSEL calculations predict an evolution of the polarization versus energy in agreement with the measurement data. The most obvious error of the simulations is the absolute value (see Table 5.3) which differs roughly by a factor of 2. The factor between experiment and

Energy [GeV]	50.0	55.3	60.6
Simulation $\%$	23 ± 4	11 ± 2	4 ± 2
Measurement $\%$	14 ± 2	5 ± 1	2 ± 1

Table 5.3: The simulated and measured polarization value at different energies during the 1997 LEP run with the 60/60 optics non-linear simulation with SITF-BESSEL; the simulation error is delivered by the scatter of calculated different alignments; the measured error is given by the polarization scale error.

simulation could be either due to the fact that the "absolute limit" of the polarization was not found during the experiments, or that the size of the errors used in the simulations were underestimated. Systematic errors occur due to the fact that the orbit corrections in MAD are quite optimistic and that the linear algorithm of SITF does not take higher orders of the coupling between the spin and orbit motion into account. The non-linear results are derived from the influence of the synchrotron sidebands and leaving out other non-linear influences.

5.4 Energy Calibration Results

Fig. 5.6 shows the lever arms of energy calibration in 1996 (5.3 GeV) and in 1997 (14.1 GeV) which are used to check the linearity of the beam energy extrapolation. The increase of the calibration range as well as the number of calibrations lead to a preliminary beam energy error of 29 MeV at E_{beam} = 91.5 GeV [46] compared to 35 MeV that would be obtained with the results of 1996 [26] (see Fig. 5.6). The improved energy calibration together with the increased amount of reconstructed W bosons give the direct determination of the W mass m_W = 80.35 ± 0.09 GeV. This is the most accurate measurement to date. The world average value which combines the indirect LEP I measurements, proton colliders results and the LEP II data is $m_W = 80.375 \pm 0.064$ GeV [47].

The different contributions to the beam energy error are summarised in Table 5.4. At a beam energy of 91.5 GeV, the comparison of NMR probes and resonant depolarization over the calibrated

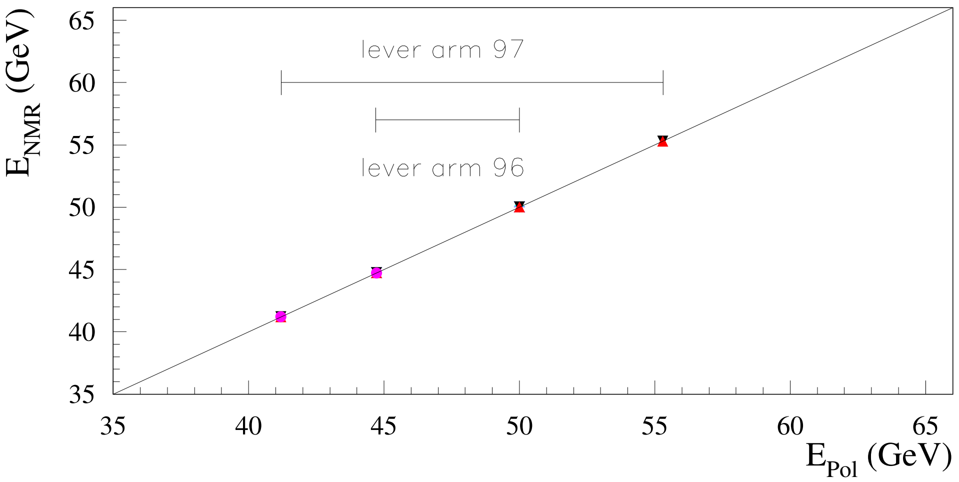

Figure 5.6: Improvement of the *lever arm* for the extrapolation of beam energy in 1997. It was increased from 5.3 GeV to 14.1 GeV.

energy range gives a contribution to the error of 10 MeV and an NMR scatter of 5 MeV (see Fig. 5.7).

The shapes of the NMRs are compared with the flux loop measurements to find deviations from a linear energy dependence in the energy range where no resonant depolarization is available. These differences are dominating the beam energy error with 20 MeV and a scatter of 10 MeV. They are studied and analysed in order to understand the reasons. The bending field which is not covered in the flux loop contributes an error of 12 MeV. It is given by the injection magnets which are equipped with additional NMR probes for the LEP run 1998 to reduce this error. The cross-calibrations show an energy difference of both optics of 4 MeV. The corrector settings are also various and give an energy uncertainty of 6 MeV. The energy calculation at the IPs is covered by the RF model. The energy files are generated every 15 minutes which means that RF voltage changes during this time are not considered. The RF related errors together with the dispersion influence are in the order of 2 to 3 MeV.

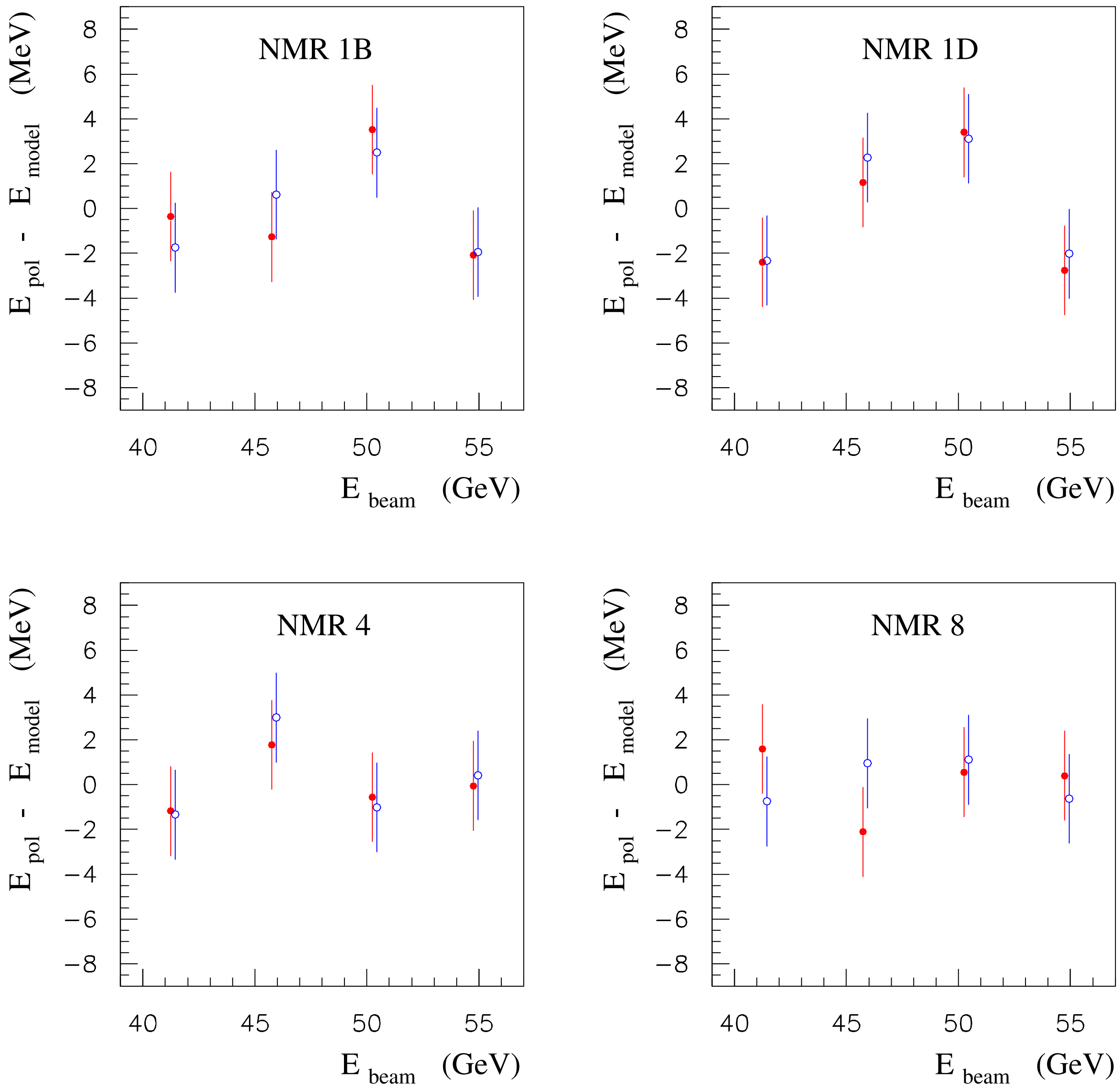

Figure 5.7: Residuals of a linear fit of the NMR field as a function of the resonant depolarization energy (after correction for effects due to quadrupoles) for 4 of the 16 NMR probes (fill 4242, 4279). The residuals of the 4 NMRs have been converted to MeV. Each NMR has its own characteristic residual shape which is due to the fact that the local field can differ significantly from the mean, represented by the resonant depolarization energy. The NMR specific shapes are reproduced in both fills. The plot is taken from 'Preliminary LEP energy calibration for 1997 data' [46].

Source	Error [MeV]		
	91.5 GeV	65/68 GeV	45.6 GeV
Polarization systematic	1	1	1
e^+/e^- energy difference	2	2	2
Optics difference	4	3	2
Extrapolation from NMR-polarization			
NMR r.m.s. for two parameter fit	10	5	0
Different E_{Pol} fills	5	3	2
Flux-loop test of extrapolation			
NMR flux-loop difference per fill	20	10	0
NMR scatter	10	5	0
3.5% of field not measured by FL			
with 1% uncertainty over 55 to 90 GeV	12	6	0
Corrector effects	6	6	6
Tide	1	1	1
Dipole rise modelling	1	1	2
RF frequency shift (15 min sampling)	3	0	0
IP specific corrections ($\sigma(E_{CM})/2$)			
RF model	3	3	3
Dispersion	2	2	2
Total	29	16	8

Table 5.4: Summary of beam energy errors. They are given for the different energies at which LEP was operated in 1997. The table is taken from 'Preliminary LEP energy calibration for 1997 data' [46].

Chapter 6

Conclusions

The compensation of depolarizing effects was improved by determination of the beam position monitor (BPM) offsets, the analysis of the mechanical misalignment of the quadrupoles and optimised machine settings. This led for the first time during the 1997 LEP run to the energy calibration at 55.3 GeV with the resonant depolarization method during the 1997 LEP run. Due to the calibration at the higher energy the beam energy uncertainty was reduced at 91.5 GeV to 29 MeV. It was possible to get a polarization level up to 15% at 50.0 GeV and to observe polarization at 60.6 GeV. Energy calibrations at four different energies per fill were reached twice and allow an improved linearity check of the beam energy error extrapolation compared to the year 1996.

It has been shown that polarization simulations are very useful to prepare polarization measurements. Different optics were compared in detail before the decision for the polarization optics was made. Measurements proved that the energy dependence of the polarization was predicted in the right way. The tune settings could be optimised. The polarization limiting influence of non-linear synchrotron resonances was observed during the measurements.

The analysis of the quadrupole magnet misalignment showed that the statistical errors of the measurements procedure are small compared to the determined vertical magnet positions and that the harmonic content of the alignment data can be used to improve the deterministic Harmonic Spin Matching (HSM). It was explained that the lowest harmonics have to be taken out in order to steer the beam according to the orbit given by the alignment data. The influence of the smoothing procedure in the harmonic content was derived to be small.

The dynamic beam based alignment of the beam position monitors with k-modulation has been continuously improved over the last four years. The principle and operation procedure of k-modulation was explained. The measurement results of the BPM offset calibrations in the bending area of LEP were discussed. The analysis gave an average r.m.s. value of $270\,\mu$m for the BPM offsets. It was seen that the Fourier components of the k-modulation results are very large. A justification of the determined offsets is needed during the 1998 LEP run because of unexpected time dependencies.

The quality of deterministic HSM was discussed. Systematic errors in the Fourier analysis due to the number of available BPMs are given. The uncertainty of the recalibration of the HSM bumps coming from the use of two different calculations of the harmonic content was calculated. During 1998 an attempt will be made to change the implemention of the HSM bumps in order to avoid the use of different harmonic content calculations. It was proved that despite the k-modulation results, the remaining errors of the harmonics require empirical HSM to achieve the highest polarization level.

It was shown that a few faulty vertical beam position readings can significantly change the Fourier spectrum. In order to make the deterministic HSM more reliable a larger number of permanently working BPMs are needed.

A quantitative estimate of the deterministic HSM precession is not possible. The attempt to use the alignment data gave contradictory results. A further increase of polarization might be achieved by making better use of the quadrupole alignment data. The time dependent fluctuations in the harmonic content due to orbit changes can be recorded using the developed program FOURIER.

The polarization results proved that the combined use of the k-modulation results, careful tune settings and the new polarization optics was successful. The same machine parameters will be used for polarization measurements during the 1998 LEP run. A comparison of the measured polarization levels in the year 1997 with deterministic HSM results at 45 GeV is not possible since depolarizing effects are much stronger at higher energies.

Appendix A

Polarization Calculations

A.1 Local closed Orbit Bumps

The dipole corrector magnets are not only used to correct the kicks due to misplaced quadrupoles but also to steer the beams locally with closed orbit bumps. There are several types of bumps: two-corrector bumps can only be closed if the phase advance between the two corrector magnets is a multiple of π. Three-corrector bumps allow a bump amplitude x_0 at any location s_0 between the correctors (provided the phase advances are not multiples of $\pi/2$). The required deflection angles θ_i of the corrector magnets are given by the beta function β_i and phase μ_i at their position s_i and of course the desired amplitude x_0

$$\begin{aligned}\theta_1 &= \frac{x_0}{\sqrt{\beta_1\beta_2}\sin(\mu_2-\mu_1)}\\ \theta_2 &= -\frac{x_0\sin(\mu_3-\mu_1)}{\beta_2\sin(\mu_2-\mu_1)\sin(\mu_3-\mu_2)}\\ \theta_3 &= \frac{x_0}{\sqrt{\beta_2\beta_3}\sin(\mu_3-\mu_2)}.\end{aligned} \tag{A.1}$$

With four-corrector bumps the displacement x_0 and the angle x_0' can be adjusted at many positions s_0 of the accelerator provided that the phase advances are adequate. This bump is used for example when x_0' should be zero at the position x_0. The corrector magnet deflections θ_i at the longitudinal positions s_i are derived to be

$$\begin{aligned}\theta_1 &= \frac{1}{\sqrt{\beta_1\beta_0}}\frac{\cos(\mu_0-\mu_2)-\alpha_0\sin(\mu_0-\mu_2)}{\sin(\mu_2-\mu_1)}x_0-\sqrt{\frac{\beta_0}{\beta_1}}\frac{\sin(\mu_0-\mu_2)}{\sin(\mu_2-\mu_1)}x_0'\\ \theta_2 &= -\frac{1}{\sqrt{\beta_2\beta_0}}\frac{\cos(\mu_0-\mu_1)-\alpha_0\sin(\mu_0-\mu_1)}{\sin(\mu_2-\mu_1)}x_0+\sqrt{\frac{\beta_0}{\beta_2}}\frac{\sin(\mu_0-\mu_1)}{\sin(\mu_2-\mu_1)}x_0'\\ \theta_3 &= -\frac{1}{\sqrt{\beta_3\beta_0}}\frac{\cos(\mu_4-\mu_0)-\alpha_0\sin(\mu_4-\mu_0)}{\sin(\mu_4-\mu_3)}x_0-\sqrt{\frac{\beta_0}{\beta_3}}\frac{\sin(\mu_4-\mu_0)}{\sin(\mu_4-\mu_3)}x_0'\\ \theta_4 &= \frac{1}{\sqrt{\beta_4\beta_0}}\frac{\cos(\mu_3-\mu_0)-\alpha_0\sin(\mu_3-\mu_0)}{\sin(\mu_4-\mu_3)}x_0+\sqrt{\frac{\beta_0}{\beta_4}}\frac{\sin(\mu_3-\mu_0)}{\sin(\mu_4-\mu_3)}x_0'\end{aligned} \tag{A.2}$$

where $\mu_i \equiv \mu(s_i)$ are the betatron phases. In addition $\mu(s_1) < \mu(s_2) < \mu(s_3) < \mu(s_4)$.

A.2 Spin Orbit Coupling

In order to calculate the coupling vector of the spin-orbit motion $\vec{d}$ it is more favourable to use the general angle coordinate $\theta = s/R$ than s. The spin motion is considered in the coordinate system $(\vec{n}_0, \vec{m}_0, \vec{l}_0)$. Thus the spin rotates around $\vec{n}_0$. With $\vec{k}_0 = \vec{m}_0 + i\vec{n}_0$ it follows that

$$\vec{k}_0(\theta + 2\pi) = \exp(2\pi i\nu)\vec{k}_0. \tag{A.3}$$

Assuming a perfect storage ring, $\vec{d}$ is given in the linear approximation by

$$\begin{aligned} \vec{d} &= \frac{1}{2}\Re\left[\vec{k}_0^* \cdot \sum_j \Xi_{\pm j}\right], & \text{(A.4)} \\ \Xi_{\pm j}(\theta) &= R_{\pm j} \cdot A_{\pm j}(\theta) \cdot V_{\pm j}(\theta), \qquad j = s, x, y. & \text{(A.5)} \end{aligned}$$

The R term describes the resonant depolarization

$$R_{\pm j} = \frac{i}{1 - \exp[2\pi i(\nu \pm Q_j)]}. \tag{A.6}$$

The amplitude of the orbit energy oscillations is proportional to the photon energy which has been emitted and is expressed by $A_{\pm j}(\theta)$. The absolute value of A is unity. In the longitudinal direction it becomes

$$A_{\pm s}(\theta) = \exp(\mp iQ_s\theta). \tag{A.7}$$

In the transverse motion A is given by the Twiss functions

$$A_{\pm j}(\theta) = \frac{\exp[\mp\psi_j(\theta)]}{\sqrt{\beta_j(\theta)}}\left[-D_j(\theta) \pm i(D'_j(\theta)\beta_j(\theta) + D_j(\theta)\alpha_j(\theta))\right], \qquad j = x, y. \tag{A.8}$$

The influence of betatron or synchrotron oscillations $V_{\pm j}(\theta)$ is summarised by integrating over one particle revolution

$$\begin{aligned} V_{\pm j}(\theta) &= \int_\theta^{\theta+2\pi} \left[-(\vec{k}_0 \cdot e_j)(a\gamma + 1)f(\theta')\sqrt{\beta_j}\exp \pm i\psi_j\right] R_{\pm j}d\theta' \qquad j = x, y & \text{(A.9)} \\ V_{\pm s}(\theta) &= \int_\theta^{\theta+2\pi} \left[\vec{k}_0(D_x e_y + D_y e_x)(a\gamma + 1)f(\theta')\right] R_{\pm s}\exp \pm iQ_s\theta' d\theta'. & \text{(A.10)} \end{aligned}$$

$V(\theta)$ are functions of the lattice and spin. Higher order spin integrals contain more powers of ν.

A.3 Strength of the Synchrotron Sidebands

The analytical calculation of the synchrotron sidebands strengths for an integer resonance is given by [16]

$$\frac{11}{18}\left\langle \oint \frac{ds}{|\rho|^3} \,|\, \vec{d}\,|^2 \right\rangle = A\left(\oint \frac{ds}{|\rho|^3}\right)\sum_{m=-\infty}^{\infty}\left[\frac{\Delta\nu}{(\Delta\nu + mQ_s)^2 - Q_s^2}\right]^2 e^{-\gamma^2} I_m(\lambda^2) \tag{A.11}$$

where $\Delta\nu = \nu - p$ is the distance from the integer, m corresponds to the m^{th} resonance order and I_m is a modified Bessel function [16]. The strength A of the first order synchrotron resonance becomes

$$\frac{11}{18}\left\langle \oint \frac{ds}{|\rho|^3} |\vec{d}|^2 \right\rangle_{(\lambda=0)} \Big/ \left(\oint \frac{ds}{|\rho|^3} \right) = A\left[\frac{\Delta\nu}{(\Delta\nu + mQ_s)^2 - Q_s^2}\right]^2, \approx \frac{A}{4(\Delta\nu + Q_s)^2} + \frac{A}{4(\Delta\nu - Q_s)^2}. \quad \text{(A.12)}$$

The sideband spectrum for a single linear betatron resonance is given by

$$\frac{11}{18}\left\langle \oint \frac{ds}{|\rho|^3} |\vec{d}|^2 \right\rangle = B\left(\oint \frac{ds}{|\rho|^3} \right) \sum_{m=-\infty}^{\infty} \left(\frac{e^{-\lambda^2}}{(\Delta\nu + mQ_s)^2}\left[J_{x,y} I_m(\lambda^2) + J_s \frac{\lambda^2}{2}\left(I_{m-1}(\lambda^2)\right)\right] + \frac{e^{-\lambda^2}}{\Delta\nu + mQ_s}\frac{mJ_s}{Q_s} I_m(\lambda^2)\right), \quad \text{(A.13)}$$

where B is a constant, $J_{s,x,y}$ are the radiation damping partition numbers which indicate the damping strengths in the longitudinal and transverse motion due to synchrotron radiation. Since two parent betatron resonances are present, the fit to the first order resonances is

$$\frac{11}{18}\left\langle \oint \frac{ds}{|\rho|^3} |\vec{d}|^2 \right\rangle_{(\lambda=0)} \Big/ \left(\oint \frac{ds}{|\rho|^3} \right) = \frac{B_1 J_x}{(\nu - Q_x - 4)^2} + \frac{B_2 J_y}{(\nu - Q_y - 4)^2}. \quad \text{(A.14)}$$

Appendix B

Tables of Harmonic Contents

The following tables refer to the analysis of the alignment and k-modulation data and to the polarization measurements made during the LEP run 1997.

Comment	Fill	Time	Fourier components [10μm]				$P[\%]$
			a_{113}	b_{113}	a_{114}	b_{114}	
First no k-modulation	4121	02:43	-3.37	0.76	1.07	1.46	1.9
Deterministic HSM no k-modulation	4121	04:54	0.46	0.17	-0.61	0.49	2.3
Empirical HSM no k-modulation	4121	08:50	-2.08	-1.52	-0.55	0.41	3.5
First	4237	01:42	-1.71	-0.72	2.88	0.21	3.5
Deterministic HSM	4237	04:24	0.92	0.01	-0.85	0.81	3.7
Empirical HSM	4237	07:41	2.56	-4.54	-0.28	-1.41	14.5
Reload	4242	00:57	-0.72	-5.37	-0.96	-0.46	4.0
Deterministic HSM	4242	01:21	0.95	-3.42	-0.89	-1.20	4.0
Empirical HSM	4242	01:56	-1.63	-3.46	1.41	-1.04	8.0
Reload	4279	18:59	2.52	-4.95	-0.40	-1.03	10.0
Empirical HSM	4279	22:51	2.80	-4.94	-0.24	-0.98	11.0
Alig+det HSM	4279	01:56	-0.38	-1.34	1.52	0.35	8.0
Reload	4372	01:43	-2.60	2.27	-0.95	0.84	2
Deterministic HSM	4372	02:03	1.24	0.60	-0.65	1.67	4
Empirical HSM	4372	04:30	-1.11	0.41	-0.17	0.79	4

Table B.1: Harmonic components in 60/60 polarization fills at 50.0 GeV. The components are given for the *first* polarization measurement after setting the machine respective to the orbit *reload*; the polarization level after the *deterministic HSM* and after *empirical HSM* optimisation. The set of 16 faulty BPMs was disabled for every Fourier analysis.

Comment	Fill	Time	Fourier components				$P[\%]$
			a_{125}	b_{125}	a_{126}	b_{126}	
First	4242	06:32	-0.95	-0.40	6.04	2.28	1.9
Deterministic HSM	4242	06:41	0.91	-0.11	-1.77	1.21	2.3
Empirical HSM	4121	08:56	-2.34	-0.28	2.35	0.96	3.0
Reload	4279	07:21	3.35	-1.44	4.47	2.89	2.0
Deterministic HSM	4279	09:12	-0.46	-1.00	4.40	1.87	3.0
Empirical HSM	4279	14:28	-1.70	0.45	2.22	1.73	4.5

Table B.2: Fourier components in successful 60/60 polarization fills at 55.3 GeV. The entries are the same as in Table B.1.

Comment	Fill	Time	Fourier components				$P[\%]$
			a_{137}	b_{137}	a_{138}	b_{138}	
First	4280	19:11	-1.89	0.22	1.49	-0.49	0.5
Deterministic HSM	4280	01:32	0.30	-0.86	1.08	0.23	0.0
Empirical HSM	4280	02:30	-1.09	0.87	1.09	0.41	1.5

Table B.3: Fourier components in the 60/60 optics polarization fill 4280 at 60.6 GeV. The entries are the same as in Table B.1.

	Alignment files							k-mod
	h1	h2	h4	h4p30	h4p70	h2p30	h2p70	
σ_y [μm]	824	426	494	183	242	183	242	267
Fourier components [10μm]								
a_{93}	1.90	1.91	1.91	1.44	1.60	1.44	1.60	-1.16
b_{93}	-1.98	-1.97	-1.97	-1.64	-1.83	-1.63	-1.82	1.23
a_{94}	-0.28	-0.43	-0.28	-0.13	-0.34	-0.13	-0.34	-3.15
b_{94}	-2.25	-1.58	-2.25	-1.30	-1.42	-1.29	-1.43	1.60
a_{101}	-2.18	-2.18	-2.18	-2.40	-2.46	-2.38	-2.46	1.26
b_{101}	-0.83	-0.83	-0.83	-0.73	-0.64	-0.72	-0.64	-0.18
a_{102}	0.87	0.70	0.87	0.87	0.81	0.89	0.81	-0.13
b_{102}	-3.20	-2.42	-3.19	-2.04	-2.32	-2.03	-2.31	-0.28
a_{103}	-3.12	-2.97	-2.97	-2.76	-2.92	-2.76	-2.92	1.92
b_{103}	-2.85	-2.80	-2.80	-2.61	-2.66	-2.61	-2.66	0.48
a_{104}	-3.47	-3.45	-3.44	-3.37	-3.37	-3.37	-3.38	3.09
b_{104}	0.91	0.91	0.91	0.63	0.86	0.63	-0.86	-1.41
a_{113}	0.79	0.94	0.94	0.52	0.53	0.51	-0.95	4.22
b_{113}	-1.59	-1.64	-1.64	-1.31	-1.46	-1.31	-0.35	-0.67
a_{114}	0.218	0.07	0.21	0.03	0.03	0.03	0.02	-2.67
b_{114}	2.30	1.64	2.30	1.25	1.43	1.25	1.43	-0.17
a_{125}	-1.00	-0.99	-0.00	-0.79	-0.95	-0.79	-0.95	-0.68
b_{125}	-0.38	-0.39	-0.38	-0.19	-0.36	-0.20	-0.35	1.79
a_{126}	-1.86	-2.02	-1.86	-2.10	-2.03	-2.10	-2.10	5.40
b_{126}	0.34	1.04	0.34	0.27	1.19	1.22	1.20	-0.69
a_{137}	0.20	0.31	0.31	0.27	0.28	0.27	0.28	0.63
b_{137}	-0.58	-0.62	-0.62	-0.69	-0.69	-0.68	-0.70	1.20
a_{138}	1.87	1.76	1.88	1.83	1.84	1.84	1.84	0.85
b_{138}	0.50	-0.06	0.50	-0.28	-0.17	-0.28	-0.18	-0.68

Table B.4: Fourier components of the alignment at the beginning of 1997 and the k-modulation results. The alignment files represent the different harmonics which were taken out and the smoothing of the measurements. The notification was introduced in Section 4.2. The Fourier analysis included every beam position monitor in the bending area of LEP.

Bibliography

[1] LEP design report. CERN-LEP/84-01, June 1984. Vol. I,II.

[2] LEP Electroweak Working Group. A combination of preliminary LEP electroweak measurements and constraints on the standard model. CERN/PPE 95-172, 1995.

[3] E.B. Courant and H.S. Snyder. Theory of the alternating gradient synchrotron. *Ann. of Physics*, 3(1), 1958.

[4] M. Sands. The physics of electron storage rings - an introduction. SLAC-121, UC-28, 1970.

[5] D.A. Edwards and M.J. Syphers. *An introduction to the physics of high energy accelerators*. Wiley Series in Beam Physics and Accelerator Technology, 1993.

[6] J. S. Jackson. Classical electrodynamics. New York, 1975.

[7] L. Thomas. *Philos. Mag.*, 3:1, 1927.

[8] V. Bargmann *et al.* Precession of the polarization of particles moving in a homogeneous elektromagnetic field. *Phys. Rev. Lett.*, 2:435, 1959.

[9] B.W. Montague. Polarized beams in high energy storage rings. *Physics Reports*, 113(1):1–96, 1984.

[10] A.A. Sokolov and I.M. Ternov. On polarization and spin effects in the theory of synchrotron radiation. *Sov. Phys. Dokl.*, 8:1203, 1964.

[11] Ya.S. Derbenev *et al.* The motion of particle spin in an accelerator with arbitrary field. *Sov. Phys. Dokl.*, 15(6):583–585, 1970.

[12] V.N. Baier and Yu.F. Orlov. Quantum depolarization of electrons in a magnetic field. *Sov. Phys. Dokl.*, 10:1145, 1966.

[13] Ya.S. Derbenev *et al.* Radiative polarization at ultra-high energies. *Part. Acc.*, 9:247–266, 1979.

[14] J.-P. Koutchouk. Systematic integer spin resonances. In K.J. Heller, editor, *High Energy Spin Physics*, Particles and Fields Series, pages 1004–1012, 1988.

[15] J. Buon. A stochastic model of depolarization enhancement due to large energy spread in electron storage rings. In K.J. Heller, editor, 8^{th} *International Symposium on High-energy Spin Physics, Minneapolis, 1988*, Particles and Fields Series, pages 963–974, 1989.

[16] S.R. Mane. Synchrotron sideband spin resonances in high-energy electron storage rings. *Nucl. Instr. Meth.*, 292:52–74, 1990.

[17] K. Yokoya. Effects of radiative diffusion on the spin-flip in electron storage rings. *Part. Acc.*, 14:39, 1983.

[18] LEP design report. CERN-AC/96-01 (LEP2), June 1996. Vol. III.

[19] L. Arnaudon *et al.* Accurate determination of the LEP beam energy by resonant depolarization. *Z. Phys. C*, 66:45–62, 1995.

[20] B. Dehning. *Elektronen- und Positronen-Polarisation im LEP-Speicherring und Präzisionsbestimmung der Masse des Z-Teilchens*. PhD thesis, Ludwig-Maximilians-Universität München, 1995.

[21] R. Assmann. *Optimierung der transversalen Spin-Polarisation im LEP-Speicherrring und Anwendung für Präzisionsmessungen am Z-Boson*. PhD thesis, Ludwig-Maximilians-Universität München, 1994.

[22] R. Assmann *et al.* Deterministic harmonic spin matching at LEP. In *Proceedings EPAC 94*, 1994. CERN SL/94-62 (AP).

[23] R. Assmann *et al.* Polarization studies at LEP in 1993. CERN SL/94-08 (AP), 1994.

[24] The LEP Energy Working Group. Calibration of centre-of-mass energies at LEP I for precise measurements of z properties. *European Physical Journal C*, 1998.

[25] M. Placidi. Beam energy measurement at LEP II. In *Physics at LEP2*, volume 1, pages 59–74, 1996. CERN 96-01.

[26] The LEP energy working group. LEP energy calibration in 1996. LEPECAL 97-01, 1997.

[27] B. Dehning *et al.* Improvements in polarization. In *Proceedings of the eighth LEP Performance Workshop*, pages 34–39, 1998.

[28] J. Uythoven. A LEP(60,60) optics for energy calibration measurements. CERN-SL-97-58 OP, 1997.

[29] R. Rossmanith and R. Schmidt. Compensation of depolarizing effects in electron positron storage rings. *Nucl. Instr. Meth. Phys. Res.*, A(236):231–248, 1985.

[30] I. Reichel. Beam position measurement by modulation of quadrupole strengths. Master's thesis, RWTH Aachen, 1994. PITHA 94/54, CERN SL/95-50.

[31] F. Tecker. *Methods of improving the orbit determination and stability at LEP*. PhD thesis, RWTH Aachen, 1998. PITHA 98/7.

[32] H. Grote and F.-C. Iselin. *The* MAD *program*, 1990. CERN SL/90-13 (AP).

[33] H. Grote. *The* MAD-SODOM *User's Guide*, 1993. CERN SL/93-40 (AP).

[34] A. Ackermann *et al.* SITF. to be published.

[35] J. Kewisch. Simulation of electron spin depolarization with the computer code SITROS. DESY 83-032, 1983.

[36] A. Chao. The SLIM program and its limitations. In *Workshop on polarized electron acceleration and storage*, 1982. DESY M-82/09.

[37] M. Böge. *Analysis of Spin Depolarizing Effects in Electron Storage Rings*. PhD thesis, Universität Hamburg, 1994. DESY 94-087.

[38] K. Yokoya. Non-perturbative calculation of equilibrium polarization of stored electron beams. KEK Report 92-6, 1992.

[39] B. Dehning *et al.* Beam position monitor offset determination at LEP. In *1997 Particle Accelerator Conference -PAC '97, Vancouver, Canada, 12-16 May 1997*, 1997. CERN SL/97-25 (BI).

[40] J. Borer. Instrumentation and diagnostics used in LEP commisioning, with accent on the LEP beam orbit measurement system. CERN SL/90-107 (BI), 1990.

[41] J. Borer *et al.* The second generation and optimized beam orbit measurement (BOM) system of LEP: Hardware and performance description. CERN SL/95-60 (BI), 1995.

[42] M. Hublin *et al.* Maintenance of the geometry of lep, improvement and optimization of the vertical and radial smoothing. In *Proceedings of the Fourth International Workshop on Accelerator Alignment, KEK Proceedings 95-12*, pages 132–139, 1995.

[43] D. Brandt *et al.* A new closed orbit correction procedure for the CERN SPS and LEP. *Nucl.Instr.Meth.*, A(293):305–307, 1990.

[44] G. Crockford *et al.* COCU user guide.

[45] I. Barnett *et al.* Dynamic beam based alignment. In *2^{nd} European Workshop on Beam Diagnostics and Instrumentation for Particle Accelerators, DESY M - 95 07*, 1995. CERN SL/94-84 (BI).

[46] The LEP energy working group. Preliminary LEP energy calibration for 1997 data. LEP-ECAL 98-01, 1998.

[47] A. Weber. Erzeugung schwerer Eichbosonen. In *Seminar of the spring conference of the German Physical Society, 23-27 March 1998, Germany*, 1998.

Acknowledgments

I would like to thank Priv. Doz. Dr. Manfred Tonutti for his initiative which made it possible to do this Diploma work at CERN and the idea for the interesting subject. I express my gratitude to Prof. Dr. Albrecht Böhm for his assistance.

Bernd Dehning instructed me at CERN and helped me when I applied. Claude Bovet enabled me to stay at CERN and helped to extend my contract. Their contributions have proved very helpful.

Special thanks to Michael Böge for endless discussions about spin polarization and delivering closed orbit bumps for polarization measurements.

I am much obliged to Frank Tecker, who helped me with PAW and LaTeX problems and explained the principle of the k-modulation to me with much patience.

I would also like to express my gratitude to the numereous people who aided in either practical work or fruitful discussions, especially Enrico Bravin, Massimo Placidi, Rüdiger Schmidt and Jörg Wenninger. I will never forget the beautiful time of energy calibrations measurements over night.

Thanks to the members of the LEP Energy Working Group for the oppurtunity to follow and learn from their discussions.

The LEP operators who allowed me to make the k-modulation measurements during physics data acquisition are gratefully acknowledged.

Special thanks to Natalie Pocock who never stopped teaching her mother tongue and helped with LaTeX knowledge.

Last but not least thanks go to my parents who have supported me throughout my studies.